Sorbonne Université

École doctorale 388

Laboratoire Chimie Physique – Matière et Rayonnement (LCPMR)

Laboratoire d'Optique Appliquée (LOA)

Studying ultrafast magnetization dynamics through Faraday effect and using linearly polarized high order harmonics

Par Carla Alves

Thèse de doctorat de Chimie Physique et Chimie Analytique

Dirigée par Jan Lüning

Présentée et soutenue publiquement le 14/12/2018

Devant un jury composé de :

Mme. Catherine Gourdon	Directrice de Recherche	Sorbonne Université	(Président du jury)
Mme. Annie Klisnick	Directrice de Recherche	Université Paris-Saclay	(Rapporteur)
M. Jan Vogel	Directeur de Recherche	Institut Néel	(Rapporteur)
M. Pascal Salières	Directeur de Recherche	CEA	(Examinateur)
M. Jan Lüning	Professeur	Sorbonne Université	(Directeur de thèse)
M. Guillaume Lambert	Ingénieur de Recherche	LOA	(Invité)

"O que dá o verdadeiro sentido ao encontro é a busca, e é preciso andar muito para se alcançar o que está perto."

José Saramago

Contents

List of Abbreviations

3TM	**3** **T**emperature **M**odel
BPM	**B**it-**P**atterned **M**edia
CCD	**C**harge-**C**oupled **D**evice
EUV	**E**xtreme **U**ltra-**V**iolet
FEL	**F**ree-**E**lectron **L**aser
GMR	**G**iant **M**agneto-**R**esistance
HAMR	**H**eat-**A**ssisted **M**agnetic **R**ecording
HHG	**H**igh **H**armonic **G**eneration
IR	**I**nfra-**R**ed
LCL	**L**eft- **C**ircular **L**ight
LCPMR	**L**aboratoire de **C**himie **P**hysique - **M**atière et **R**ayonnement
LLG	**L**andau **L**ifshitz **B**loch
LLG	**L**andau **L**ifshitz **G**ilbert
L-MOKE	**L**ongitudinal **M**agneto-**O**ptical **K**err **E**ffect
LOA	**L**aboratoire d'**O**ptique **A**ppliquée
MCD	**M**agnetic **C**ircular **D**ichroism
MO	**M**agneto-**O**ptical
MOKE	**M**agneto-**O**ptical **K**err **E**ffect
M3TM	**M**icroscopic **3** **T**emperature **M**odel
P-MOKE	**P**olar **M**agneto-**O**ptical **K**err **E**ffect
RCL	**R**ight- **C**ircular **L**ight
SAS	**S**mall-**a**ngle **S**cattering
SFA	**S**trong **F**ield **A**pproximation
T-MOKE	**T**ransverse **M**agneto-**O**ptical **K**err **E**ffect
TMR	**T**unneling **M**agneto-**R**esistance
XFEL	**X**-ray **F**ree-**E**lectron **L**aser
XMCD	**X**-ray **M**agnetic **C**ircular **D**ichroism

Introduction

The quest for faster and smaller storage technology is one of the main interest of today's society. The performance of these devices strongly depends on how fast the magnetic properties of materials can be manipulated. And the information storage capacity depends on how small the magnetic materials can be reduced. Therefore, an advancement of this subject matter is as much in the interest of the industry as of the scientific community, regarding the wealth of the related discoveries. In this context, Beaurepaire *et al.* [1] made a great discovery in 1996 that opened an entirely new field of research. An ultrafast loss of the magnetization (<1ps) of a nickel film was observed after excitation of the magnetic layer by an intense femtosecond IR laser pulse. This observation was very surprising at the time, leading to the beginning of the laser-induced magnetization dynamics research field. By applying an external magnetic field to a magnetic material, all the spins will be aligned leading to a macroscopic magnetization. A dynamic response is induced when the direction of the magnetic field is suddenly turned. The magnetization must follow this external field giving rise to a reorientation of the spins. The process occurs within a few hundred femtoseconds after the magnetic sample being perturbed by a femtosecond laser pulse. The electrons in the material quickly absorb part of the laser energy, creating a thermal disorder among their spins that results in a lower magnetization. The mechanism behind this ultrafast loss is actively debated and no clear microscopic explanation of the experimentally observed effects in magnetic materials was accepted so far.

To follow such fast dynamics of magnetic materials for later technological applications, two conditions are required for the laser source. First, short pulses are demanded to explore the dynamics on the femtosecond time scale. Second, the light source must cover the extreme ultraviolet or soft x-ray ranges to probe nanoscale magnetic materials. Both conditions are satisfied by the synchrotron femto-slicing and the FEL/XFEL

sources. The main drawback of these large-scale sources is the limited user accessibility due to the small number of operational facilities worldwide. More accessible light sources in the extreme ultraviolet and soft X-rays ranges are based on the generation of high-order harmonics. The harmonic generation process is a nonlinear optical response of individual atoms in a gas while interacting with a laser beam. It offers an elegant approach to achieve table-top sources of coherent light with an ultra short flash of light, typically a few femtoseconds. For a long time, none of the available tools were fast enough to solve atomic and molecular dynamics. Consequently, harmonic sources have become an important key in many areas of investigation, including magnetism, making possible the study of ultrafast magnetization dynamics with high temporal resolution and jitter free.

Magnetization phenomena is evaluated through magneto-optical effects, which describe the interaction of magnetism with light. Therefore, high-order harmonic sources are commonly used in two different approaches regarding the polarization of the light, whether it is required elliptically or linearly polarized. Elliptically polarized light allows studies based on the magnetic circular dichroism [2], [3], which describes the different response of a magnetized material to left and right-handed elliptically polarized light. Likewise, studies of magneto-optical effects using linearly polarized harmonics are performed, including the transverse magneto-optical Kerr effect [4]–[6] and magnetic diffusion [7] techniques. While the transverse magneto-optical Kerr effect is executed in a reflection geometry retrieving information only about the material's surface phenomena, the magnetic diffusion drawback, in a transmission geometry, lies on the difficulty of producing magnetic domains in the majority of the materials. The observation of the magnetic circular dichroism in time-resolved experiments requires a very high degree of elliptically polarized harmonics with efficient fluence, which requires deeper investigations of the available techniques. Hence, for the first time we propose here to study the ultrafast magnetization dynamics through the Faraday effect, which goes beyond all those difficulties by using simply generated linearly polarized harmonics. The transmission geometry allows to probe all the layers of the material and no magnetic domains are required. Our approach is based on the resonant Faraday effect on the M absorption edge of transition metals, particularly between 40 and 70 eV for cobalt-based materials.

Thesis organization

This thesis reports the investigation of ultrafast magnetization dynamics in cobalt through the magneto-optical Faraday effect. Linearly polarized high-order harmonics are generated in noble gases in the extreme ultraviolet range to cover the entire M absorption edge of cobalt. To accomplish this work, the following objectives were defined:

- Assembly of the linearly polarized harmonic source for both static and pump-probe experiments,
- Measurement of the static magneto-optical Faraday effect in cobalt based materials,
- Measurement of the evolution of the magnetization dynamics of cobalt based materials through the Faraday effect,
- Accomplishment of the experiments using different thicknesses of cobalt based materials.

Chapter 1 includes the general scientific background behind this recent research field, the laser-induced ultrafast magnetization. The most relevant related theory and concepts for our experimental investigation are also reported.

The high-order harmonic source used to probe the magnetization dynamics of cobalt based materials is detailed in **Chapter 2**. In particular, the most important highlights of the theory behind the phenomenon as well as the experimental approach used in our work are presented. This chapter also focus on the importance of the high-order harmonic source for ultrafast magnetization dynamics studies. Additionally, the description of the harmonics polarization state is presented along with some techniques used to obtain elliptically polarized light. This is related with my first experimental results performed at the beginning of my PhD, which are detailed in Appendix A.

The **Chapter 3** refers to the experimental work that culminates the discussed points in the two previous chapters in an experimental realization. The experimental setup is explained in detail along with the principle of the measurement and the samples details. The static and time resolved measurements are reported around the magnetically dichroic M absorption edge in CoDy and Co/Pt samples.

CHAPTER 1

Fundamentals of ultrafast magnetism

Today's technology is intrinsically dependent on the phenomenon of magnetism. Ultrafast magnetization dynamics is a recent research topic which covers several processes occurring on a wide range of timescales. This chapter presents the general scientific background behind the laser-induced magnetization dynamics research field, as well as the relevant theory and concepts for the experimental investigation reported in this work.

1.1 Brief summary of the history of magnetism

Magnetism is an interesting phenomenon which plays an important role in the development of the civilization from the very beginning up to nowadays. Although its history dates back to earlier than 600 B.C., it was only in the twentieth century that scientists have begun to understand it and develop technologies based on this understanding. In the northen Greece, in a city called Magnesia, a shepherd found a material with the ability to attract other pieces of the same material and iron. This material was a mineral magnetite called lodestone, which consists of iron oxide. The ancient Greeks called it a magnet because of the name of the city. Scientifically, William Gilbert (1540-1603) was the first to investigate the phenomenon of magnetism, discovering that Earth is itself a weak magnet. Early theoretical investigations into the nature of Earth's magnetism were carried out by the german Carl Friedrich Gauss (1777-1855). Charles Coulomb (1736-1806) established the inverse square law of force, which states that the attractive force between two magnetized objects is directly proportional to the product of their individual fields and inversely proportional to the square of the distance

between them. Hans Christian Oersted (1777-1851) first suggested a link between electricity and magnetism. Experiments showing the interaction between the effects of magnetic and electric fields were then conducted by Ampere (1775-1836) and Faraday (1791-1869). Also in the nineteenth century, Maxwell (1831-1879) provided the theoretical foundation to the physics of electromagnetism. A full understanding of the magnetic effects on an atomic scale came in the late 1920's with the advent of quantum mechanics by one of the founding fathers, Heisenberg (1901-1976) [8]. From here new materials with wide applications in modern technology were created.

We can store information collected in a lifetime into a hard drive thanks to magnetism. The discovery of the giant magneto-resistance (GMR) by Albert Fert and Peter Grünberg in 1988, is an important milestone in the history of magnetism. GMR refers to the large changes in electrical resistance observed in thin magnetic films and multilayers depending on whether the magnetization of adjacent ferromagnetic layers are in a parallel or an antiparallel alignment. The resistance can thus be manipulated by an externally applied magnetic field. This effect is widely used in hard-drive storage technologies which have created a $50 billion industry. It is a great discovery which also marked the birth of *spintronics*, a new type of electronics where both the charge and the spin of electrons play a fundamental role. For example, the so-called spin polarized current, a current where the carriers have their spins oriented in the same direction, is created based on the GMR effect and used for many spintronics applications. A similar effect to the GMR is the tunneling magnetoresistance (TMR), whose effect relies on the possibility for electrons to tunnel between two magnetic layers [9]–[11]. The effect is being used in read heads to read/write in the computer hard discs. Areal density is defined as the number of bits in one inch square of hard-drive media. Conventional magnetic storage devices are limited to densities of 400 Gbits/in^2 (i.e. one bit/40 $\times$ 40 nm^2) and reading/writing times of 2 ns. Nowadays, the investigation focus on the quest for the smaller and the faster to understand the limits in the speed of the magnetization dynamics and in the information storage capacity.

The heat-assisted magnetic recording (HAMR) [12] as well as the bit-patterned media (BPM) [13] are promising for faster and higher capacity hard-drives in the future (figure 1.1). The HAMR uses a small amount of laser heating to increase the temperature of recording spot (bit) to be able to switch the magnetization of the harder magnetic materials used to increase the bits density. Here, it is important to clearly understand

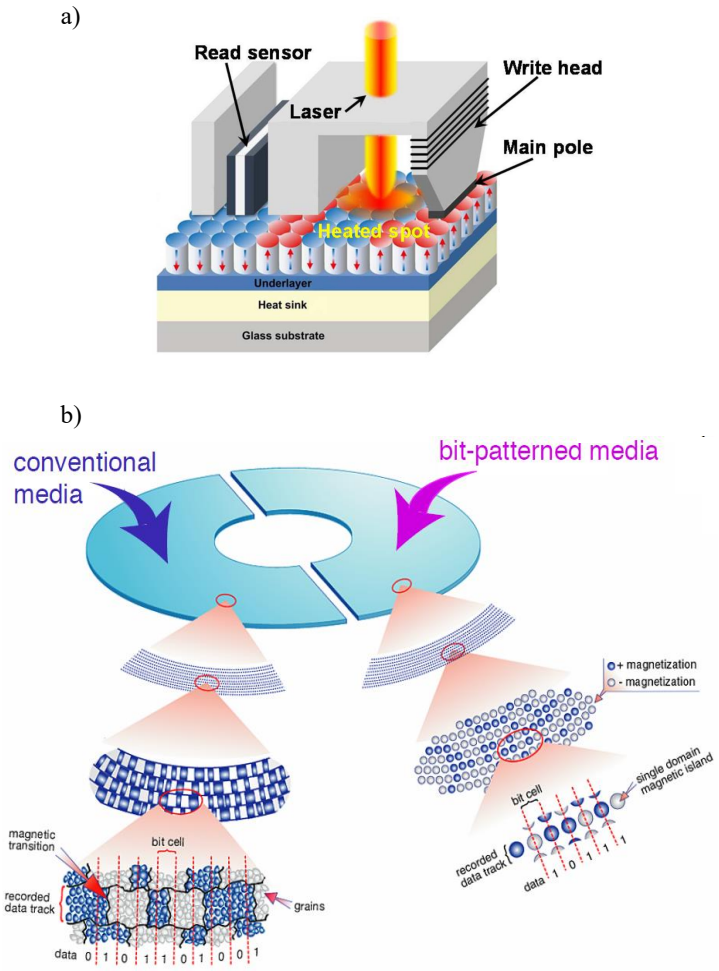

FIGURE 1.1: **Future hard-drive technologies.** A schematic representation of the working principle of a) HAMR (from [14]), and b) conventional granular media (blue arrow) and BPM (pink arrow) (from [15]).

the magneto-optical effects (MO) to be able to control the interaction between a laser pulse and a magnetic material. The BPM lies on the idea of using very small and well-organized grains, or bits, to make reading and writing processes much more efficient. Combining BPM and HAMR may lead to an areal density of 300 Tbits/in^2, two orders of magnitude larger than the current commercial hard drives [16]. Therefore, light sources in the extreme ultraviolet or soft x-ray range to probe magnetic nanostructures, and with short pulses to explore the dynamics on the femtosecond time scale, are important for the development of future technologies.

This last magnetism research trend is not only on the interest of the industry and technology development: scientists are interested in the fundamental physics of magnetic materials and the related dynamics at ultrafast time scales. In this context, the first observation of laser-induced ultrafast demagnetization in 1996 [1] led to the development of a new field of research: ultrafast magnetization dynamics. After two decades of

increasing attention and research, the explanation behind the fundamental microscopic processes of the laser-induced magnetization dynamics is not well understood. In the rest of the chapter, this field is discussed, from the proposed theoretical hypothesis to the future applications, providing a bridge to the experimental results reported in this thesis.

1.2 Magneto-optical effects

Magneto-optical effects refer to interaction between light and a magnetized medium. These effects provide experimental support to the electromagnetic theory of light, as well as to both classical and quantum theory of matter. Using the MO effects, the magnetic properties of the materials can be studied, and the magnetization manipulated and probed with light. Michael Faraday performed the first successful MO experiments in 1845 [17]. He discovered that the polarization of a linearly polarized beam is rotated upon transmission through a material which is placed in a magnetic field parallel to the propagation direction of the light (figure 1.2 a)). In 1877, John Kerr observed the same effect in reflection [18], called the magneto-optical Kerr effect (MOKE) (figure 1.2 b)). Both effects arise from similar microscopic origins and can be explained

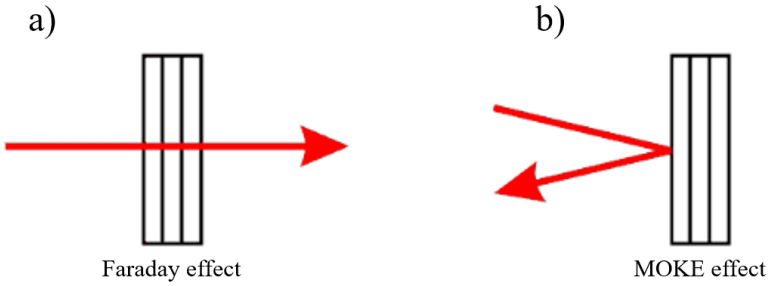

FIGURE 1.2: **Schematic representation of two MO effects configurations.** a) Faraday, and b) MOKE effects.

using the same formalism. By definition, linearly polarized light can be decomposed in the sum of two circularly polarized waves, left- and right-circular polarized (LCL and RCL, respectively), with equal amplitude. The magnetization of the medium leads to the propagation of these two waves with (1) different velocities, and (2) experiencing different absorption rates. From (1) the polarization axis of the incident light will rotate

and from (2) the beam will change its polarization from linear to elliptical. Other important MO effects are the magnetic circular dichroism (MCD) and the magnetic small-angle scattering (SAS). The MCD describes the differential absorption of left and right circularly polarized light, induced in a magnetized sample. In the SAS technique, the incident linearly polarized light is focused in a material with a magnetic domain structure giving rise to magnetic scattering. In all the referred MO effects, a dependence of the complex refractive index with the magnetization is present. Nevertheless, in the next paragraphs, this dependence is only shown for the case of the Faraday effect.

1.2.1 Magneto-optical Faraday effect

The Faraday effect is schematically represented in figure 1.3 for an out-of-plane magnetized sample. As already mentioned, linearly polarized light can be decomposed into the sum of left- and right-circular polarized light. Consequently, each of the components will experience a different refractive index as it propagates through a magnetic material. The complex refractive indices $n\pm$ for these two circularly polarized waves describe the propagation of the radiation through the sample, where $\pm$ refer to left- and

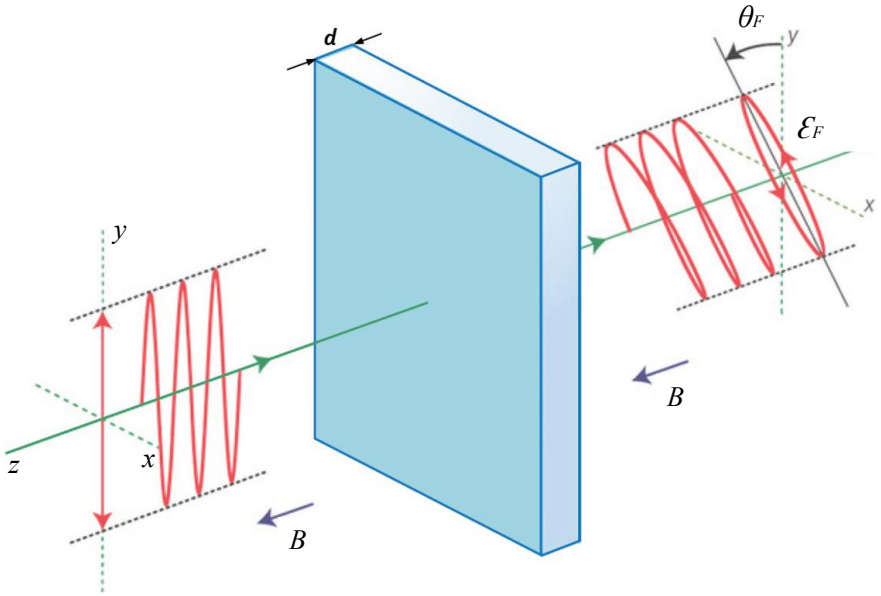

FIGURE 1.3: **Faraday effect illustration (adapted from [19]).** The polarization axis of the incident linearly polarized light (red line) changes upon transmission through a magnetized sample. θ_F and ε_F corresponds to the Faraday rotation and ellipticity, respectively.

right-circular of the photon helicity relatively to the wave vector ($\vec{k}$) of the light,

$$n_{\pm} = 1 - (\delta_0 \pm \Delta\delta) + i(\beta_0 \pm \Delta\beta). \tag{1.1}$$

And in this particular case, where the sample's surface is perpendicular to the propagation of the light (see figure 1.3), the magnetization of the sample ($\vec{M}$) is parallel to $\vec{k}$. In equation 1.1, $\Delta\delta$ and $\Delta\beta$ are the intrinsic material's magnetic-optical quantities, describing the Faraday rotation and ellipticity, respectively (θ_F and ε_F in figure 1.3). $\Delta\delta$ corresponds to the dephasing of the radiation, while $\Delta\beta$ describes the absorption. For magnetized ferromagnetic materials, both are nonzero. In fact, if one of the circular waves travels faster than the other through the material, constituting a dephasing, it will also rotate faster generating the rotation of the light's polarization axis [20]. And the difference in absorption of the two circularly polarized waves changes the polarization of the light from linear to elliptical.

Mathematically, the light transmitted through the sample propagating along the z axis is described as follows for the left- and right-circularly polarized waves [21],

$$\vec{E}_{\pm}(\vec{r}, t) = \frac{1}{\sqrt{2}} E_0(\vec{e}_x \pm i\vec{e}_y) e^{i\omega n_{\pm} z/c - i\omega t}, \tag{1.2}$$

where ω the frequency of the light. Both the phases and the amplitudes of the two circularly polarized waves have become unequal after passing through the sample. The ratio of the two electric field vectors for a sample with thickness d at normal incidence is then given by

$$\frac{E_+(\vec{r}, t)}{E_-(\vec{r}, t)} = e^{i\omega d(n_+ - n_-)/c}. \tag{1.3}$$

From the Fresnel equation for the magnetic refractive indices of the material [21], θ_F and ε_F can be related to $n_{\pm}$ by the equation

$$\left(\frac{1 - \tan\varepsilon_F}{1 + \tan\varepsilon_F}\right) e^{2i\theta_F} = e^{i\omega d(n_+ - n_-)/c}. \tag{1.4}$$

Since θ_F and ε_F are small compared to the nonmagnetic response, equation 1.4 can be expanded to first order in the small quantities, which gives

$$\theta_F + i\tan\varepsilon_F \approx \frac{\omega d}{2c}(n_+ - n_-). \tag{1.5}$$

The two Faraday polarization effects can thus be decomposed into two parts,

$$\theta_F = \frac{\omega d}{2c}\Re(n_+ - n_-), \tag{1.6}$$

$$\tan\varepsilon_F = \frac{\omega d}{2c}\Im(n_+ - n_-). \tag{1.7}$$

$\Delta\delta$ and $\Delta\beta$ can be obtained using the equation 1.1 in the above ones,

$$\theta_F = -\frac{\omega d}{c}\Delta\delta, \tag{1.8}$$

$$\tan\varepsilon_F = \frac{\omega d}{c}\Delta\beta. \tag{1.9}$$

If the incoming light is not normal, but oblique ($d = d_0/\cos\theta_t$) at an incident angle θ_i [20], [22],

$$\theta_F = -\frac{E_{phot} d_0}{\hbar c \tan\theta_t}\Delta\delta, \tag{1.10}$$

$$\tan\varepsilon_F = \frac{E_{phot} d_0}{\hbar c \tan\theta_t}\Delta\beta. \tag{1.11}$$

where E_{phot} is the photon energy, d_0 is the thickness of the foil and θ_t is the angle of refraction. For x-ray light at the $2p$ edges, $\tan\theta_t \approx \tan\theta_i$. Thus, $\Delta\delta$ and $\Delta\beta$ can be directly obtained from the experiment with small error. Although the first order approximation is valid in the soft-X-ray range, a more exact expression which relates both θ_F and ε_F to the optical constants is required [20].

1.2.2 Magneto-optical Kerr effect

One can distinguish three main MOKE configurations which are represented in figure 1.4. The plane xy is the plane of incidence. When magnetization $\vec{M}$ is in the plane

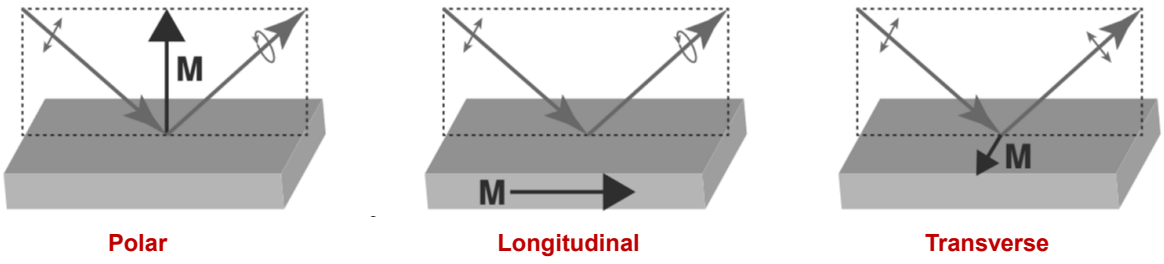

FIGURE 1.4: **Different geometries for MOKE experiments (adapted from [23]).** A schematic of the polarization state of the light is also represented before and after the light reflection on the sample.

of incidence and perpendicular to the sample surface, it corresponds to the polar geometry (P-MOKE). In longitudinal geometry (L-MOKE), $\vec{M}$ is parallel to both the sample surface and plane of incidence. Lastly, in the transversal configuration (T-MOKE) configuration, the $\vec{M}$ remains parallel to the sample surface but perpendicular to the plane of incidence.

In the P-MOKE and the L-MOKE a polarization analysis is required to have information on the magnetization. On the contrary, in the T-MOKE there is no change in the polarization state since the magnetization is perpendicular to the plane of incidence. Here, the reflectivity of *p*-polarized light will give information on the amplitude and the direction of the magnetization [18].

1.2.3 Magnetic circular dichroism

Dichroism is defined as the property of some materials of absorbing light to different extents depending on the polarization form of the incident beam. Circular dichroism refers to the different absorption rates of the material for right- and left-handed circularly polarized light. When the effect is induced in a sample by a magnetic field parallel to the direction of light propagation, we refer to the magnetic circular dichroism (figure 1.5 a)). If the incident light is in the x-ray range, we refer to the XMCD. The effect is

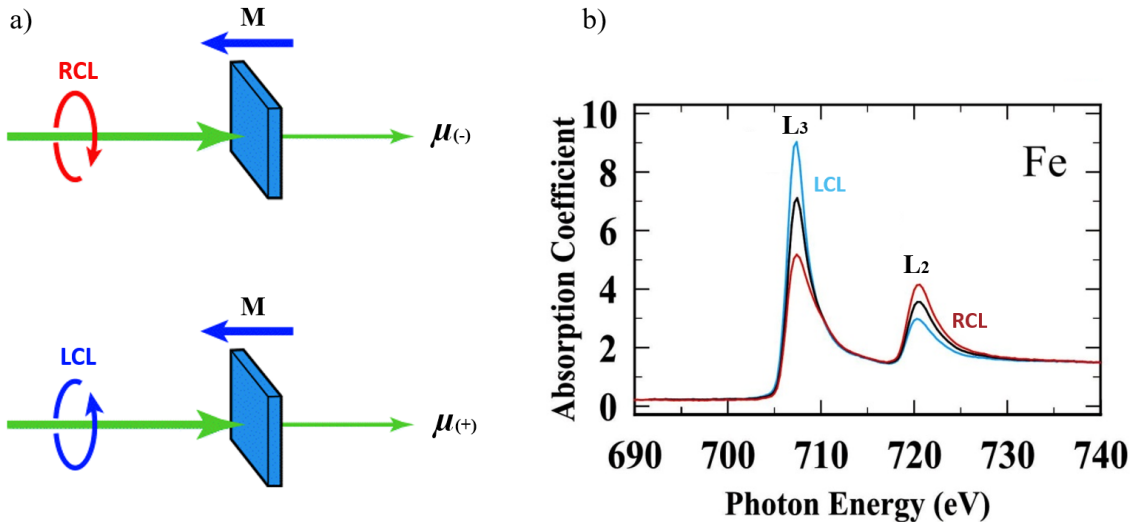

FIGURE 1.5: **Principle of magnetic circular dichroism measurement.** a) Schematic representation of the MCD, where the incident light (RCL or LCL polarized) is parallel to the sample's magnetization (adapted from [24]). The transmitted light has different absorption coefficients depending on the helicity of the circularly polarized light, $\mu_{(-)}$ and $\mu_{(+)}$ for RCL and LCL, respectively. b) Absorption spectra measured at the L-edge of Fe for LCL and RCL helicities (from [25]).

related with the magnetism induced change in the absorption spectra, close to an absorption edge of the material. The absorption spectra measured at the material's edge depends on the helicity of the circularly polarized light, as represented in figure 1.5 b) for LCL and RCL polarizations. The dichroism signal is then given by the difference between the two spectra corresponding to right- and left-handed circularly polarized light, which is described by the asymmetry of the absorption as follows,

$$A_{XMCD} = \frac{I^{LCL} - I^{RCL}}{I^{LCL} + I^{RCL}} \tag{1.12}$$

The observation of the XMCD signal strongly depends on the orientation of the sample's magnetization, which is maximized when it is parallel or antiparallel to the polarization axis of the incident light. XMCD has become a unique and widely used tool in magnetic spectroscopy allowing element specificity, which enables the characterization of different components in complex systems. In addition, quantitative information about the orbital angular momentum and spin components of the magnetization can also be provided by the XMCD measurement. By increasing the thickness of the magnetic material, the contrast level is improved. However, the drawback lies on the light transmission through the sample, which is exponentially reduced by the material thickness.

1.2.4 Resonant magnetic small-angle scattering

In SAS techniques, the radiation is elastically scattered by a sample and the resulting pattern gives information on the size, shape, local magnetic moments, magnetic structure and phase transitions of the sample.

In some materials, it is possible to obtain a structure of magnetic domains having opposite magnetization directions at nanometer size by applying a specific demagnetization procedure [7]. This structure acts as a grating that scatter light into a plus and minus first diffraction orders, as represented in figure 1.6 a). The scattered intensity in the first-order peaks is known to be proportional to the square of the magnetization magnitude within each magnetic domain, M^2. We can then measure the dynamics of the magnetization by following the intensity of the scattering peaks (figure 1.6 b)). The scattering pattern can be observed with linearly polarized light since the light can

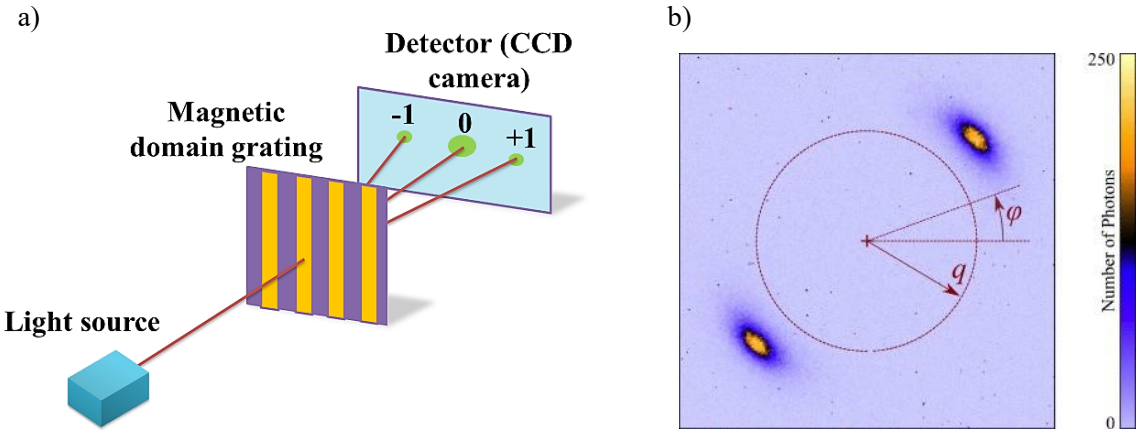

FIGURE 1.6: **Magnetic small-angle scattering technique.** a) Schematic representation of the technique where the structure of the sample acts as a grating that diffracts the light into two symmetric diffraction orders and, b) resonant magnetic scattering pattern of a domain structure at the cobalt $M_{2,3}$ absorption edge (from [26]).

be decomposed in the sum of right and left circularly polarized field of equal intensity. Many studies have been performed with the SAS technique using free-electron laser (FEL) [27] and high order harmonic generation (HHG) [7], [26] sources. The main drawback of this technique lies on the limited type of materials in which magnetic domains are possible to obtain.

1.3 Ultrafast magnetization dynamics

Magnetization dynamics describes the evolution of the magnetization of a material, whose related processes occurs in a large range of timescales (figure 1.7). In the millisecond to second range, the thermal activated magnetization processes, such as viscous regime, domain nucleation and domain growth take place. From picosecond to nanosecond timescale, precessional and magnetic vortex dynamics as well as magnon generation and propagation and domain wall motion are observed. An easy way of

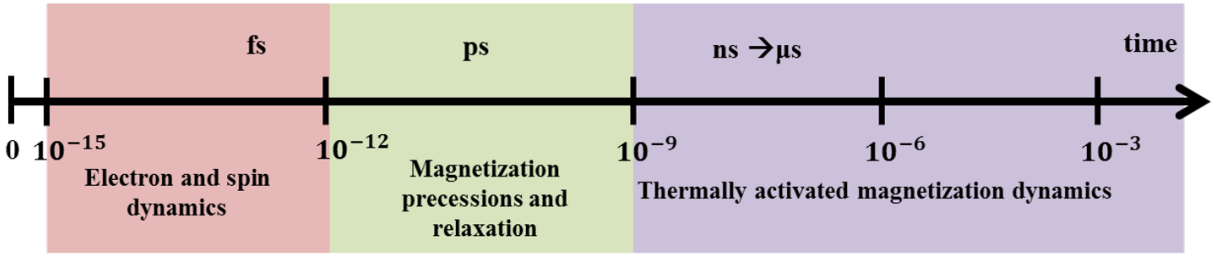

FIGURE 1.7: **Characteristic time scales in magnetism (from [28]).**

inducing a dynamic response in a magnetic material is by applying an external magnetic field. If the field is strong enough, all the spins tend to align in a ferromagnetic medium giving rise to a macroscopic magnetization. If the magnetic field direction is suddenly turned, the magnetization has to follow this external field. A reorientation of the spins occurs by a coherent damped precession of the spins around the external field as described by the Landau-Lifshitz-Gilbert equation [29], [30]. The frequency of the precession is normally in the GHz range, corresponding to a period of a few hundreds of ps, and the reorientation process can take several nanoseconds. At the femtosecond regime, ultrafast demagnetization processes occur, related with the exchange interaction between spins. In specific, the ultrafast demagnetization process takes place within a few hundred fs after the magnetic sample being perturbed by a fs laser pulse. The electrons in the material quickly absorb part of the laser energy, creating a thermal disorder among their spins that results in a lower magnetization. This process is several orders of magnitude faster than the timescales involved in precessional dynamics. Typical demagnetization curves are shown in figure 1.8. It shows the timescale on which the demagnetization is quenched.

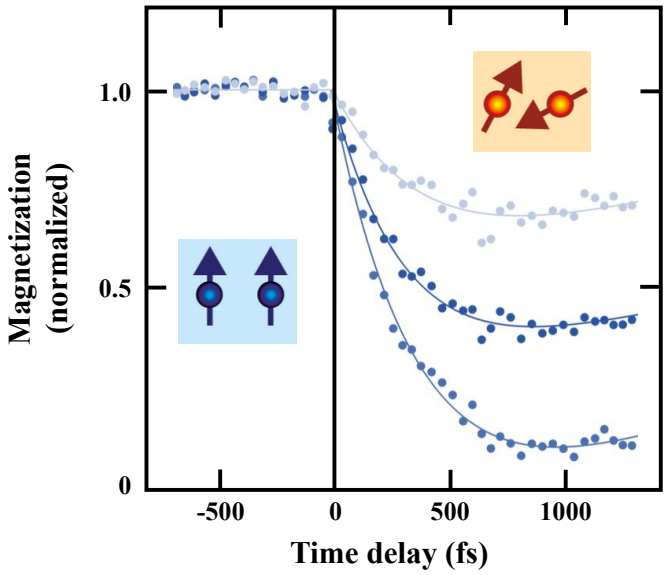

FIGURE 1.8: **Typical ultrafast demagnetization curves with different demagnetization degrees.** After a femtosecond laser perturbation, a thermal disorder among the spins of the electrons in the material occurs, resulting in a lower magnetization.

The laser-induced ultrafast demagnetization research topic has high potential in technological applications, particularly magnetic storage technology. The process can

be useful for writing information in magnetic media in a very fast way. Therefore, two conditions are required for the light source:

1. short pulses to explore the dynamics on the femtosecond time scale,

2. extreme ultraviolet or soft x-ray range to probe magnetic nanostructures.

But these studies are still in the fundamental research stage, with no clear microscopic explanation for the experimentally observed effects in magnetic materials. In the next subsections, a brief overview of this phenomenon is presented.

1.3.1 Laser-induced demagnetization dynamics: historical review

First experiments in laser excitation of ferromagnetic materials were conducted by Vaterlaus *et al.* [31], [32]. The authors estimated that spin-lattice relaxation in Gd takes place within $\sim 100 \pm 80$ ps. In other words, spin-orbit interactions cause electrons to lose their spin-angular momentum in the lattice, and as a result, the spin polarization of the electrons disappears. These experimental results along with theoretical predictions led to the conclusion that demagnetization upon laser heating follows from spin-lattice relaxation at a typical timescales between 0.1 and 1 ns.

In 1996, Beaurepaire *et al.* [1] observed the demagnetization dynamics of a Ni film via MOKE pumped, for the first time, with a very short pulse (60 fs). Surprisingly, the magnetization of Ni achieved its minimum value, almost 50% less than the saturation value, in less than 1 ps instead of the expected demagnetization time of some tens of ps (figure 1.9). This observation was soon confirmed by other groups [33], [34] and the community has come to a full consensus about a typical demagnetization time within 100-300 fs. After the first observation of ultrafast demagnetization, a number of new investigations emerged. Laser-induced launching of magnetization precession and spin waves in canted ferromagnetic thin films was demonstrated [35]. The loss of magnetization was directly detected by emission of terahertz radiation [36]. Later, laser-induced magnetization dynamics in coupled multilayers was studied [37]–[39].

Several hypothesis have been debated to explain the phenomenon of laser-induced ultrafast demagnetization from a microscopic point of view [40]–[48]. The main issue relies on understanding how angular momentum can be redistributed among electrons, spins and the lattice on such a short time scale. Indeed, magnetization is angular momentum and angular momentum has to be conserved within the system. In

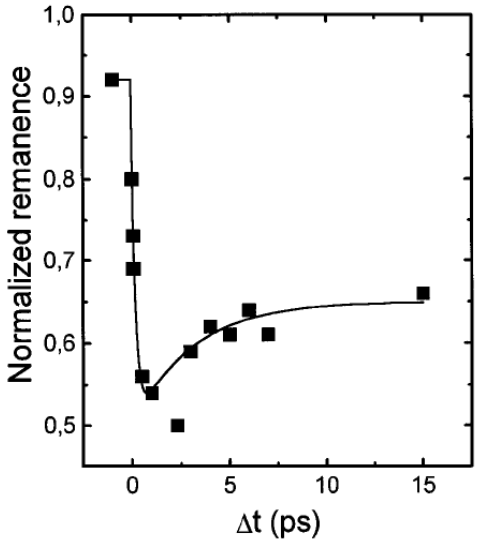

FIGURE 1.9: **Beaurepaire *et al.* experimental observation of ultrafast demagnetization in a Ni thin film (from [1]).** The normalized remanence, proportional to the magnetization, drops in roughly 50% within the first ps, after fs optical excitation.

the following subsections, some models explaining ultrafast demagnetization are discussed, starting with two phenomenological models, one based on the Landau-Lifshitz equation and the popular three temperature model. These two models describe the experimental observations without taking explicitly into account the transfer of angular momentum. Afterwards, microscopic models explicitly considering the transfer of angular momentum for the underlying origin of ultrafast demagnetization are described.

1.3.2 Models based on the Landau-Lifshitz equation

The precessional motion of a magnetic moment is described by the Landau-Lifshitz equation [29],

$$\frac{d\vec{m}}{dt} = \gamma \vec{m} \times \vec{H}_e, \tag{1.13}$$

where γ is the gyromagnetic ratio and $\vec{H}_e$ is an effective magnetic field containing many material dependent contributions, namely the external applied field, the anisotropy field and the demagnetization field.

In 1955, this equation was improved for the case of damping of a magnetic moment without magnitude change, the Landau-Lifshitz-Gilbert (LLG) equation [49],

$$\frac{d\vec{m}}{dt} = \gamma \vec{m} \times \vec{H}_e + \frac{\alpha}{|\vec{m}|} \vec{m} \times \frac{d\vec{m}}{dt}, \tag{1.14}$$

with α being a dimensionless phenomenological Gilbert damping constant. But this is valid only at low temperature and for no change of the magnetic moment magnitude. Therefore, one can use the Landau-Lifshitz-Bloch (LLB) equation [50], which is valid up to and beyond the Curie temperature T_C [51], to describe changes in the magnetization vector norm.

$$\frac{d\vec{m}}{dt} = \gamma\vec{m} \times \vec{H}_e - \gamma\lambda_{\parallel}\frac{\vec{m}(\vec{m}\cdot\vec{H}_e)}{m^2} + \gamma\lambda_{\perp}\frac{\vec{m}\times(\vec{m}\times\vec{H}_e)}{m^2}, \tag{1.15}$$

where $\lambda_{\parallel}$ and $\lambda_{\perp}$ are the dimensionless longitudinal and transversal damping parameters [52]. The three contributing terms of the LLB equation is schematically represented in figure 1.10.

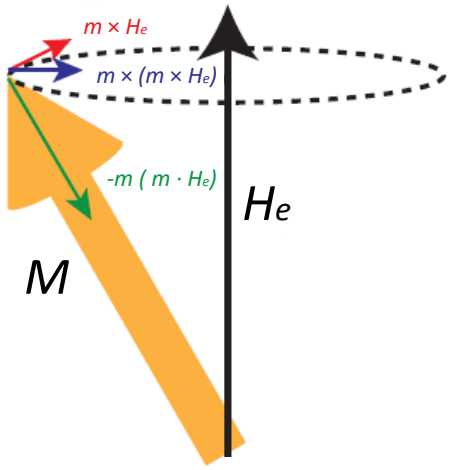

FIGURE 1.10: **Illustration of the Landau-Lifshitz-Bloch equation (adapted from [53]).** The three terms of the equation 1.15 are represented. The red force corresponds to the first term, which makes the magnetic moment precessing around H_e. The second term matches the green force, which is the source of demagnetization by longitudinal damping. Finally, the blue force corresponds to the third term, which applies a transversal damping to align the magnetic moment along H_e without changing its magnitude.

The LLG and LLB equations successfully describes some ultrafast demagnetization dynamics experiments [1], [42], [54] but no assumptions are made about the microscopic mechanisms behind the damping parameters.

1.3.3 Three temperature model

Beaurepaire *et al.* [1] introduced a phenomenological three temperature model (3TM), based on the two-temperature model that assumes that electrons and the lattice are different coupled heat reservoirs by defining the temperature of the electrons and phonons. In the three temperature model, the spin-degree of freedom was added as a third reservoir, describing then the interaction between the electrons (e), spins (s) and lattice (l), as sketched in figure 1.11 a). The temporal evolution of the system's temperature is described by the following coupled differential equations [1]:

$$C_e(T_e)\frac{dT_e}{dt} = -G_{el}(T_e - T_l) - G_{es}(T_e - T_s) + P(t), \tag{1.16}$$

$$C_s(T_s)\frac{dT_s}{dt} = -G_{es}(T_s - T_e) - G_{sl}(T_s - T_l), \tag{1.17}$$

$$C_l(T_l)\frac{dT_l}{dt} = -G_{el}(T_l - T_e) - G_{sl}(T_l - T_s), \tag{1.18}$$

where $P(t)$ represent the initial excitation from the laser, C the heat capacities and T the temperature of the three systems. G_{el}, G_{es} and G_{sl} are the coupling constants between electrons and lattice, electrons and spins, and spins and lattice, respectively. Once determined, G gives information about the strength of a particular link but does not determine the nature of the interaction. The laser excitation with a femtosecond laser pulse

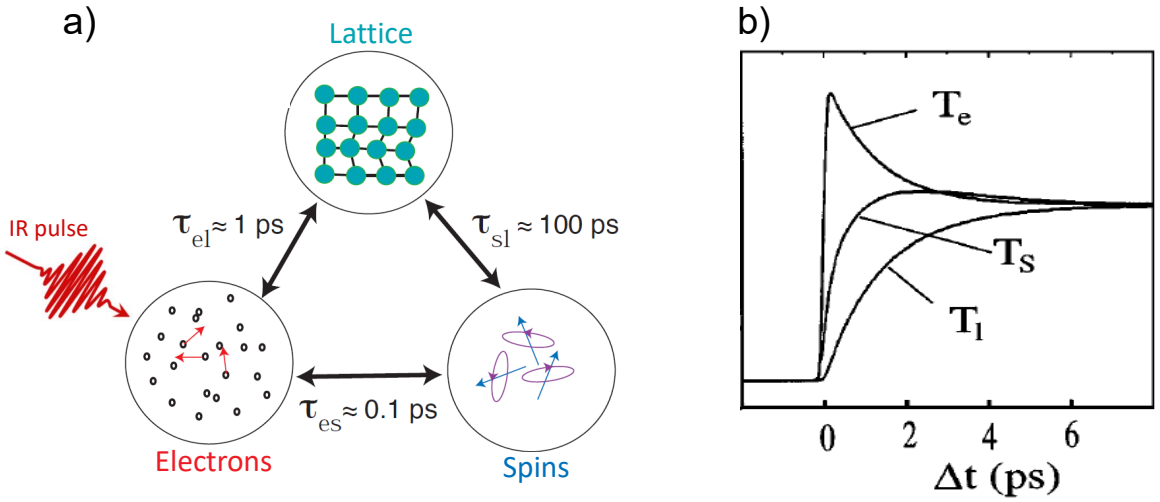

FIGURE 1.11: **Three temperature model.** a) Schematic diagram with the respective interaction time constants between the reservoirs (adapted from [55]). b) Experimental observation of spin (T_s), lattice (T_l), and electron (T_e) temperatures [1].

is initially almost instantaneously absorbed by the electrons. The heat is then redistributed among the three systems through the previous equations, following by spin and then lattice. The temperature evolution between different reservoirs after the laser excitation is schematically shown in figure 1.11 b).

Nevertheless, the three temperature model is not sufficient to completely understand the microscopic mechanisms involved in laser-induced demagnetization. Once more, the angular momentum conservation should be considered in the magnetic system, which explains what happen with the spins during full demagnetization process [56]. This problem is discussed in the following subsection.

1.3.4 Microscopic models for ultrafast demagnetization

Despite more than two decades of research, the microscopic quantum interpretation for the ultrafast demagnetization is still under debate by the scientific community. Figure 1.12 shows a schematic timeline of the possible ultrafast photon-electron-spin-lattice interactions after an excitation by an ultrafast laser [57]. To clarify the phe-

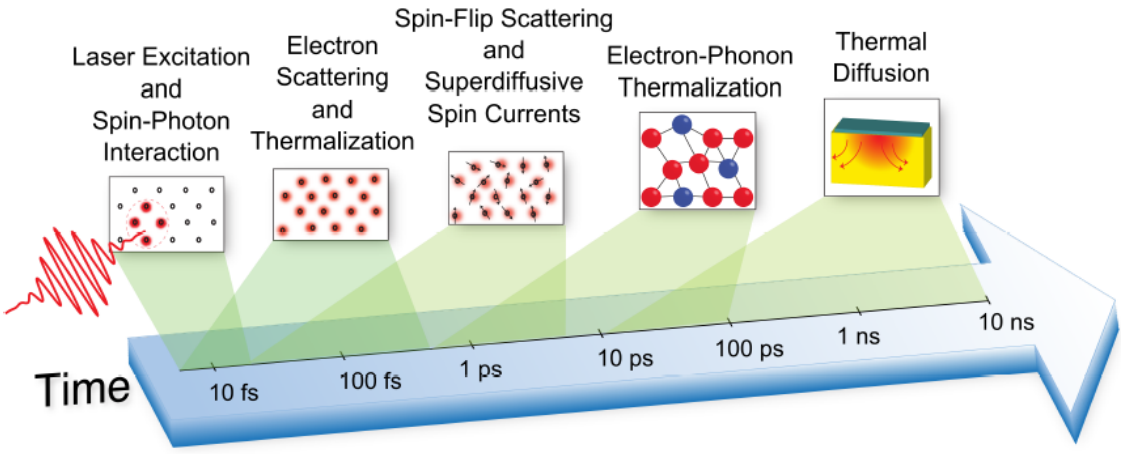

FIGURE 1.12: **Schematic timeline of ultrafast photon-electron-spin-lattice interactions after an ultrafast laser excitation (adapted from [57]).** A laser excitation on the electron system trigger various scattering processes between electrons and phonons. First, the excited electron system thermalizes by electron-electron scattering and the material starts to demagnetize because of spin-flip scattering and superdiffusive spin currents events during this thermalization process. Then, electron-phonon scattering processes transfer energy from the excited electrons to the lattice, and thermal equilibrium is typically reached on picosecond timescales. Lastly, the system riches the equilibrium by thermal diffusion on nanosecond timescales.

nomenon of ultrafast demagnetization, the importance of the contribution of each represented interaction during the process has to be established, specially the understanding of the angular momentum dissipation in a femtosecond timescale.

In this subsection, I present the two most discussed microscopic models. The first one based on the Elliott-Yafet Spin-flip events and the second based on the mechanism of spin super-diffusive transport.

1.3.4.1 Elliott-Yafet Spin-flip events

To explain the ultrafast demagnetization dynamics, Koopmans *et al.* [54] proposed to consider electron-phonon scattering event of Elliott-Yafet type [58]. Upon collision with a phonon, an electron has a probability a_{sf} to flip its spin. This model presupposes

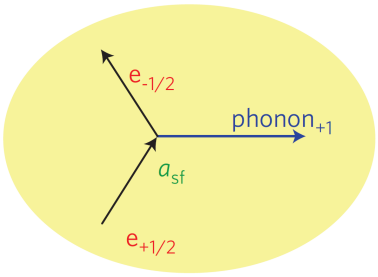

FIGURE 1.13: **Schematic representation of the Elliott-Yafet spin-flip scattering.** The electron changes its spin upon emission of a phonon, taking over angular momentum (from [42]).

that the angular momentum is directly transferred from the spin to the lattice. Later, in another investigation, Koopmans *et al.* proposed another model which combines the three temperature model with the Elliott-Yafet mechanism, the so-called the microscopic three temperature model (M3TM) [42]. In this model, ab initio calculations of the Elliot Yafet spin flip probabilities were considered. The behavior of Cobalt and Nickel demagnetization were successfully reproduced with this model. In the meantime, Essert *et al.* [59] concluded that electron-phonon spin-flip scattering is not sufficient to explain the experimental results behind ultrafast demagnetization. Furthermore, the dynamical changes of the band structure are important but they are not included in the M3TM. These last results infer that the Elliott-Yafet spin flip scattering phenomena cannot explain alone the demagnetization rate experimentally observed.

1.3.4.2 Spin super-diffusive transport

In 2010, Battiato *et al.* [45] proposed another mechanism to explain the ultrafast demagnetization behavior based on a spin dependent transport of hot electrons, called the spin super-diffusive transport. In this work, theoretical demagnetization curves of a Ni/Al bilayer and a Ni reference sample were compared to understand the different processes unleashed by laser excitation. The idea of the model is to verify if the electrons of the Al layer are excited by the effect of super-diffusive spin transport, as schematically represented in figure 1.14. It is shown that the spin majority electrons ("spin up") leave the excited region more promptly than the spin minority electrons ("spin down"), leading thus to femtosecond spin currents. The demagnetization of the excited region is an immediate consequence of the reduction of the number of spin majority electrons.

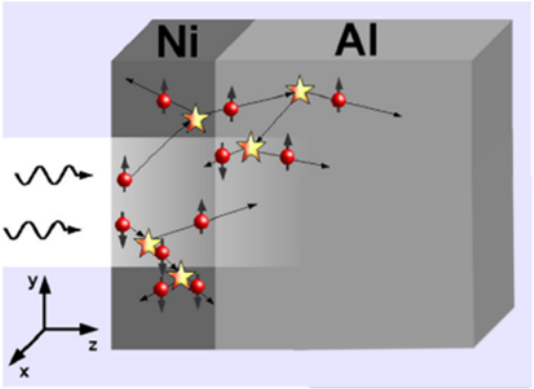

FIGURE 1.14: **Sketch of the super-diffusive phenomena created by a laser excitation.** Majority and minority spin carriers show different mean free paths and also a cascade of electrons is generated after an inelastic scattering (from [45]).

Other interesting investigations on utrafast spin dynamics were carried out by Rudolf *et al.* [60] using a Ni/Ru/Fe trilayer. The magnetization of the Ni and Fe layers can be either parallel or antiparallel (figure 1.15 a)). If the magnetization of Ni and Fe are parallel, the Ni layer magnetization decreases while the Fe is enhanced by the demagnetization of Ni, as plotted in figure 1.15 b). When they are antiparallel, the magnetization of both Ni and Fe layers decreases, as shown in figure 1.15 c). The results for these two systems on the femtosecond timescale infer the generation of super-diffusive spin current between Fe and Ni layers after optically induced demagnetization, which is in good agreement with the spin super-diffusive transport model. On the other hand, Schellekens *et al.* [61] revealed that spin transport is negligible in the demagnetization

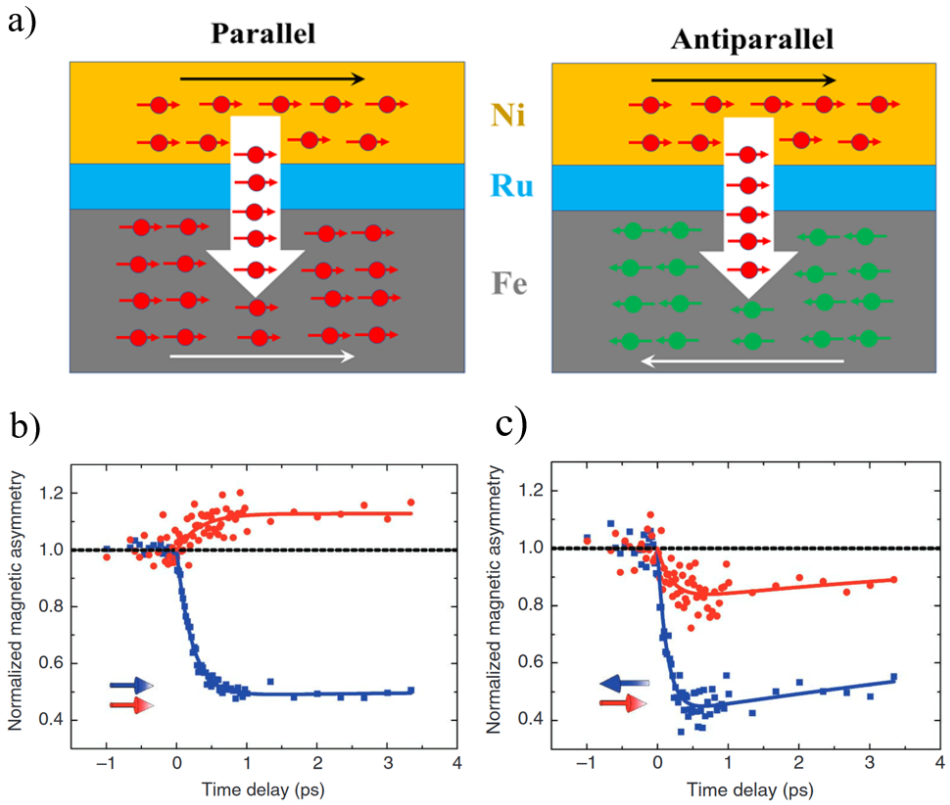

FIGURE 1.15: **Layer- and time-resolved magnetization of Ni and Fe layers (from [60]).** a) Illustration of parallel and antiparallel magnetization alignment of the Ni and Fe layers, where the red and green circles are the majority spin alignment in the layers, and the large white arrow represents the flow of the spin current. b) and c) corresponds to the time-resolved magnetization of the Fe (red) and Ni (blue) layers for parallel and antiparallel magnetization alignment, respectively.

process of ferromagnetic films on insulating substrates by comparing front-pump with back-pump measurements of a Ni/Al_2O_3 film. Therefore, the spin current is certainly not the dominant effect in the demagnetization of ferromagnetic Ni films.

1.4 Why X-rays for studying ultrafast magnetization dynamics?

The development of future technologies is based on the full understanding of the dynamics of nanoscale magnetic materials at ultrashort timescales. Therefore, light sources at short wavelengths with short pulses on the femtosecond timescale are desirable to probe nanoscale magnetic structures. With visible light, ranging from 400 to 800 nm, optical microscopy can only detect objects down to approximately 200 nm in size, which is already larger than the bit size used in commercial hard drives. Consequently,

there is a quest for light sources on the extreme ultraviolet (EUV) and soft x-ray range to probe nanoscale magnetic materials. EUV light ranges from 30 to 250 eV, and soft x-rays range from 250 eV to several keV, which allows a spatial resolution below hundred nanometers allowing applications such as microscopy [62] and lithography [63]. Here, the spatial resolution is small enough to study the hard drives structures up to an areal density of 10 Tbits/in^2 in EUV and 1000 Tbits/in^2 in soft x-rays, as schematically represented in figure 1.16.

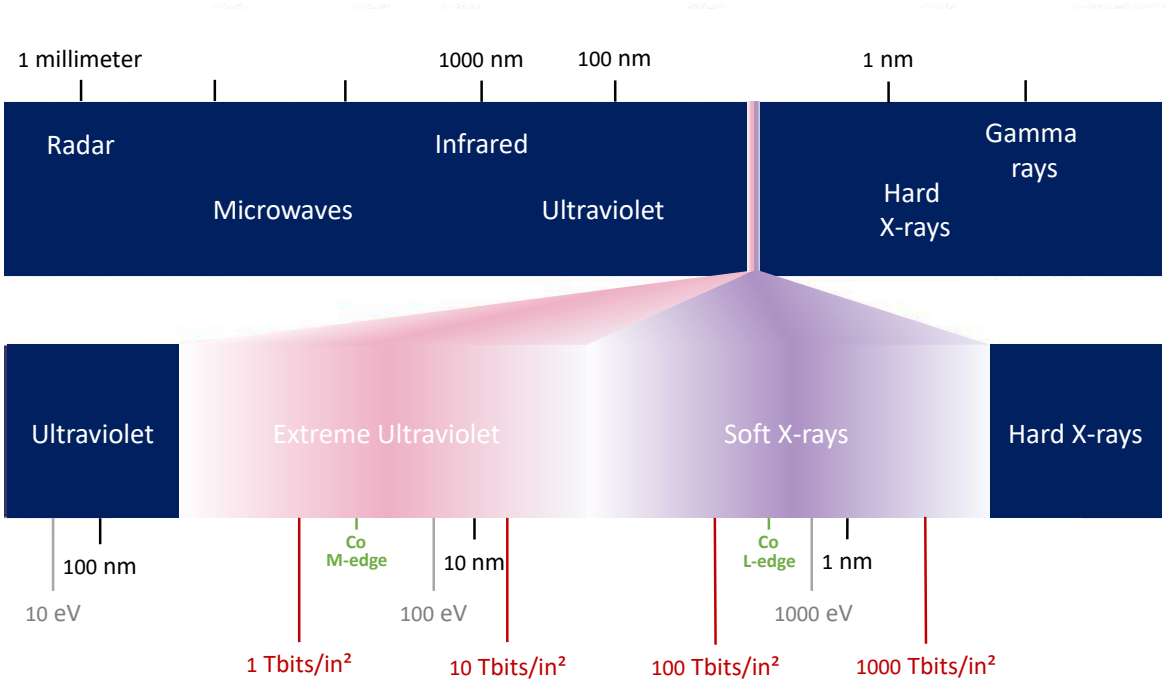

FIGURE 1.16: **Wavelength resolvable bit size and associated areal storage density.** EUV and soft x-ray range allow to study nanoscale magnetic structures with high resolution due to the their short wavelengths (black and gray for the wavelength and photon energy, respectively). The respective areal densities for different wavelengths are also represented (red). Additionally, the Co M and L absorption edges are represented in green.

From the scientific point of view, many interesting absorption edges of magnetic materials and rare earths correspond to the EUV and soft x-ray regions. The interaction of magnetism with light is studied through MO effects, as detailed in subsection 1.2. Near the EUV and soft x-ray absorption edges, the MO effects are greatly enhanced which allows the observation of very small effects. Furthermore, the absorption edges are unique for each element which is very useful in magnetism based applications, such as probing magnetization in an element-specific manner. For example, ferromagnetic elements, e.g., iron, cobalt, and nickel, have absorption edges located in EUV and soft x-ray regions. M absorption edges, where core 3p electrons are excited to the valence 3d

levels, are located at the EUV region. The soft x-ray region corresponds to L absorption edges, where deeper core 2p electrons are excited to the same valence 3d levels. In this thesis, we focused on the study of the M-edge of cobalt materials.

1.4.1 Typical experimental configuration

The ideal experimental technique should combine sensitivity to the magnetization state with femtosecond time resolution. In addition, it should allow element selectivity, meaning distinguish different materials in an alloy or a multilayer system, and image with nanometer spatial resolution (for future technological applications).

Typical experiments employ the pump-and-probe method. A femtosecond laser pulse in the optical range (pump) first excites a magnetic system. Then, a delayed second pulse (probe) of eletromagnetic radiation resolves the ultrafast dynamics in the material. Repeating this procedure for several time delays, a reconstruction of the temporal evolution of the excitation taking place in the medium is possible. The duration of the probe pulse defines the temporal resolution. The spectrum of the probe should be chosen according to the material absorption edges one is interested to investigate, far-infrared, optical, ultraviolet, or x-ray spectral ranges. Further complete information can be obtained while measuring the same phenomenon for the four different ranges. In my work, a probe pulse on the EUV/soft x-ray range is required for the investigation of the M absorption edge of cobalt-based materials.

1.4.2 EUV and X-ray sources around the world

Femto-slicing at sychrontron [64], [65], X-ray free-electron laser (XFEL) facilities [27], [66], and table-top HHG sources [60], [67]–[69] are complementary techniques with unique advantages. All of them present the nanometer-wavelength and femtosecond-pulse-duration requirements for element-selective studies of ultrafast magnetization dynamics. Synchrotrons and XFELs can probe high energy absorption L-edges. HHG probes mainly absorption M-edges but with the advantage of simultaneously probing the magnetic dynamics of multiple wavelengths and jitter free. In terms of output energy, femto-slicing and HHG sources are similar delivering up to 1 μJ, while FEL sources reach 100 μJ.

Traditional synchrotron radiation is generated by accelerating electrons bunches to relativistic speed and put them in a circular storage ring: when the path of the bunches is altered (acceleration) either by a bending magnet or an undulator, radiations are emitted covering the spectral range from infrared to hard x-ray. It presents a large photon flux and the pulse duration range from a few hundred picoseconds to nanoseconds. But in the slicing mode, the pulse duration goes down to $\sim$100 fs [70], which is adapted to capture ultrafast magnetization dynamics. XFELs provide very bright short-pulsed light across the electromagnetic spectrum. The process uses a linear accelerator for accelerating a beam of electrons close to the speed of light. The electrons pass through a long periodic arrangement of permanent magnets, which creates a sigmoidal magnetic field. This magnetic field forces an oscillating trajectory of the electrons and, consequently the emission of an electromagnetic wave train [71]. The main drawback of these large-scale light sources is the limited user accessibility because of the very small number of operational slicing beamlines and XFELs worldwide (figure 1.17).

More accessible light sources for extreme ultraviolet and soft x-rays are based on high-order harmonic generation. This table-top source was employed in the course of this thesis for studying magnetization dynamics of the M absorption edge of cobalt materials and it is described in detail in Chapter 2.

a)

b)

FIGURE 1.17: **Large-scale light sources.** a) XFEL (from [72]) and b) synchrotron (from [73]) facilities worldwise and in Europe, respectively.

CHAPTER 2

High order harmonic generation in gases

The generation of high order harmonics occurs due to a highly nonlinear optical process when an intense laser, typically 10^{14-15} W/cm^2, with some tens of *fs* pulse is focused in a gas. This is a non destructive and table-top source of spatially [74], [75] and temporally coherent [76] and polarized light, ranging from the ultraviolet (260 - 100 nm) to the soft X-ray region (100 - 10 nm) [77], [78]. HHG presents a wide range of applications, including nonlinear EUV optics [79], attosecond physics [80]–[82], EUV spectroscopy [83] or ultrafast magnetism [7]. This chapter presents the HHG, particularly the theoretical models, the general experimental approach and its importance for ultrasfast magnetization dynamics studies.

2.1 A suitable table-top source for ultrafast demagnetization measurements

Harmonic emission is a coherent nonlinear response of individual atoms, first observed in 1961 by Franken et al. [84] shortly after the demonstration of the first working laser by Maiman in 1960. The experiment consisted in focusing light from a pulsed ruby laser (at 694.3 nm wavelength, $\sim$ 3 J pulse energy and 1 ms pulse duration) into a non isotropic crystalline quartz sample. As a result, the second harmonic of the fundamental beam at 347.2 nm was generated with a very low efficiency conversion. This became the first experiment in the nonlinear optics field. In 1967, New et al. demonstrated the first third-harmonic generation in a gas [85].

High order harmonic generation was first observed by *McPherson et al.* [86] who successfully generated harmonic emission up to the 17^{th} order with a 248 nm radiation in neon gas. When it was first reported, the main research lied on understanding its physical phenomena [87]–[89]. It was then followed by the development of a coherent light source in the EUV region [90]–[92]. In the last 15 years, the main research topic was focused on attosecond science [93]–[95]. Basically, HHG is an elegant approach to achieve table-top sources of coherent light with the shortest flash of light, typically a few hundreds of attoseconds.

For a long time, no available tools were fast enough to resolve atomic and molecular dynamics, so HHG has become an important key in such investigation fields. However, the drawback of the HHG-based sources lies on the poor efficiency in their conversion of energy, 10^{-7} in neon [96], 10^{-5} in argon [97], and slightly below 10^{-4} in xenon, as well as the limitation to energies around a few hundred eV. But in order to time-resolve intra-nuclear dynamics it is necessary an advancement to shorter pulse duration and higher photon energies.

In addition, investigations of HHG polarization control have been performed, constituting an important tool in magnetic spectroscopy based techniques. HHG sources allow the investigation of ultrafast spin dynamics for up to a few femtoseconds jitter free temporal resolution. For example, it allows the reconstruction of the ultrafast laser-induced magnetic evolution. A new quantum control method [98] and spectroscopy method [99] in the EUV region are under development, which involve the active use of attosecond pulse trains.

2.2 Theory of the harmonics

2.2.1 Theoretical models

In a traditional optics theory, the low applied electric field (E) of the light and the dielectric polarization (P) of a material is given by a linear relationship:

$$P = \varepsilon_0 \chi E \tag{2.1}$$

where χ is the linear susceptibility and ε_0 is the permittivity.

For stronger electric fields (up to 10^8 V/m), the nonlinear terms in the induced polarization become important, which can be expressed by the Taylor series

$$P = \varepsilon_0 \chi^{(1)} E + \varepsilon_0 \chi^{(2)} E^2 + \varepsilon_0 \chi^{(3)} E^3 + ... \tag{2.2}$$

The first term defines the linear susceptibility and the next ones the nonlinear susceptibilities, which are small compared to the first one. Typically, only laser light is sufficiently intense to modify the optical properties of a material system. Its response to an applied optical field depends in a nonlinear manner on the strength of the optical field. When a very strong laser field is applied, a very high order of the polarization is induced. HHG is an extreme nonlinear optical process which occurs in the strong field regime. A completely new perturbative understanding of nonlinear optics is then necessary to describe the high order harmonics processes. Several models have been proposed to explain the occurrence of high order harmonics generated by individual atoms. The models are based on the behavior of a single atom exposed to the electric field of the laser. Two main approaches will be here discussed: a semiclassical model and a quantum model.

2.2.1.1 Three-step model: the semiclassical approach

The most successful description is the three-step model from *Corkum et al.* [87]. It is a semiclassical model since both quantum and classical approaches are used to describe the electron behavior. From quantum mechanics, a quantum particle presents an undulatory structure, which defines the measurement of the probability of finding the particle within a certain location. Therefore, the quantum approach describes the electron as a superposition of waves or a electronic wave packet. Classically, the model is based on the application of Newton's physics to study the movement of ionized electrons in the electric field of the linearly polarized driving laser. The three steps of the model are represented in figure 2.1. First, the gas interacts with the electric field of an intense laser beam, which lowers the potential barrier of the atoms of the gas (1). In every half optical cycle, an electron can be emitted by tunnel ionization and then accelerated by the laser field in the continuum, gaining kinetic energy (2). When the laser field changes the sign, it is slowed down and then accelerated towards its parent atom. Finally, when the electron passes near the atom, it has a certain probability to recombine

on the ground state (3). When the electron recombines, a photon, with energy equal to the one gained by the acceleration in the field plus the ionization potential, is emitted in the form of a strong and coherent HHG photon in the EUV. These three steps are described in more details in the next paragraphs.

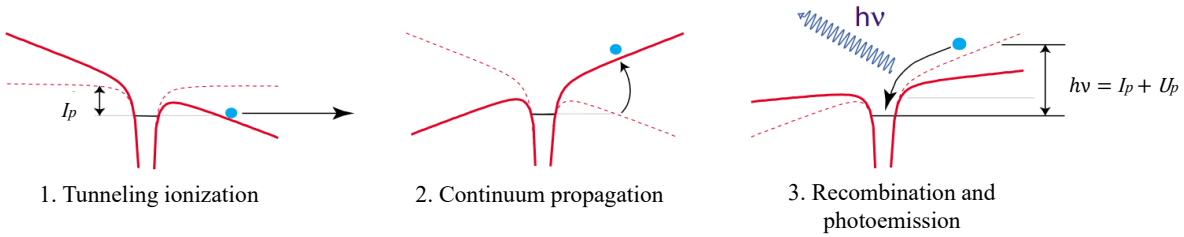

FIGURE 2.1: **Three-step model of high-harmonic generation with linear polarization in a gas (adapted from [100]).** 1, Distortion of the Coulomb potential due to the electric field of the focused laser, inducing tunnel-ionization of an electron. 2, The electron wave packet is accelerated away from the atom. 3, Due to electric field reversal the electron wave packet is accelerated back and then recombines with the parent ion when the field is nearly zero, leading to the emission of extreme ultraviolet radiation.

Tunneling ionization

One considers an isolated atom in the fundamental state. An electron in this condition is submitted to the Coulomb potential of the nucleus, $V_0 = -1/r$. Adding a linearly polarized electromagnetic field, $E(t) = E_x \cos(\omega_0 t) e_x$, where e_x and ω_0 corresponds to the polarization axis and the angular frequency of the field, the new potential becomes:

$$V(x,t) = V_0(x) + xE(t) \tag{2.3}$$

This leads to the lowering of the potential barrier on one side. If the field is strong enough, part of the electronic wave packet can cross the potential barrier by tunneling effect. This probability depends on the height, thickness and the time during which this barrier is lowered. By further increasing the intensity of the electric field, the potential barrier is completely removed, releasing the electron. This extreme case is called ionization regime by barrier suppression [101], [102].

Continuum propagation, recombination and photoemission

After tunneling out of the atom, we assume that the electronic wave packet dynamics is ruled only by the laser field, strong enough to neglect the long-range atomic

potential effects. We can then use the classical description of the electronic wave packet dynamics, where the Lorentz force is the only one acting on the electron:

$$m\ddot{x} = -eE_0 \cos(\omega_0 t) \tag{2.4}$$

For the initial conditions, t_i is the instant of the wave packet ionization, and one assumes $x(t_i) = 0$ and $\dot{x}(t_i) = 0$, meaning the movement across the tunnel barrier is neglected and all its kinetic energy is lost after crossing it. Integrating the equation 2.4:

$$\dot{x} = -\frac{eE_0}{m\omega_0}[sin(\omega_0 t) - sin(\omega_0 t_i)] \tag{2.5}$$

$$x = \frac{eE_0}{m\omega_0^2}[cos(\omega_0 t) - cos(\omega_0 t_i)] + \frac{eE_0}{m\omega_0} sin(\omega_0 t_i)(t - t_i) \tag{2.6}$$

The electron oscillates in the field in the direction e_x and periodically returns to x = 0, that is its parent atom, where it can recombine, emitting a EUV photon. The electron's trajectory depends on the time of its emission into the continuum. A photon is emitted only when the electrons leaves the atom at every half cycle of the driving laser (maximum and minimum of the laser field). The periodicity is then T/2, where $T = 2\pi/\omega_0$ is the period of the laser, corresponding to $2\omega_0$ in the frequency domain. The spectrum of the emitted radiation is therefore a harmonic comb up to a cut-off energy (see equation 2.13), described in detail in section 2.2.3, separated by $2\omega_0$. Moreover, since the generation medium is centro-symmetric, only the odd harmonics are emitted.

The three-step model gives a simple picture of the HHG process, successfully explaining the experimental observations, like the prediction of the cut-off region. However, a quantitative description requires more advanced quantum mechanical calculations, including a more realistic treatment of the atomic system. This is explained in further detail in the next section.

2.2.1.2 Lewenstein's model: the quantum approach

In 1994, Lewenstein *et al.* [89] proposes a fully quantum model of the single atom emission of HHG, which takes into account the quantum effects not included in the semiclassical model. In the semi-classical model, a single electron is considered to accelerate along a certain trajectory, by the electric field of the laser, while in this quantum mechanical description, an ensemble of trajectories will contribute to the wave packet.

This approach is based on the Strong Field Approximation (SFA). Considering only one active electron submitted to the electric field $\vec{E}(t)$, the Schrodinger equation is written:

$$i\frac{\partial \mid \psi(\vec{x},t)\rangle}{\partial t} = (-\frac{1}{2}\nabla^2 + V(\vec{x}) - \vec{E}\cdot\vec{x}) \mid \psi(\vec{x},t)\rangle \tag{2.7}$$

Lewenstein *et al.* solved numerically the time dependent Schrödinger equation in a strong field with the following assumptions:

- The contribution to the wave packet of all bound states except the ground state can be neglected,
- There is no depletion of the ground state,
- In the continuum states, the electron can be treated as a free particle moving in the electric field with no effect of the atomic potential.

The electron, propagating in the laser field, recombines with the parent ion by a dipole transition. The SFA approach assumes the calculation of the harmonic dipole moment as the coherent sum of all the different quantum paths that contribute to the harmonic emission. In addition, this model shows the dependence of the conversion efficiency on the laser wavelength and pulse duration. Lasers with shorter wavelength as well as lasers with shorter pulse duration, generate harmonics more efficiently. From these approximations, also the cut-off law is predicted,

$$E_{max} = I_p F(I_p/U_p) + 3.17U_p, \tag{2.8}$$

where U_p and I_p are the ponderomotive and the atom ionization potentials, respectively. The factor $F(I_p/U_p)$ is equal to 1.3 when $U_p \gg I_p$, and ~ 1 when I_p increases. This equation is in good agreement with both the semiclassical three step model and with experimental data.

2.2.2 Phase matching

An important property of HHG is its coherence, which arises because the phase of harmonic emission is locked to the laser phase. So, for example, if the laser has linear polarization, the harmonics will have linear polarization. But for a HHG conversion process to be efficient, it is crucial for the emission that all atoms are phase-matched

meaning that harmonics from different atoms have to be emitted with the same phase to allow for constructive interferences throughout the medium length (figure 2.2). In turn, the intensity of harmonic radiation will grow as square of the medium length. There is an additional phase shift between the fundamental laser field and the gener-

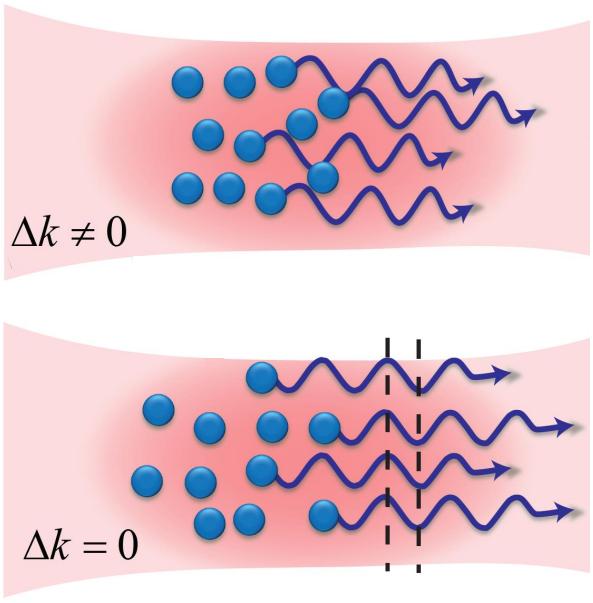

FIGURE 2.2: **Schematic representation of phase-matching (adapted from [103]).** Two cases of generation are represented: non-phase-matched ($\Delta k \neq 0$) and phase-matched ($\Delta k = 0$).

ated harmonics field, produced when the ionized electron transfers an additional phase acquired during its movement in the electric field. This can affect the properties of the resulted beam, such as angular distribution [104] or coherence [105], giving rise to the phase mismatch between them, which restricts the quadratic growth of the harmonic intensity with the medium length. The phase matching effect on the high order harmonics generated in gas medium was first studied in [106]. To maximize the emission, the wave vector mismatch, Δk, must be minimized. For a given harmonic order q, in conventional nonlinear optics, Δk is equal to

$$\Delta k = k_q - q k_L, \tag{2.9}$$

where k_q e k_L are the wave vectors of the harmonic field and fundamental laser, respectively. A useful parameter characterizing phase matching is the coherence length

$L_c = \pi/\Delta k$, which describes the propagation distance between two locations of harmonic emission that are exactly out of phase. Thus, within L_c the two fields, fundamental and harmonic, interfere constructively. Outside this limit, destructive interferences between them occur, meaning that at the end of the coherence length, there is a π phase shift between the two fields that was generated at the beginning of the coherence length.

With regard to the macroscopic emission corresponding to the HHG, the equation 2.9 must be considered in the strong field regime to include the harmonic dipole phase gradient [107]:

$$k_q = qk_L + \overrightarrow{\nabla}\phi_{EUV} \tag{2.10}$$

Minimization of the phase mismatch in HHG and optimization of its conversion efficiency has been studied extensively [105], [108]–[110]. There are four main contributions that can result to phase shift between the incoming laser beam and the generated harmonics:

$$\Delta k = \Delta k_g + \Delta k_a + \Delta k_p + \Delta k_d \tag{2.11}$$

The Gouy phase shift Δk_g contributes when a laser beam induces a geometrical phase mismatch associated with the rapid variation of the Gouy phase at the Gaussian beam focus. This gradient depends on the spatial coordinates and always takes negative values. The minimum value is at the beam focus, equal to $-q/z_R$, where $z_R = \pi\omega_0^2/\lambda$ is the Rayleigh length, with ω_0 the beam waist. Δk_a and Δk_p are due to the atomic and plasma dispersion, respectively, making different frequencies (fundamental laser and harmonics) travel with different velocities in the medium. Finally, the harmonic dipole phase gradient Δk_d is the partial derivative of the phase gained by the electron in the continuum, also leading to an atomic phase mismatch.

Furthermore, the medium where HHG are produced reabsorbs the radiation, especially in the EUV region of the spectrum. This limits the medium length to 5-10 times the absorption length [111]:

$$L_{abs}(\lambda) = \frac{1}{\rho_{at}\sigma_{abs}(\lambda)} \tag{2.12}$$

where ρ_{at} is the atomic density and $\sigma_{abs}(\lambda)$ is the absorption cross-section, decreasing with the harmonic order. The optimal conversion for the generation conditions is $L > 3L_{abs}$ and $L_c > 5L_{abs}$, where L is the medium length, as plotted in figure 2.3. In

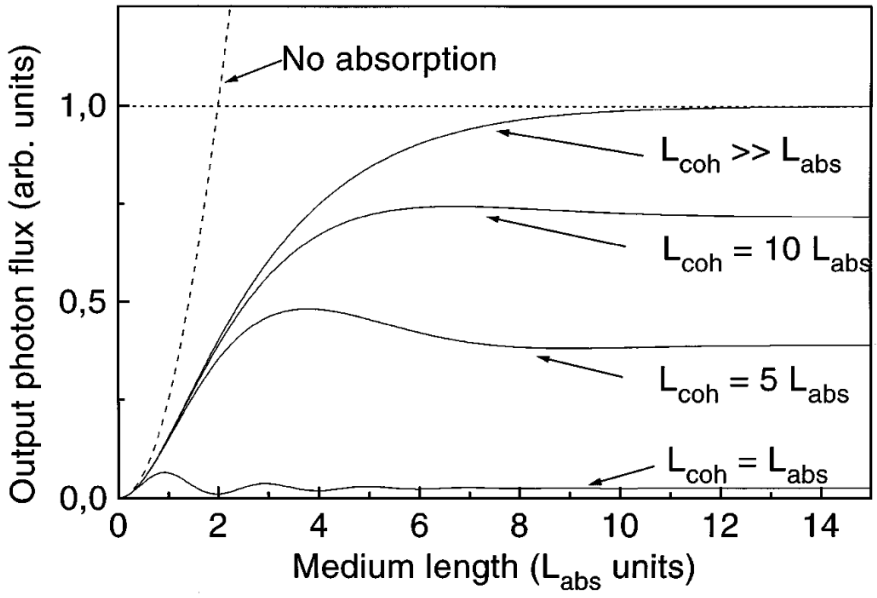

FIGURE 2.3: **HHG photon emission as a function of the medium length in units of absorption length (from [111]).** The dotted line refers to the no absorption case.

summary, the phase-matching terms are dependent on the setup parameters, the geometry, and the generation medium. And a change of one parameter often influences many phase-matching terms. Consequently, the optimization of the HHG generation requires a persistent readjustment so that all the setup parameters match.

2.2.3 Characteristics of the harmonics

2.2.3.1 Spectral properties

The harmonic radiation is emitted in the form of a comb of the odd multiple frequencies of the fundamental frequency of the driving laser (ω). Contrary to a continuous exponential decrease typical for perturbative nonlinear processes, three different spectral regions can be defined in the emission spectrum of HHG (figure 2.4). In the perturbative region ($3^{th} - 7^{th}$ harmonic) the intensity of each harmonic order drops rapidly, then levels out in a plateau of successive harmonics with similar intensity until a sudden cut-off within a few harmonic orders. The cut-off law which defines the maximum HHG photon energy generated from a single atom is determined by the sum of the atom ionization potential, I_p, and by the ponderomotive potencial, U_p:

$$E_{max} = I_p + 3.17U_p \tag{2.13}$$

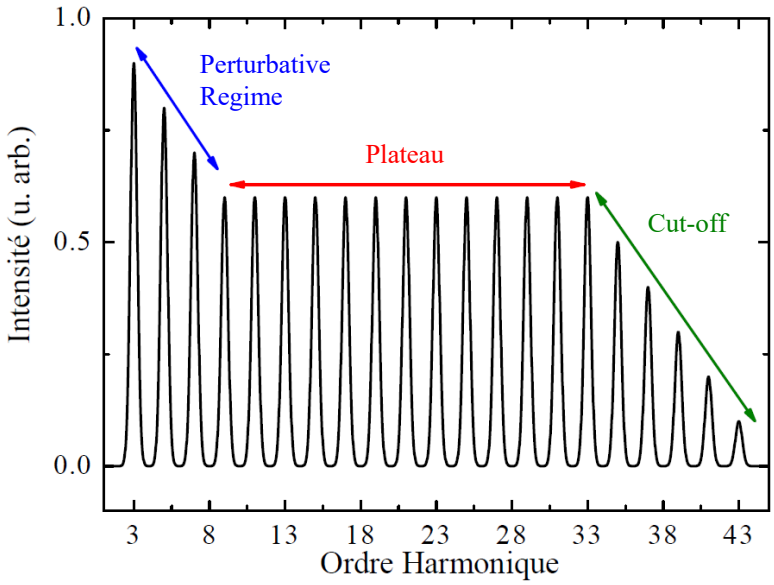

FIGURE 2.4: **Typical HHG spectrum (adapted from [112]).** The intensity drops rapidly for the first harmonics (perturbative regime), then levels out in a plateau with similar intensity until a sudden cut-off within a few harmonic orders.

The ponderomotive potential corresponds to the average energy of a free electron oscillating under the action of a laser field and can be given by

$$U_p = \frac{e^2 E^2}{4m\omega^2} \tag{2.14}$$

for a linearly polarized oscillating field, $E\sin(\omega t)$. Replacing E and ω by laser intensity, I_L, and wavelength, λ,

$$U_p \simeq 9.33 \times 10^{-14} I_L \lambda^2 \tag{2.15}$$

The numerical factor of 3.17 in equation 2.13 results from calculations of the dynamics of an electron interacting simultaneously with an external laser field and the atomic core, which agrees with a large number of experimental observations [87], [89]. The equation shows that the maximum photon energy increases with the increasing driving wavelength and laser intensity. This means that, in order to generate very short wavelengths, it is necessary to use a gas with a high ionization potential, generally a noble gas, and a driving laser with long wavelength and high intensity. But increasing the laser intensity too much risks to prevent the recombination of the ionized electrons with their parent ions and, thus the photon emission. This classical interpretation shows that in order to control HHG processes, one should try to control the motion of free electrons in the laser field. The highest photon energy depends on the generation

medium. Figure 2.5 schematically shows experimentally observed HHG spectra generated in gaseous media. Helium shows the largest cut-off energy among all noble gases, followed by Neon, Argon and Xenon. However, the number of photons significantly decreases for the gases with the largest cut-off energy. For this thesis, the characteristic wavelengths of interest are located around 60 eV corresponding to the cobalt M-edge. Observing figure 2.5, three gases are eligible. Neon is the gas with higher number of photons and, thus the one used to carry out our experiment.

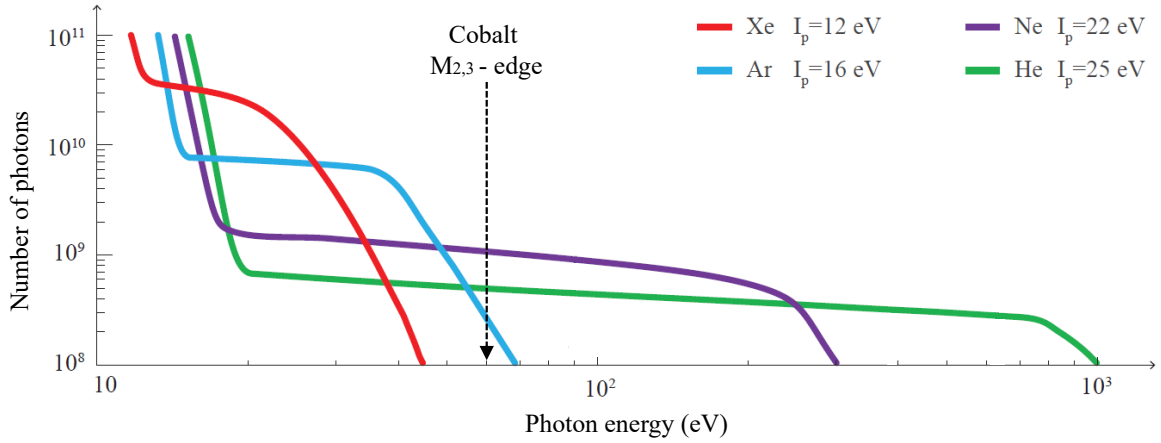

FIGURE 2.5: **HHG spectra for different gases (adapted from [103]).** The wavelength of interest for this thesis in the EUV range corresponds to the Cobalt $M_{2,3}$, located around 60 eV.

The three step model predicts that the odd harmonics are emitted at every half-optical cycle [113]. In the time domain, it represents the spacing between two harmonics of about one half of the laser optical cycle, $T/2 = 1/2f$, as represented in figure 2.6 a). Consequently, in the frequency domain, the spacing between harmonics is 2f (figure 2.6 b)). The high-harmonic pulse duration is determined by the number of optical cycles involved in the tunneling ionization. The symmetry of the medium prevents the generation of even-order harmonics. But the symmetry of the driving electric field can be broken by adding a weak second-harmonic field $\omega + 2\omega$, which is described as

$$E = E_0 \sin(\omega t + \phi(\omega)) + rE_0 \sin(2\omega t + \phi(2\omega)), \tag{2.16}$$

where $\phi(\omega)$ and $\phi(2\omega)$ are the phase of the fundamental and second harmonic fields and r is the amplitude ratio. Here, the generation of the laser pulses takes place at every full optical cycle [114], $T = 1/f$, which results in the generation of both even and odd

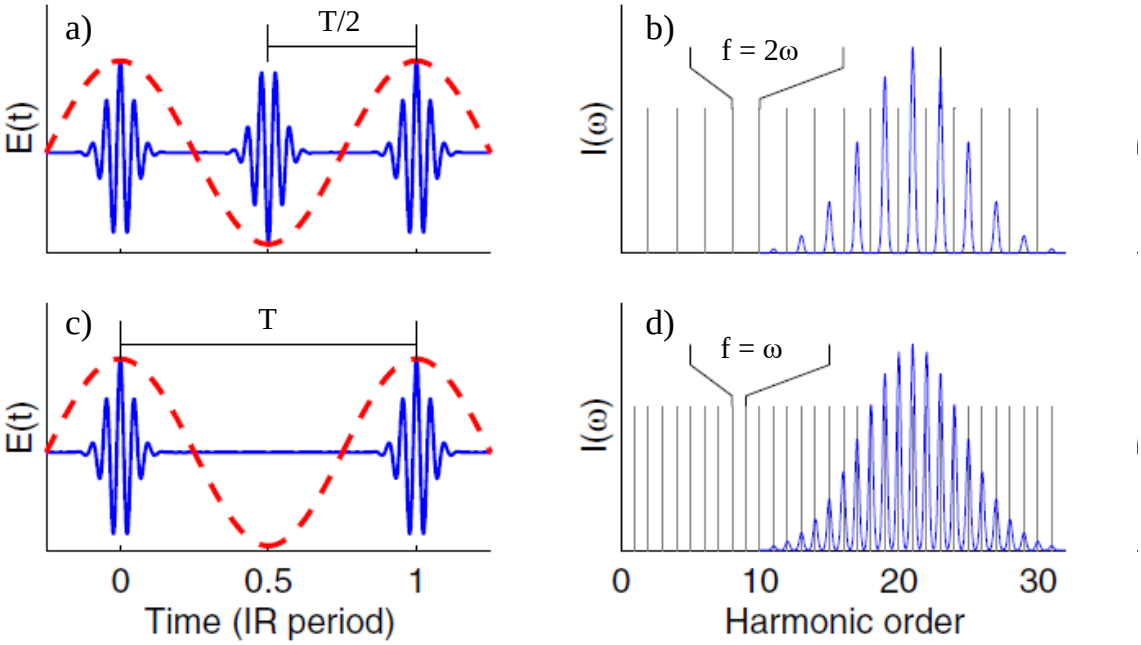

FIGURE 2.6: **Odd and even order harmonics generation (adapted from [113]).** a) and b) corresponds to a one color driving field resulting in a emission with periodicity equal to half of the driving field T/2, which gives a frequency of f=2ω, c) and d) corresponds to a two color driving field resulting in a emission with periodicity equal to the driving field T, which gives a frequency of f=ω.

harmonic orders (figure 2.6 c)). Consequently, the spacing between harmonics reduces to one fundamental frequency f (figure 2.6 d)).

2.2.3.2 Description of the harmonics polarization state

2.2.3.2.1 General concepts of polarized light

Consider the plane-wave solution to Maxwell's equations given by

$$\vec{E}(\vec{r},t) = \vec{E}_0 e^{i(\vec{k}\cdot\vec{r}-\omega t)}. \tag{2.17}$$

The wave vector $\vec{k}$ specifies the direction of propagation. If the wave is propagating in the direction $\hat{e}_z$ and the wave vector and the electric field are orthogonal, the electric field is transverse and will evolve according to $\hat{e}_x$ and $\hat{e}_y$. The field is then described as

$$\begin{cases} E_x(z,t) = E_{0,x}\cos(\omega_0 t - kz + \phi_x) \\ E_y(z,t) = E_{0,y}\cos(\omega_0 t - kz + \phi_y) \\ E_z(z,t) = 0 \end{cases} \tag{2.18}$$

with $E_{0,i}(i = x, y)$ the positive real amplitudes and $\phi_i(i = x, y)$ the phases defined within 2π. Combining the two first equations from 3.2 and eliminating t, the end of the electric field vector describes an ellipse,

$$\frac{E_x^2}{E_{0,x}^2} + \frac{E_y^2}{E_{0,y}^2} - 2\frac{E_x E_y}{E_{0,x} E_{0,y}} \cos\phi = \sin^2\phi \tag{2.19}$$

with $\phi = \phi_x - \phi_y$ the phase difference between the two components of the field defined on the interval $[-\pi, \pi]$. The polarization ellipse is represented in figure 2.7. The ellipse

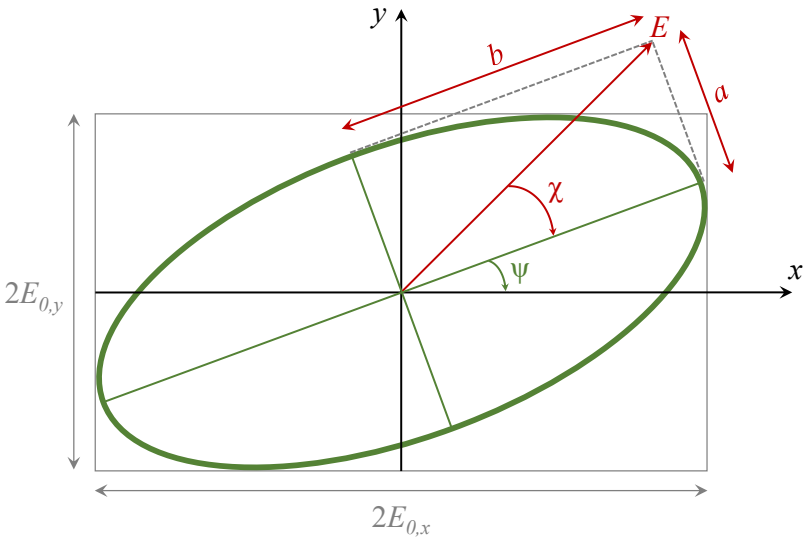

FIGURE 2.7: **Polarization ellipse.** The ellipse minor and major axes (a and b) gives the ellipticity of the field ($\varepsilon = a/b$).

can be described in terms of the ratio between its minor and major axes, a and b, which gives the ellipticity of the field, $\varepsilon = a/b$. The angle χ, ellipticity angle, is noted such that $\tan\chi = \varepsilon = a/b$ on the interval $[-\pi/4, \pi/4]$. The orientation angle, ψ, is the angle between the the x axis and the major axis a of the ellipse on the interval $[0, \pi]$. The ellipticity ε thus varies from 0 for a linear polarization to 1 for a circular polarization. If $\varepsilon > 0$, the wave is elliptically left polarized and carries a spin angular momentum of $\varepsilon\hbar$ per photon. For $\varepsilon < 0$, it is elliptically right polarized carrying $-\varepsilon\hbar$ per photon.

Three polarization states are represented in figure 2.8, which depends on how the electric field is oriented. Elliptically polarized light is the most general description of polarized light (figure 2.8 a)), where the electric field of the light describes an ellipse. The electric field corresponds to the sum of two linear components, perpendicular to each other with different amplitudes ($E_{0,x}$, $E_{0,y}$) and a phase shift (ϕ). The resulting electric field rotates elliptically around z and, depending on the rotation direction, it

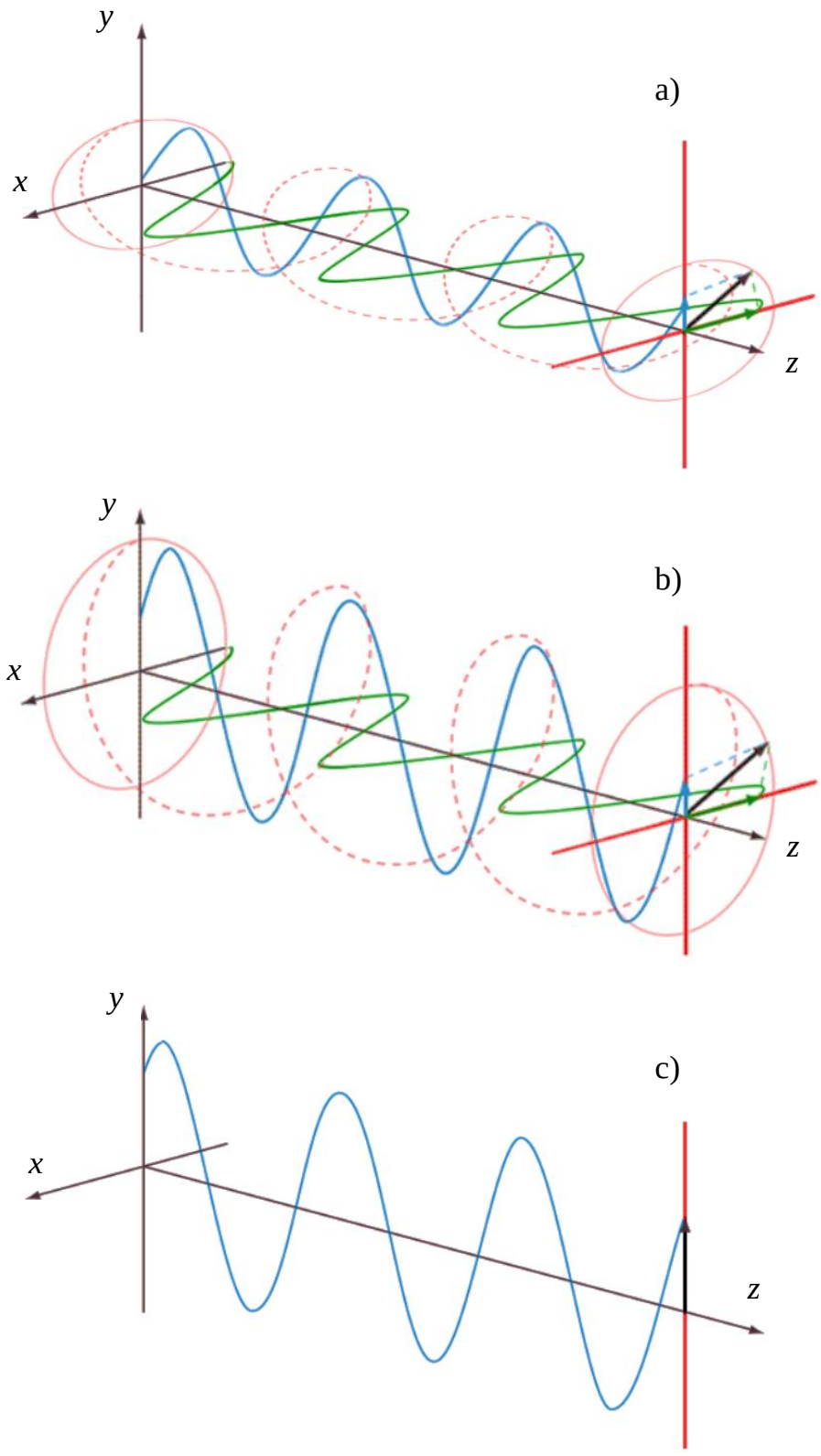

FIGURE 2.8: **Examples of polarization state (from [115]).** a) Elliptically polarized, b) circularly polarized, c) linearly polarized.

results in left- or right-hand elliptically polarized light. Circular and linear polarization can be considered as special cases of elliptically polarized light. Circular polarization (figure 2.8 b)) results from the combination of two linear components perpendicular to each other and equal in amplitude $E_{0,x} = E_{0,y}$, with a phase shift of $\phi = \pm\pi/2$. The electric field of the linearly polarized light (figure 2.8 c)) is confined to a single plane along the direction of propagation z. In this particular case, it corresponds to linearly vertical polarized light with $E_{0,x} = 0$.

2.2.3.2.2 Vector description of the light: Stokes-Mueller formalism

For purely monochromatic waves, the amplitudes, $E_{0,x}$ and $E_{0,y}$, and the phase difference ϕ are constant or slowly vary with time. Thus, the polarization ellipse remains fixed as the polarized beam propagates, corresponding to an instantaneous representation of polarized light. But in practice, these waves do not exist. The polarization state is well defined in every point and moment, but it quickly varies in time or space during the measurement. Furthermore, our detectors are too slow to follow their time evolution ($10^{-14} - 10^{-15}$ seconds). It is thus necessary to measure time averages defined by $\langle E_x E_y \rangle = \lim_{T \to +\infty} \frac{1}{T} \int_0^T E_x E_y \, dt$, where T is the integration time of the detector. Applying the time average definition to the polarization ellipse defined by equation 2.19, one obtain the formalism introduced in 1852 by George Gabriel Stokes [116]. He enunciates the mathematical formalism necessary to describe all the polarization states of light, including unpolarized or partially polarized light, via the Stokes parameters (S_0, S_1, S_2, S_3) defined as follows [117],

$$\vec{S} = \begin{pmatrix} S_0 \\ S_1 \\ S_2 \\ S_3 \end{pmatrix} = \begin{pmatrix} E_x E_x^* + E_y E_y^* \\ E_x E_x^* - E_y E_y^* \\ E_x E_y^* + E_y E_x^* \\ i(E_x E_y^* - E_y E_x^*) \end{pmatrix} = \begin{pmatrix} E_{0,x}^2 + E_{0,y}^2 \\ E_{0,x}^2 - E_{0,y}^2 \\ 2E_{0,x}E_{0,y}\cos\phi \\ 2E_{0,x}E_{0,y}\sin\phi \end{pmatrix} \tag{2.20}$$

The 4 Stokes parameters have a physical meaning in terms of intensities:

- S_0 describes the total intensity I_0 of the optical wave,
- S_1 describes the intensity preponderance of linearly horizontal (x-direction) over linearly vertical (y-direction) polarized light,

- S_2 describes the intensity preponderance of linearly polarized light in a plane rotated by $\pm 45^\circ$ with respect to the S_1 plane,
- S_3 describes the preponderance of right circularly over left circularly polarized light.

If the light is completely polarized, $S_0^2 = S_1^2 + S_2^2 + S_3^2$. For the case of no polarized light, $S_1^2 = S_2^2 = S_3^2 = 0$. Finally, if the light is partially polarized:

$$S_0^2 \geq S_1^2 + S_2^2 + S_3^2 \tag{2.21}$$

It is thus possible to define the degree of polarization of the field, given by:

$$P = \frac{I_{pol}}{I_{total}} = \frac{\sqrt{S_1^2 + S_2^2 + S_3^2}}{S_0} \tag{2.22}$$

P describes the two components of the partially polarized light, the completely polarized light (I_{pol}) and the non polarized one (I_{npol}), so that $I_{total} = I_{pol} + I_{npol}$. Thus, it varies between 0 for unpolarized light and 1 for full polarization. Figure 2.9 shows the some typical polarization states. The Stokes parameters can be written in function of the orientation and ellipticity angles (χ and ψ in figure 2.7) as follows,

$$\begin{pmatrix} S_0 \\ S_1 \\ S_2 \\ S_3 \end{pmatrix} = S_0 \begin{pmatrix} 1 \\ \cos 2\chi \cos 2\psi \\ \cos 2\chi \sin 2\psi \\ \sin 2\chi \end{pmatrix} \tag{2.23}$$

And,

$$\begin{aligned} \psi &= \frac{1}{2} \tan^{-1}\left(\frac{S_2}{S_1}\right), 0 \leq \psi \leq \pi, \\ \chi &= \frac{1}{2} \sin^{-1}\left(\frac{S_3}{S_0}\right), -\frac{\pi}{4} \leq \chi \leq \frac{\pi}{4} \\ \varepsilon &= \tan \chi. \end{aligned} \tag{2.24}$$

Another description method of the polarization light appeared in the middle of the 20^{th} century, the formalism of Mueller's matrices [118]. This formalism calculates the Stokes parameters of the light transmitted by an optical assembly. It uses the matrix calculation, to obtain the state of polarization and the intensity of the monochromatic light

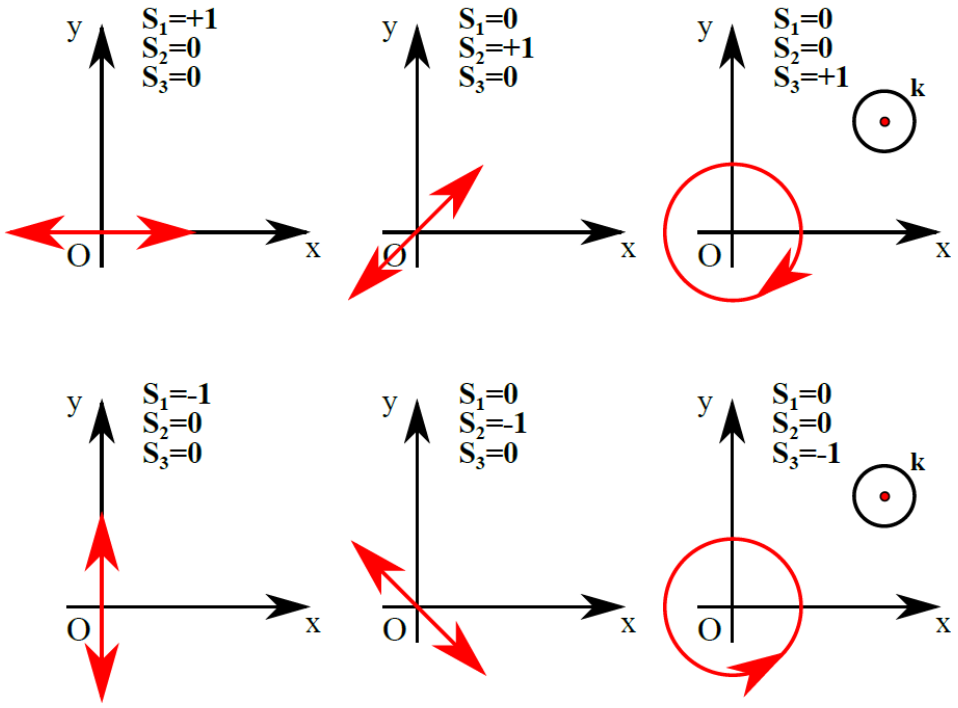

FIGURE 2.9: **Polarization state of the light.** Examples and sign conventions of the polarization state for a light beam propagating towards the observer (from [112]).

transmitted by complex optical assemblies, containing polarizers and birefringent media. Mueller showed that the incident $\vec{S}_i$ and transmitted $\vec{S}_f$ Stokes vectors are related in an optical system:

$$\vec{S}_f = M\vec{S}_i, \tag{2.25}$$

where M is the Mueller matrix that represents any optical element. By knowing this matrix, it is possible to predict the transmitted polarization state by knowing the incident one. For n optical elements in an experimental apparatus, the Mueller matrix is given by

$$M = M_n \times M_{n-1} \times ... \times M_2 \times M_1, \tag{2.26}$$

where each matrix corresponds to different optical elements.

2.2.3.2.3 Elliptically polarized high-order harmonics

The harmonic beam properties are most of the time similar to the driving laser properties. Therefore, one can control the harmonics ellipticity by the driving laser ellipticity. First observations of this method were made shortly after the HHG discovery [119],

[120]. But the generation of elliptical polarized light from an IR beam elliptically polarized shows a very low conversion efficiency, especially for applications. This is due to the trajectories of the emitted electrons and their low probability of recombining with the parent ions [121].

Yet, sources of elliptical polarized light are very interesting for many applications in different fields, and especially here for magnetism [122]. In order to obtain high order harmonics elliptically polarized, different techniques are possible:

- Generation in aligned molecules [123], [124],
- EUV polarizer [3], [125],
- HHG driven by a two-color laser field [2], [126].

The first technique uses a set of molecules aligned with respect to the polarization axis of the laser, presenting an asymmetry of the generation medium. This method is quite inflexible, needs to align molecules and provides a relatively low ellipticity. In addition, the need of an alignment pulse frequently creates spatial and temporal inhomogeneities, which make difficult the generation of high polarized harmonics. The second technique lies on the generation of linearly polarized harmonics followed by the harmonics propagation through a device that consists in a set of optics comparable to a quarter-wave plate. With this technique, a high degree of ellipticity is obtained. However, the low transmission of the device and its limitation to photon energies below 70 eV, reduce its use for applications. The last technique, HHG driven by a two-color laser field, which produces an intense and high elliptical harmonic beam, is frequently used for magnetic applications, namely the measurement of the magnetic circular dichroism. Two variations of this technique are described below in more detail.

Developed in our group [2], the first variation of this technique uses a cross-polarized two-color laser field, where the second field refers to the second harmonic (2ω) of the fundamental field (ω). The setup is compact and simple, only involving a frequency doubling crystal to obtain the second harmonic (figure 2.10 a)). The orthogonally polarized ω and 2ω laser fields are focused in a centrally symmetric gas medium, generating both odd and even harmonic orders at short wavelengths (here up to 70 eV) with an ellipticity degree up to 75%.

The observation of the XMCD effect requires a very high degree of elliptical polarized light, especially in time-resolved experiments. Consequently, our two-color laser

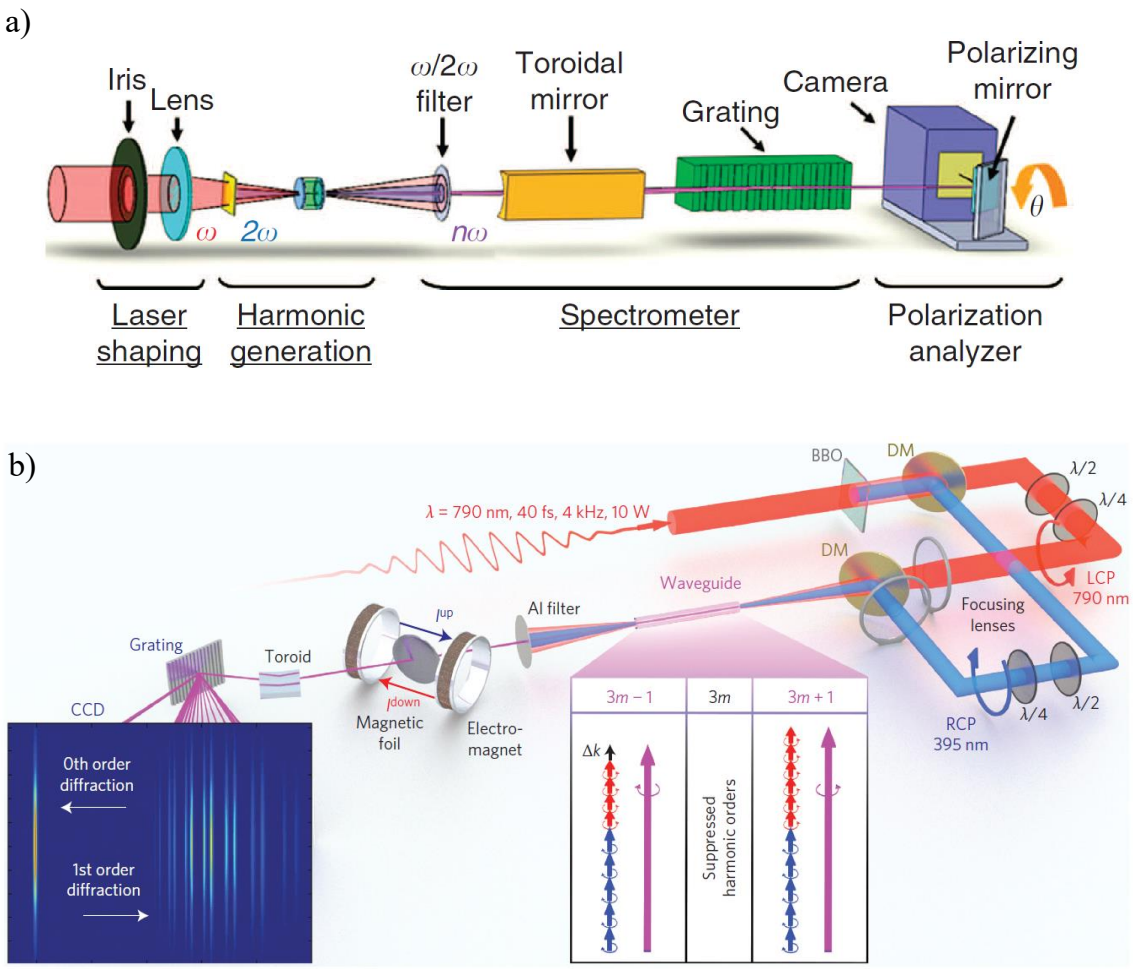

FIGURE 2.10: **Experimental setups for elliptically polarized harmonics.** a) Cross-polarized two-color laser field (from [2]), and b) co-propagation of bi-chromatic counter-rotating circularly-polarized laser pulses (from [126]).

field technique requires deeper investigations and, particularly, complete polarimetry has to be performed. In a first step, this was done for a low-order harmonic, the 4^{th} harmonic at the beginning of my PhD. Two main reasons led to the accomplishment of this research. First, HHG can be employed for seeding free-electron lasers. In our two-color configuration, the harmonic content is doubled and a higher number of photons is produced, which makes it an ideal source for seeding. The aim was using our seeding source in the plasma-based FEL experiment, also taking place at LOA [127]. Second, the experimental realization for a complete polarimetry of low-order harmonics is simpler than for high-order harmonics. Deepen the knowledge of the low-order harmonics polarization may provide a first overview of the polarization dependence of high-order harmonics. The experimental setup as well as the main results and conclusions are discussed in detail in Appendix A.

The second variation of the technique, nowadays known as the reference technique, achieved higher degree of ellipticity [126]. Bright circularly polarized high harmonics are generated by co-propagating bi-chromatic laser beams, the fundamental and second-harmonic, that are circularly polarized with opposite helicity in a gas-filled hollow waveguide. A photon flux of $\sim 1 \times 10^9$ HHG photons per second per harmonic is obtained, which is comparable to the linearly polarized HHG flux used in magneto-optical HHG-based experiments. However, experimentally, it is much more complex to setup (figure 2.10 b)).

2.3 Fundamental apparatus for HHG at LOA

Here I provide an overview of the experimental HHG setup used to carry out all the research presented in this thesis. It was assembled at the *Laboratoire d'Optique Appliquée (LOA)* from scratch using a newly purchased laser. Important components of the experimental apparatus are described below.

2.3.1 Laser system and laboratory environment

The laser source used in the experiment is a commercial system produced by Coherent, the Legend Duo Elite version (figure 2.11 a). It is based on the chirped pulse amplification technique [128], [129] using a Ti:Saphire as a gain medium. Briefly, a very short-duration pulse is generated and then stretched, significantly reducing its average power. The next step is to amplify this pulse and finally compress it to near its original duration. The IR laser system used in our experiments provides pulses centered at 800 nm, pulse duration of 30 fs and maximum energy of 3 mJ operating at 5 kHz.

This newly purchased laser was installed in a restored laboratory with distinct rooms, redesigned to set it up there. The noisy components of the laser, such as the chiller system, are installed in a small room connected to *salle Argent*, which is the laser room. This reduce vibrations and temperature variations, creating thus a more comfortable environment to work. Additionally, a control room (figure 2.11 b) was built apart from the laser laboratory so we can perform the experiments with the least possible perturbations. The laser is used simultaneously in two different beamlines in the fallowing way: 1 kHz for a beamline in *Salle Argent*, and 4 kHz for our high-harmonic beamline in the next room, the *Salle Corail*. The beam is transported in a vacuum tube from *salle*

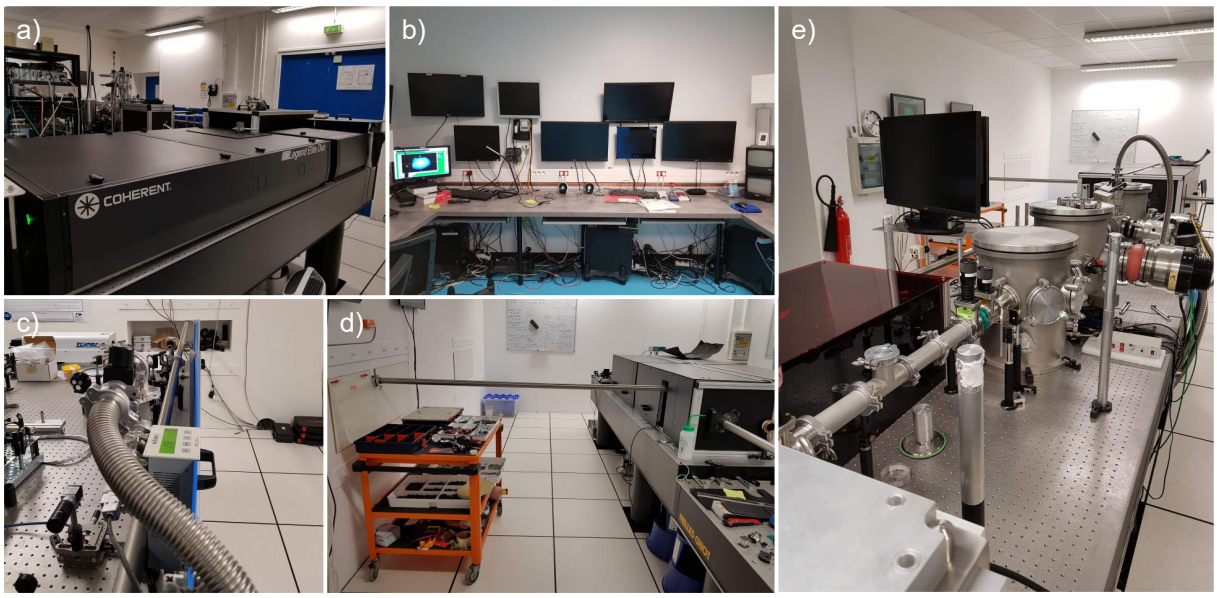

FIGURE 2.11: **Photos of the laboratory environment.** a) Laser system in *salle Argent*, b) control room outside of the laboratory, c) vacuum pump and tube in *salle Argent* which transport the laser to d) *salle Corail* and, e) the entire experiment line in *salle Corail*.

Argent (figure 2.11 c) to *salle Corail* (figure 2.11 d) within 5 m, in order to reduce its propagation in the air. Here, the beam can be divided in two parts: *i)* 90% for the generation of high order harmonics and *ii)* 10% for the pump to induce demagnetization dynamics in time resolved experiments, detailed in the next chapter.

2.3.2 IR optical system dedicated to HHG

The experimental set-up is conceptually simple and involves only the focusing of a sufficiently high-energy laser pulse into a gaseous medium (figure 2.12). After the laser exit in *salle Argent*, the beam passes through a telescope (divergent and convergent spherical mirrors) in order to increase the beam diameter. This step was implemented since the original diameter of the laser led to nonlinear interactions with the fused silica window, placed at the entrance of the vacuum tube that transports the laser until the *salle Corail*. These nonlinear interactions would result in an increase of the pulse duration which is a limitation for our experiment. At the beginning of the experimental line in *salle Corail* we start by shaping the laser beam, adjusting its diameter using an iris. Then, its horizontal polarization (p-direction) is changed to vertical polarization (s-direction) by using a periscope, which is composed of two IR mirrors, in order to adjust the beam height between the two rooms. Four IR mirrors, optimized at 800 nm

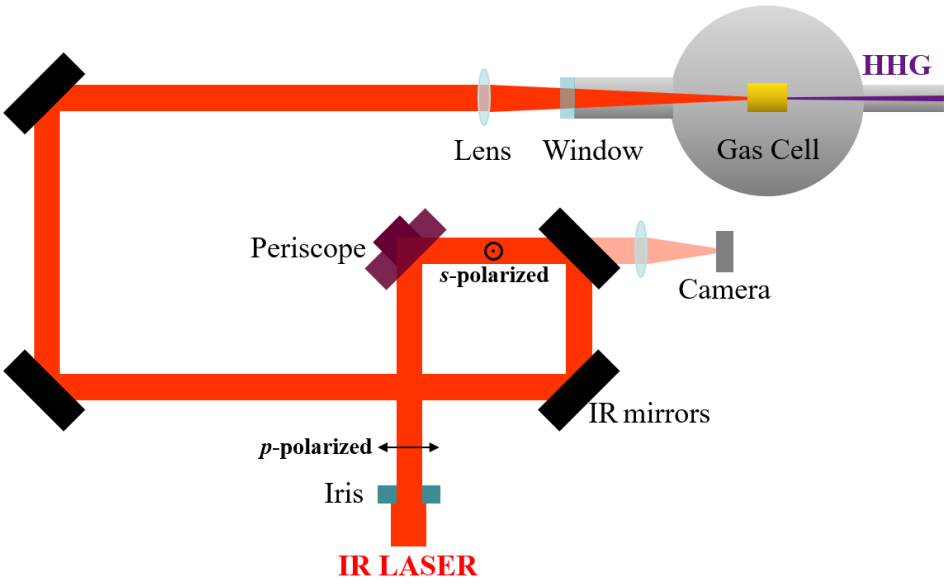

FIGURE 2.12: **Schematic generation of high-order harmonics in a gas cell.** At the beginning of the experimental line, the laser is *p*-polarized, changing then to *s*-polarized using a periscope. The transmitted light through the first IR mirror is focused in a camera to help in the alignment of the laser beam. The beam is then focused in a gas cell in vacuum where the generation of the harmonics occurs.

for a pulse duration of 30 fs, are used to redirect the beam into the harmonic generation axis. A small part of the beam, which is transmitted through the first IR mirror, is focused into a camera to help in the beam alignment. The beam is then focused by a lens into the gas cell, which is in vacuum since the EUV light is strongly absorbed by gases and all the materials. The focus of the lens can be controlled manually by means of a micrometer screw. The laser beam enters in the vacuum chamber through a fused silica window to minimize dispersion and nonlinear effects and interact with the gas during a small region near the focus. The generated harmonics are perfectly synchronized with the driving laser.

The relatively low pulse energy requires a tight focusing to ensure intensities focus of the order of 10^{14-15} W/cm^2. In our beamline, a lens with a focal distance of 1.8 m was used. The picojoule energy level of a single harmonic pulse is compensated with the high repetition rate of the laser, in terms of beam power. The access to ultrashort pulses of 30 fs allows a more efficient harmonics generation than longer pulses.

The transverse profile of the IR beam is Gaussian, with a diameter of around 20 mm. For a perfect Gaussian beam propagating on the z axis, the beam radius $\omega(z)$, defined

at $1/e^2$ corresponding to 86% of the total power, is equal to

$$\omega(z) = \omega_0 \sqrt{1 + \left(\frac{z}{z_R}\right)^2}. \tag{2.27}$$

By clipping the beam with an iris, a better compromise for an efficient harmonic generation can be achieved. However, the Gaussian profile turns in a truncated Gaussian one. This can significantly affect the focusing geometry [130], the size of the focal spot and, consequently, the intensity. The Gouy phase is also different for truncated Gaussian beams, which in turns affects the phase matching conditions [131] and thus the conversion efficiency. In our case, a diameter of $\sim$17 mm was used for the harmonics generation, giving as well a more circular intensity profile, and a more stable source.

2.3.3 HHG systems

The harmonics generation in gases was achieved using several high-pressure systems, such as gas jets [132], gas cells [133] and gas-filled capillaries [134]. In our experiment, the gas cell is a simple system to install which gives temporal stability. The uniform density over the whole interaction region is the biggest advantage, providing a longer interaction length and self-guiding mechanisms to enhance the laser intensity along the interaction length. The two sides of the gas cell are sealed with thin Al foils which are punctured by the focused laser making holes for entrance and exit. The gas cell is installed in the middle of the interaction chamber and the release of the gas is made by a debit regulator of gas from Bronrkhorst (figure 2.13 a)).

The size and geometry of the gas cell are important for the harmonic generation. A longer gas cell provides a higher volume interaction between laser and gas but it risks an high absorption of the harmonics. Its length can be chosen with respect to the Rayleigh length z_R of the focused IR beam, which is related to the lens focal length, f, by

$$z_R = 4\frac{\lambda f^2}{\pi D^2} \tag{2.28}$$

where D is the beam diameter before the lens. In general, the best gas cell length is the one close to the confocal parameter $b = 2z_R$ of the driving laser, which corresponds to $b \simeq 23$ mm in our experiment. A few gas cells with different sizes were tested in the experiment. Initially, a cylindrical gas cell made of aluminum, with 8 mm of diameter,

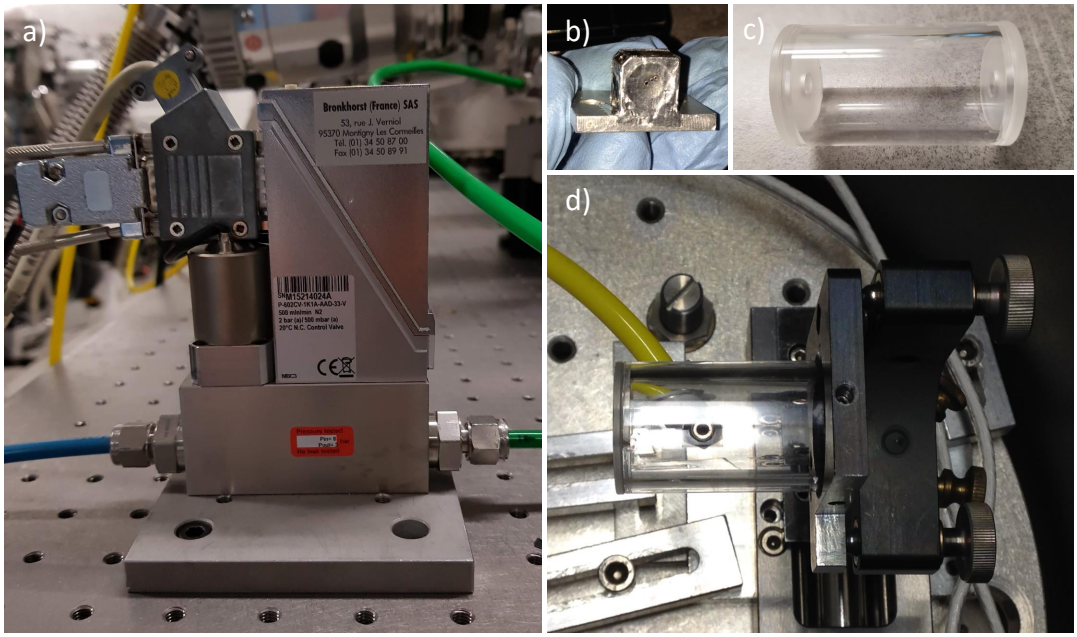

FIGURE 2.13: **Gas cell photos.** a) Gas debit regulator, b) first type of gas cell in aluminum, c) second type of gas cell in PVC, d) gas cell holder where the yellow tube corresponds to the entrance of gas in the cell.

was used (figure 2.13 b)). Its length is smaller than the parameter b, around 10 mm. Besides the low harmonics intensity and the temporal stability, the big issue of this type of gas cell was the impossibility to achieve higher photon energies for our experiment (up 70 eV). Then, we designed cylindrical gas cells, considerably bigger in volume with different lengths, 20, 30 and 40 mm, represented in figure 2.13 c). The cylindrical gas cell with 30 mm provided the best compromise for the harmonics generation along with large temporal stability. As expected, this gas cell length agrees with the assumption of being close to the confocal parameter b. Regarding the geometry of the gas cell, we cannot conclude about its importance for the generation efficiency since we did not test different gas cell geometries in the same conditions. Figure 2.13 d) shows the respective gas cell holder inside the generation chamber, where the yellow tube allows the entrance of gas. The holder system is placed on a motorized horizontal translation stage.

With respect to the gas pressure, its increase leads to a fast improvement of the conversion efficiency. However, high pressures can lead to the saturation of the efficiency or decrease due to absorption in the gas [135]. In our particular experiment, the more adequate pressure of neon was 110 mbar.

The harmonics generation and propagation have to be done under vacuum, in order to evacuate the generating gas and to avoid the absorption of the EUV light by the air. Four vacuum chambers and four turbomolecular pumps connected to four primary vacuum pumps are used in our experimental apparatus. The previous described harmonic generation occurs in the first vacuum chamber (figure 2.14 a)). During the harmonic generation process, the vacuum drops to 10^{-3} mbar. Here, two turbomolecular pumps connected to two primary pumps are used.

2.3.4 Application section

After the harmonic generation, the remaining IR beam propagates collinearly with the harmonics being several order of magnitude more intense. In the second and third

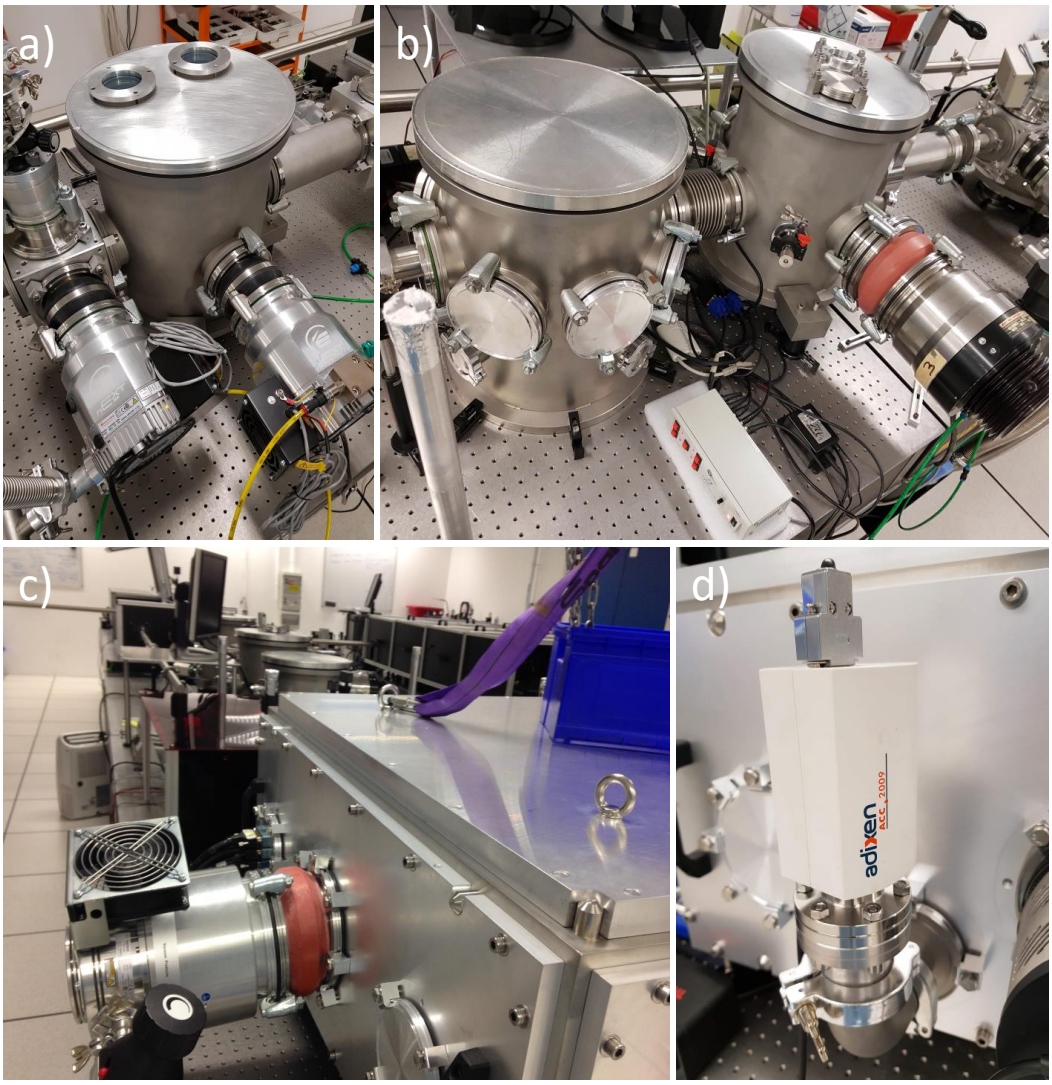

FIGURE 2.14: **Vacuum chambers photos.** a) Generation chamber, b) IR removal chambers, c) Faraday effect apparatus chamber, d) pressure gauge.

vacuum chambers,to remove the remaining IR light, SiO_2 mirrors at grazing incidence and aluminum filters, which can transmit the desired wavelength range, are used (figure 2.14 b)) However these filters also reduce the energy of the transmitted harmonics by $\sim 50\%$, depending on the spectral range and the filter thickness. In addition, the surfaces of these filters generally creates a thin oxidation layer, usually close to a few nm, further reducing their transmittance [136]. Aluminum filters with thicknesses of 150 to 300 nm are used in our experiment. Then the harmonics are focused by a toroidal mirror in the last vacuum chamber (figure 2.14 c)). The pressure inside the vacuum chambers during operation is measured by a pressure gauge (figure 2.14 d)) and it reaches the order of 10^{-5} mbar within 15 min. Inside this last chamber a Faraday effect detection is installed. This part is detailed in subsection 3.2.4. To perform this experiment, a spectrometer is needed. The spectrometer is composed of a reflective diffraction spherical grating with a groove density of 1000 gr/mm. In order to reflect a significant part of the EUV light, the grating is used in grazing incidence at $\sim 3°$, manually implemented by means of a micrometer screw. Here, the harmonic orders are spatially separated and

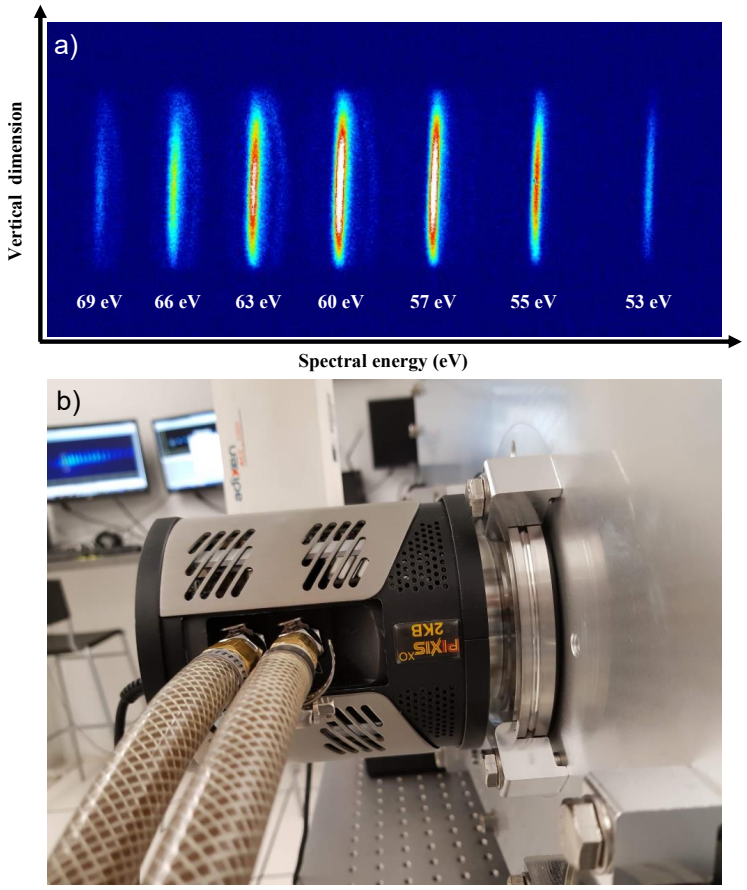

FIGURE 2.15: **HHG spectrum.** a) Spectral distribution obtained in Ne, and b) CCD camera.

focused in a charge-coupled device (CCD) camera. The CCD camera, manufactured by Princeton Instruments, with 2048x2048 square pixels of 13 μm, detects the harmonics (figure 2.15 b)). The high speed readout is 2 MHz (16 bit) for rapid image acquisition and the low speed readout is 100 kHz (16 bit) for high signal to noise ratio. In order to minimize the thermal noise, it is cooled between -30 and -40 °C. The data acquisition is controlled by Princeton Instruments WinView software. Figure 2.15 a) shows a typical spectrum obtained in our beamline, showing the harmonics from 53 to 69 eV. An extra caution is to prevent the fundamental light of hitting the camera, which easily saturates.

2.4 Potential optimization of our HHG source for magnetism studies

The experiments in magnetism usually require high number of photons, principally if the sample is in a transmission configuration, as in the case of the Faraday effect studied in this thesis. Therefore, an important characteristic of any laser-driven source is its conversion efficiency [137], which is strongly influenced by many factors collectively. For the HHG in gases, it is usually very low and simultaneously dependent on the laser intensity, atomic density, and medium length. The optimization of the phase-matching conditions can improve the conversion efficiency. For example, loose focusing geometry to obtain longer Rayleigh lengths will increase the interaction volume (between laser and gas), and in turn, increase the energy output as long as the phase matching is kept. Ideally, if the HHG from individual atoms are fully phase matched, then the number of photons will increase quadratically with the medium pressure. But the nonlinear interaction between lasers and gases leads to dispersion and absorption of the harmonics by the medium [111], [138], [139]. Better conversion efficiencies have been reported such as 1.5×10^{-5} [140] in argon and 4×10^{-5} [111] in xenon. The use of a non-Gaussian or a modified Gaussian beam for generation of high-order harmonics can also improve the conversion efficiency [141]–[144]. A combination of Bessel and Gaussian beams can be used to optimize the HHG process [143], [145].

Besides the conversion efficiency, pushing the cut-off energies to higher photon energies (X-ray region) is very important for magnetism studies. The use of gases with higher ionization potential, such as helium and even neon, leads to higher harmonic

order in the cut-off region [77]. Also using ionized argon instead of neutral argon provided very high order harmonics up to 250 eV [146]. However, higher ionization potential also leads to low photon flux. Another technique to significantly extend the cut-off photon energy of the high order harmonics is the use of a longer wavelength driving laser. T. Popmintchev *et al.* [147] showed photon energies up to 330 eV by using a mid-infrared laser with a pulse wavelength of 1.3 μm.

CHAPTER 3

Towards ultrafast magnetization dynamics: Faraday effect using HHG

This chapter culminates the previous two chapters in an experimental realization of a technique based on the magneto-optical Faraday effect, which describes the interaction between light and a magnetic field in a medium. We demonstrate that contrary to common believe linearly polarized EUV radiation, particularly HHG, can be employed in absorption spectroscopy to characterize a sample's ferromagnetic state. Here, the evolution of the conducted experiment is presented in detail, from the initial idea to its last version. Static and time resolved measurements are reported around the magnetically dichroic cobalt $M_{2,3}$ absorption edge (60 eV) in CoDy and Co/Pt samples.

3.1 Introduction

The phenomenon of ultrafast magnetization has been studied employing mainly pump-probe techniques using visible light. The specificity of our work is to study the ultrafast magnetization dynamics using X-rays. Indeed, the MO effects are greatly enhanced near the EUV (and X-ray) absorption edges, which allow the observation of very small effects, due to the spin–orbit interaction and exchange interaction of the core levels and of the valence bands of the transition metals or rare earths [20]. Additionally, since the photon energies of the samples absorption edges of interest correspond to very short wavelengths (of the order of a few nanometers) we obtain much higher spatial resolution with X-rays compared to the optical probe.

Most commonly, the traditional synchrotron radiation is used as a source of X-rays for magnetism studies in matter. However, as discussed in subsection 1.4.2, its temporal resolution is intrinsically limited to *ps* level because it delivers pulses of a few tens of picoseconds. For the study of ultrafast magnetism, femtosecond time resolution is required, which makes the femto-slicing mode at sychrontron, FELs and HHG sources good alternatives. HHG sources have been established over the past decade as powerful tools to investigate ultrafast charge and spin phenomena [5], [7]. Particularly, these sources allow element-selective investigations of the magnetic properties of the materials and of their magnetic domain structures as well as the investigation of the materials' demagnetization evolution [7]. These investigations are possible due to its potential for very high time resolution. Indeed it is uniquely limited by the length of the employed pump pulse, beneficiating from no jitter between pump and probe beams, since both pulses are derived from the same laser source. The polychromaticity enables simultaneous probing of individual dynamics in compound materials. Although FELs and femto-slicing lead to shorter wavelengths and higher fluency compared to HHG sources, huge facilities with very high value of construction and maintenance are required. Only a few FELs are implemented around the world and so, the respective beamtimes are limited and short in duration (1-2 weeks). On the contrary, HHG appear as laboratory scale sources, evolving toward shorter wavelength, higher efficiency and higher repetition rate.

For studying magnetization phenomena, HHG -based techniques are commonly used in two different approaches regarding the polarization of the light, whether it is required elliptically or linearly polarized. Elliptically polarized light allows studies based on XMCD [2], [3], presented in subsection 1.2.3, which describes the different response of a magnetized sample to left and right-handed elliptically polarized light. Likewise, studies of MO effects using linearly polarized harmonics were performed, including the T-MOKE [4]–[6] and magnetic SAS [7] techniques, both described in subsection 1.2.2 and 1.2.4, respectively. While the T-MOKE is executed in a reflection geometry retrieving information only about the material's surface phenomena, the magnetic SAS drawback, in a transmission geometry, lies on the difficulty of producing magnetic domains in the majority of the materials.

Our approach is here based on the resonant Faraday effect using simply generated linearly polarized harmonics on the EUV region. Particularly, the M-edge of transition

metals, our region of interest between 40 and 70 eV. The transmission geometry allows to probe all the layers of the material and no magnetic domains are required.

3.2 Static Faraday effect

As detailed in Chapter 1, the Faraday effect relies on the change of light's polarization after its interaction with the material. More specifically, this effect leads to the rotation of the polarization axis (θ_F) of the incident linearly polarized light upon transmission through a magnetized sample and it changes its polarization to elliptical (ε_F). The Faraday rotation and ellipticity are related with $\Delta\delta$ and $\Delta\beta$ from equation 1.1, which in turn are proportional to the magnetization.

3.2.1 Theoretical relation between Faraday quantities and magnetization

Figure 3.1 schematically represents the polarization of the transmitted light through a magnetized sample. The Faraday effect induces on the incident linearly polarized beam a rotation of its polarization axis and an ellipticity degree. In our configuration, the magnetization and the incident light are normal to the material's surface. The Faraday effect measurement is then performed for the two symmetric magnetization directions (M^+ and M^-), perpendicular to the sample's surface. Here the $\pm$ refer to the two symmetric magnetization direction of the sample while in section 1.2 $\pm$ stands for

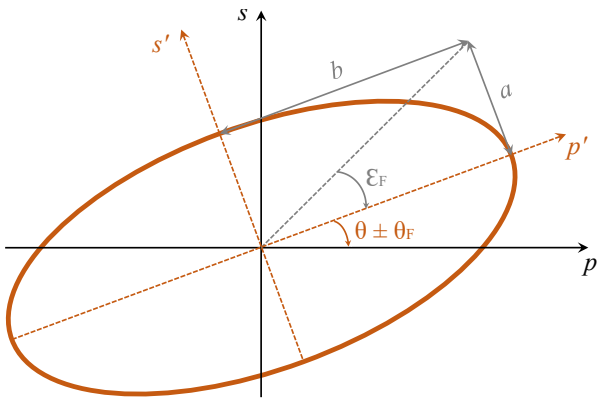

FIGURE 3.1: **Representation of the transmitted light polarization.** The Faraday effect leads to a transmitted beam elliptically polarized ε_F introducing a rotation of the polarization axis by θ_F. The ellipse minor and major axes, a and b, define the ellipticity such as, $\tan\varepsilon_F = a/b$. The s' and p' axes correspond to the rotation of the transmitted light relative to the s and p axes of the incident light.

left- and right-circular of the photon helicity relatively to the wave vector of the light. The electric field for $\vec{M}^+$ and $\vec{M}^-$ is described by the ellipse parameters major (a) and minor (b) axis of the polarization, which can be simply written according to

$$\vec{E}_\pm = b\vec{e'}_p \pm ia\vec{e'}_s \tag{3.1}$$

To evaluate the effect of the analyzer on the beam, this equation has to be rewritten using the s and p base,

$$\begin{aligned} \vec{e'}_p &= \cos(\theta \pm \theta_F)\vec{e_p} + \sin(\theta \pm \theta_F)\vec{e_s} \\ \vec{e'}_s &= -\sin(\theta \pm \theta_F)\vec{e_p} + \cos(\theta \pm \theta_F)\vec{e_s} \end{aligned} \tag{3.2}$$

where θ is the initial angle between the polarization axis and the p direction (before the sample) and θ_F is the Faraday rotation. Then one can write the equation 3.1 as following,

$$\vec{E}_\pm = [b\cos(\theta \pm \theta_F) \mp ia\sin(\theta \pm \theta_F)]\vec{e_p} + [b\sin(\theta \pm \theta_F) \pm ia\cos(\theta \pm \theta_F)]\vec{e_s} \tag{3.3}$$

After the analyzer and considering $\tan\varepsilon_F = a/b$, the electric field becomes:

$$\vec{E}_\pm = E_p^\pm \vec{e}_p + E_s^\pm \vec{e}_s \tag{3.4}$$

where

$$\begin{aligned} E_p^\pm &= bt_p[\cos(\theta \pm \theta_F) \mp i\tan(\varepsilon_F)\sin(\theta \pm \theta_F)] \\ E_s^\pm &= bt_s[\sin(\theta \pm \theta_F) \pm i\tan(\varepsilon_F)\cos(\theta \pm \theta_F)] \end{aligned} \tag{3.5}$$

and t_p and t_s are the transmission coefficients for respectively p and s direction of the light.

The total intensity of the transmitted light is equal to:

$$I^\pm = I_p^\pm + I_s^\pm = \mid E_p^\pm \mid^2 + \mid E_s^\pm \mid^2 . \tag{3.6}$$

From equation 3.5, the p and s components of the intensity, $I_p^{\pm}$ and $I_s^{\pm}$ respectively, can be written as follows:

$$\begin{aligned} I_p^{\pm} &= b^2 T_p[\cos^2(\theta \pm \theta_F) + \tan^2(\varepsilon_F)\sin^2(\theta \pm \theta_F)] \\ I_s^{\pm} &= b^2 T_s[\sin^2(\theta \pm \theta_F) + \tan^2(\varepsilon_F)\cos^2(\theta \pm \theta_F)] \end{aligned} \tag{3.7}$$

where $T_p = \mid t_p \mid^2$ and $T_s = \mid t_s \mid^2$. Since $(\theta \pm \theta_F) \ll 1$ and $\varepsilon_F \ll 1$ [20],

$$\begin{aligned} I_p^{\pm} &= b^2 T_p[1 - (\theta \pm \theta_F)^2 + \varepsilon_F^2(\theta \pm \theta_F)^2] \sim b^2 T_p \\ I_s^{\pm} &= b^2 T_s[(\theta \pm \theta_F)^2) + \varepsilon_F^2] \end{aligned} \tag{3.8}$$

which gives

$$I^{\pm} = b^2[T_p + T_s(\theta^2 \pm 2\theta\theta_F + \theta_F^2 + \varepsilon_F^2)]. \tag{3.9}$$

To prove the veracity of the used approximation, one can consider the highest θ used in this work, equal to 12°. Consequently, $\theta + \theta_F = 24^{\circ}$ which leads to $\sin(0.4189) \approx 0.4068$, in radians. If we consider the difference between the harmonic intensity of the two opposite magnetization directions, we obtain:

$$\mathbf{I}^{+} - \mathbf{I}^{-} = b^2 T_s 4\theta\theta_F \propto \Delta\delta \propto \mathbf{M}. \tag{3.10}$$

Therefore, it is possible to obtain information about the magnetization dynamics directly by measuring the intensity of the transmitted light for the two symmetric magnetization directions and taking into account its difference. The intensity difference is then related to the Faraday rotation angle, which in turn is proportional to the magnetization.

On the other hand, for specific photon energies very close to the M and L absorption edges, the Faraday rotation vanishes ($\theta_F \sim 0$) and the signal is dominated by ε_F [20],

$$I^{+} = I^{-} = b^2[T_p + T_s(\theta^2 + \varepsilon_F^2)]. \tag{3.11}$$

In that case, it becomes impossible to retrieve the magnetization by the previous method. To have information about the magnetization, one have to do an additional measurement for an unmagnetized sample ($M = 0$). The ellipticity is equal to zero and the

difference between the two measurements becomes proportional to M^2 as follows,

$$\mathbf{I}^{\pm}(\mathbf{M}) - \mathbf{I}^{\pm}(\mathbf{M}=\mathbf{0}) = b^2 T_s \varepsilon_F^2 \sim (\Delta\beta)^2 \sim \mathbf{M^2} \tag{3.12}$$

Once again, one can easily retrieve the magnetization dynamics by measuring the time evolution of this difference. The zero magnetization measurement has to be performed only once, as it does not depend on the time delay. In our experiment, the effect is observed in a large range (∼20 eV) and, depending on the energy, both quantities can contribute at the same time for the effect.

3.2.2 Principle of the measurement

In our research, the sample's ferromagnetic state is characterized through the Faraday effect using linearly polarized high order harmonics. As already discussed, its magnetization can be described by the Faraday rotation and ellipticity. Then, the most logical procedure is to directly measure these two quantities, as Valencia *et al.* [20] performed. However, the goal of our experiment is to know the variation of the sample's magnetization and not the exact value of these two Faraday quantities. As already proved above, by experimentally measuring the vertical component of the transmitted signal, we simply evaluate the variation of the two Faraday quantities, directly related with $\Delta\delta$ and $\Delta\beta$ from equation 1.1, which in turn are proportional to the magnetization. The principle of the Faraday effect measurement is generally represented in figure 3.2 for two opposite directions of the sample's magnetization ($\vec{M}^-$ and $\vec{M}^+$). To measure the *s*-projection of the transmitted light, a polarizer is required in order to reflect the *s*-component and block the *p*-component of the light.

First, for this measurement, a polarizing mirror is introduced in the harmonics beam, with an incidence angle close to the Brewster's angle at the targeted energy. For the polarization axis component close to *p*-direction, the *p*-component projection is very weak, meaning the *p*-reflectivity of the mirror (R_p) is very weak. Therefore, we are able to measure mainly the *s*-component. For each harmonic order, we measure the intensity of the *s*-component of the transmitted signal for $\vec{M}^-$ and $\vec{M}^+$. Afterwards, we can calculate the respective asymmetry A, which corresponds to the magnetic contrast

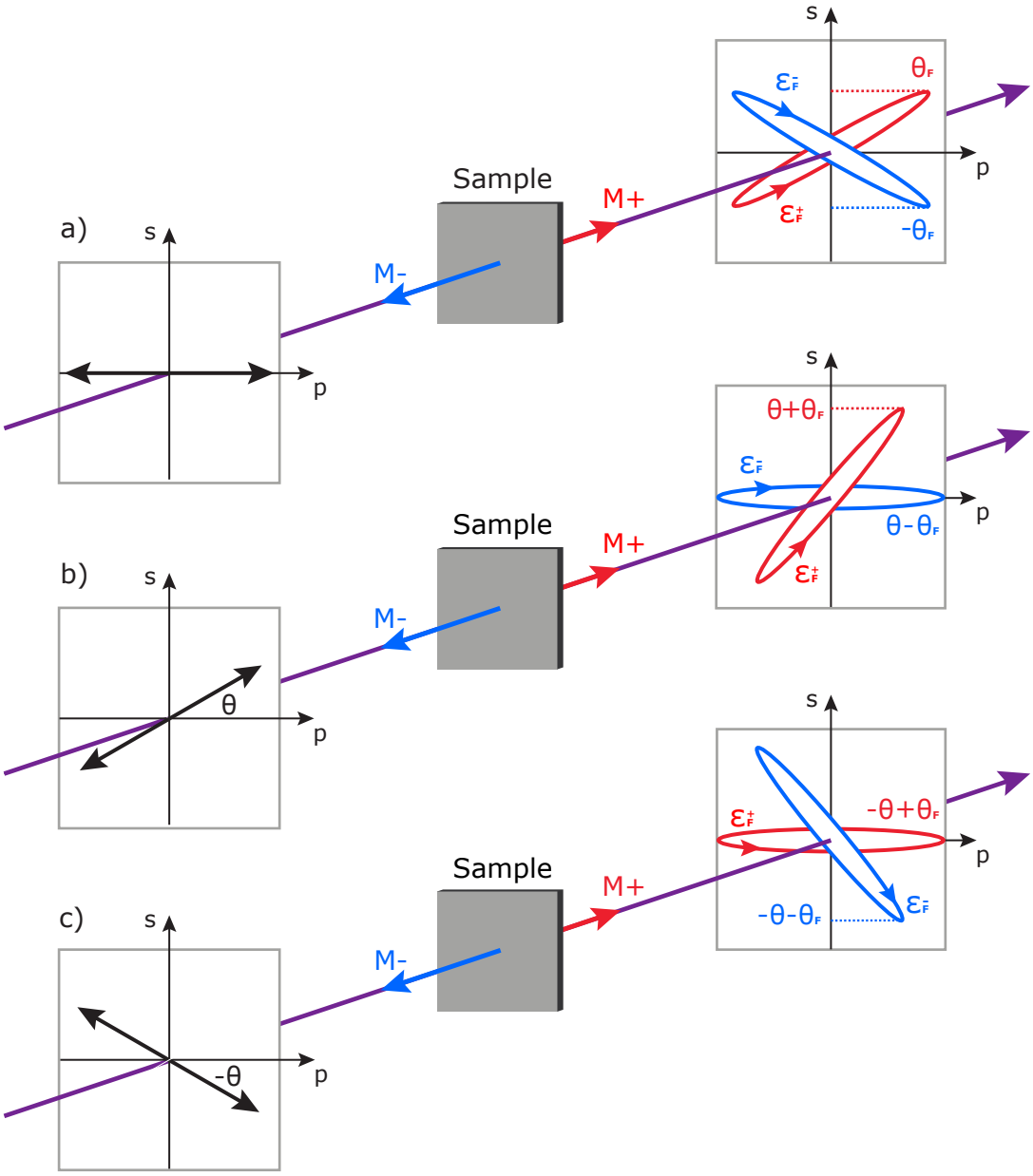

FIGURE 3.2: **Illustration of the Faraday effect.** Faraday rotation angle (θ_F) and ellipticity (ϵ_F) introduced in the incident harmonics' polarization passing through a magnetized sample for two opposite magnetization directions, with the polarization angle of the incident light: (a) parallel to the p direction, (b) equal to θ, (c) and equal to $-\theta$. A half-wave plate was used to rotate the polarization axis of the incident light. To maximize the s projection component: $\theta \approx \theta_F$.

commonly deduced in XMCD experiments,

$$A = \frac{I^+ - I^-}{I^+ + I^-}, \tag{3.13}$$

where I^+ and I^- correspond to the intensity of the s projections of the ellipse for $\vec{M}^+$ and $\vec{M}^-$, respectively. This quantifies the ability to measure the rotation of the ellipse

and the variation of ellipticity through this configuration for the static experiment. Yet, at the Brewster's angle, R_s becomes also weak, strongly limiting the photon flux on our detector. One should then use proper optics for the polarizer to have simultaneously an acceptable R_s and large R_s/R_p.

Second, if the polarization axis of the incident beam is parallel to the p-direction, the vertical projections of the ellipse have the same amplitude so we cannot quantify the effect since $A \approx 0$ (figure 3.2 a). Using a half wave-plate, the angle of the polarization axis of the incident light is set to θ corresponding to the minimum s-component for one of the magnetization directions ($\vec{M}^+$ referring to the red ellipse in figure 3.2 b). Ideally, to maximize the s projection component: $\theta \approx \theta_F$. Rotating the magnets system on 180° ($\vec{M}^-$ corresponding to the blue ellipse in the same figure), a rotation of the polarization axis occurs, introducing a significant vertical component. Therefore, the reflectivity of the signal on the polarizer increases, allowing the measurement of the vertical component projection of the blue ellipse. Then, the asymmetry between these two vertical components is calculated. In addition, for symmetric angles of the polarization axis of the incident light the effect is expected to be symmetric, meaning opposite variation of A (figure 3.2 c).

For time-resolved experiments, the intensity difference ($I^+ - I^-$) is taken into account instead of the asymmetry. The asymmetry is not proportional to the magnetization as one can conclude by the derived equations in the previous subsection.

3.2.3 Sample details

Our Faraday effect based experiment requires the sample in a transmission configuration. Therefore, the material of the sample must be easy to magnetize, thus with a square magnetic hysteresis loop. Cobalt is an appropriate material, fulfilling these requirements of the experimental configuration. Cobalt based magnetic samples with different thicknesses of cobalt were used in the experiment. An alloy of CoDy, $Pt(5nm)/\mathbf{Co}_{76}\mathbf{Dy}_{24}(50nm)/Pt(5nm)/Ta(3nm)$ deposited on a 100 nm Si_3N_4 membrane, where the Dy ensures the out-of-plane magnetization of Co, and two Co/Pt multilayers, $Al(5nm)/Pt(2nm)/[\mathbf{Co}(0.6nm)/\mathbf{Pt}(0.8nm)] \times 20/Al(5nm)$ deposited on a 50 nm Si_3N_4 membrane and $Ta(5nm)/Pt(5nm)/[\mathbf{Co}(1.5nm)/\mathbf{Pt}(1.2nm)] \times 5/Pt(3nm)$ deposited on a 50 nm Si_3N_4 membrane. Each sample is composed of several membranes with different sizes as schematically represented in figure 3.3 b).

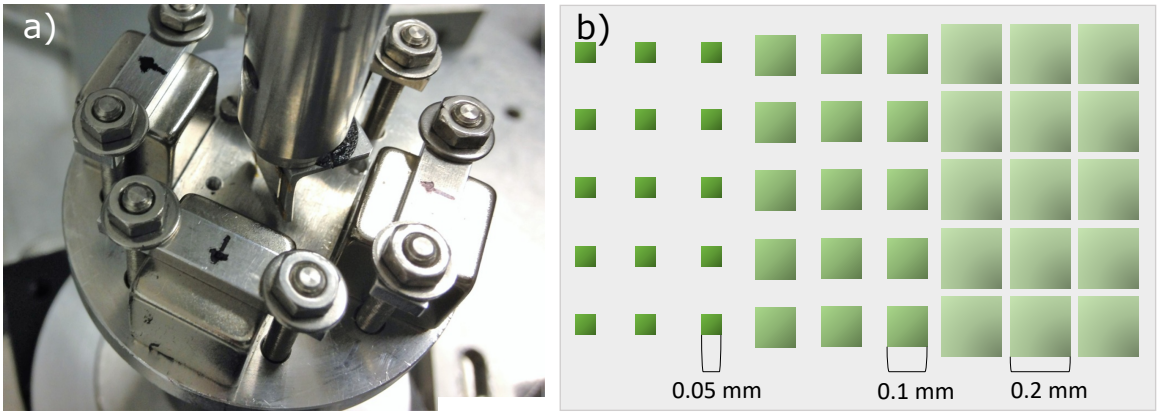

FIGURE 3.3: **Sample details.** (a) Photography of the four permanent magnets support and the respective sample holder. (b) Scheme of the sample, constituted of membranes with different sizes (0.05, 0.1 and 0.2 mm^2).

The sample is fixed and surrounded by four permanent magnets to stabilize a single domain state with out-of-plane magnetization (figure 3.3 a). A magnetic field of 200 mT is used in the experiment and it is sufficient to fully saturate the magnetization of the samples. The magnet structure can be rotated around the sample in order to inverse the induced magnetization. This configuration ensures exactly the same magnitude of the magnetization projection on the optical axis for negative and positive fields, as schematically shown in the sample position of figure 3.2 (blue and red arrows, respectively).

3.2.4 Experimental apparatus

Here, I describe two different experimental configurations for the measurement of the static Faraday effect. Yet, the principle of the measurement is the same for the two configurations since both need the polarizer combined with the half-wave plate to measure the *s*-component of the transmitted light. The two configurations differ on the measurement method. The first one, measures the effect through the **(1) harmonics footprint**, and the second one through the **(2) harmonics spectra**.

To successfully measure the Faraday effect, we started from a simple experimental setup, looking at the (1) footprint of the harmonics as schematically represented in figure 3.4 a). In this configuration, the measured signal corresponds to a mixture of all the generated harmonics. The important losses degree on the optics significantly reduces the number of available photons for the Faraday effect measurement. Therefore, the signal variation between the two magnetization directions of the sample is expected

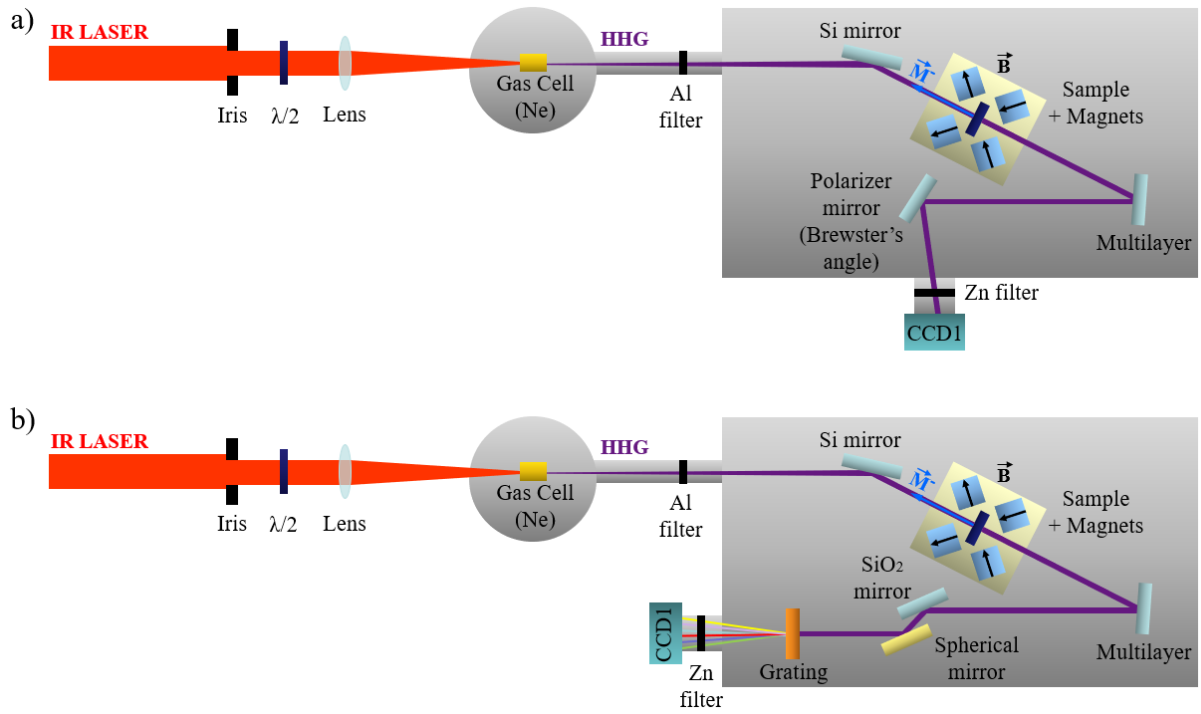

FIGURE 3.4: **Schematic diagrams of the experimental setup for the measurement of the Faraday effect through the harmonics footprint.** The harmonics are focused on the magnetic sample in order to measure the static Faraday effect. The Al and Zn filters prevents the IR light arriving to the sample and saturating the CCD camera. Two configurations are represented: a) harmonics footprint and b) harmonics spectra configurations.

to be difficult to measure. Nevertheless, the signal variation was successfully detected (see subsection 3.2.5.2). This configuration was then slightly modified to have information about the generated harmonics spectra (figure 3.4 b) to assure the generation and selection of the harmonics region of interest, which is around 60 eV for the Cobalt $M_{2,3}$ edge.

Following the schematic representation on figure 3.4 a), the linearly polarized laser is focused into a gas cell filled with neon generating high order harmonics horizontally polarized in a wide photon energy range. By adjusting the source parameters, such as the iris aperture, the laser chirp and the gas pressure, it is possible to optimize the generation efficiency close to the targeted spectral range for magnetic edges studies. The majority of the IR light is blocked by a 300-nm-thick Al foil transmitting ~50% of the EUV light up to the Al L_3 edge at 72.5 eV. The Si mirror is used to re-position the beam in the axis of the magnetized sample. At the same time, the Si mirror suppresses a significant part of the IR beam due to the grazing incidence angle of the beam. The sample is surrounded by four permanent magnets to stabilize a single domain state with

out-of-plane magnetization. After passing through the sample, the harmonics around 60 eV are selected and reflected by the multilayer into a SiO_2 polarizer mirror, placed close to its Brewster's angle at the referred energy. This polarizer provides a high ratio between the reflectivities of the *s* and *p*-components ($R_s/R_p \sim 10$). Combined with a half-wave plate, the SiO_2 polarizer reflects mostly the *s*-component of the harmonics into the CCD camera for generally 30s (figure 2.15), after passing through a Zn filter. This filter removes the lower harmonic orders, and combined with the Al filter, selects the harmonics of interest for the experiment (around 60 eV). In addition to the relatively low harmonics intensity, the greatest difficulty for the measurement of the Faraday effect lies on the signal losses in the optics, especially the polarizing mirror. Close to its Brewster's angle at the targeted energy, R_s/R_p is preferably high in order to reflect mostly the *s*-component. Yet, the reflectivity of the *s*-component is very low using the SiO_2 polarizer mirror. For the spectral measurements in figure 3.4 b), the modifications in the footprint setup comes after the multilayer. The SiO_2 mirror is now only used to redirect the beam on the right axis by reflecting it into the spherical mirror. This last optical element refocus the harmonics into the CCD camera after passing through a grating, which separates all the harmonic orders.

The footprint setup had shown the capability of this configuration to measure the Faraday effect. But the harmonics spectra gives a more precise and detailed information on the effect since each energy corresponds to different information. If the harmonics are mixed as happens in the footprint configuration, this detailed information becomes indistinguishable. Then the second experimental setup configuration corresponds to the measurement of the Faraday effect through the (2) harmonics spectra, which is represented in figure 3.5. A half-wave plate was used to vary the polarization angle of the incident harmonics, a key element of the Faraday effect observation. For each polarization angle we measure the *s*-component of the harmonics intensity for two opposite magnetization directions of the sample giving rise to the evaluation of the static Faraday effect. After the generation of the harmonics in the gas cell, the SiO_2 mirrors at grazing incidence combined with the half-wave plate remove the driving IR light, horizontally polarized. The remained one is then blocked by two 300-nm-thick Al foils. The toroidal mirror (f=1.5m) focuses the harmonics in the magnetized sample surrounded by four permanent magnets. Afterwards, the harmonics are reflected by a polarization analyzer into a spectrometer, where each harmonic order is well separated by a concave

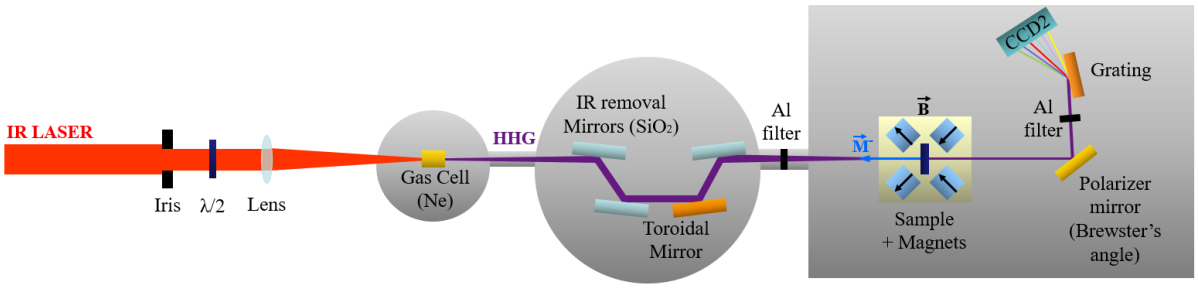

FIGURE 3.5: **Schematic diagrams of the experimental setup for the measurement of the Faraday effect through the harmonics spectra.** The half-wave plate is used to vary the polarization angle of the incident harmonics beam. For each polarization angle, the *s*-component of the harmonics intensity for two opposite magnetization directions of the sample is measured.

grating (1000 lines mm^{-1}), being then recorded with the CCD camera. The characteristics of this CCD camera are similar to the one used in the previous setup configuration but it can be placed inside the vacuum chamber. In this configuration, a gold coated mirror and a multilayer mirror optimized at 60 eV were used as a polarizer for CoDy and Co/Pt samples, respectively. For the CoDy sample, the gold mirror is used at 40.0º. In this particular case, $R_s = 0.04$ and the theoretically expected ratio between the *s* and *p* reflectivities is ~ 17. For the Co/Pt sample, the multilayer mirror, used due to the less quantity of cobalt present in the sample, is set at 42.1º. $R_s = 0.18$ and the respective ratio between the *s* and *p* reflectivities is ~ 900. This allows a proper measurement of the vertical projection component of the two ellipses. With regard to the polarization axis angle of the incident beam θ, introduced in subsection 3.2.2, its value, which maximizes the visibility of the Faraday effect, was experimentally obtained for the two types of samples. For CoDy the effect is maximized with $\theta = \pm 12°$ and for Co/Pt $\theta = \pm 6°$.

3.2.5 Experimental results

3.2.5.1 CoDy sample absorption

The absorption of the CoDy sample around the spectral energy range of interest was evaluated. Figure 3.6 a) represents the spectro/spatial distribution of the high order harmonics recorded by the CCD camera for $\vec{M}^-$ direction. Figure 3.6 b) shows the projection of the intensity of two harmonics spectra recorded for two positions of the CoDy sample, in and out of the harmonics path (orange and black lines, respectively). With the sample in the harmonics path, the transmission efficiency of the harmonics

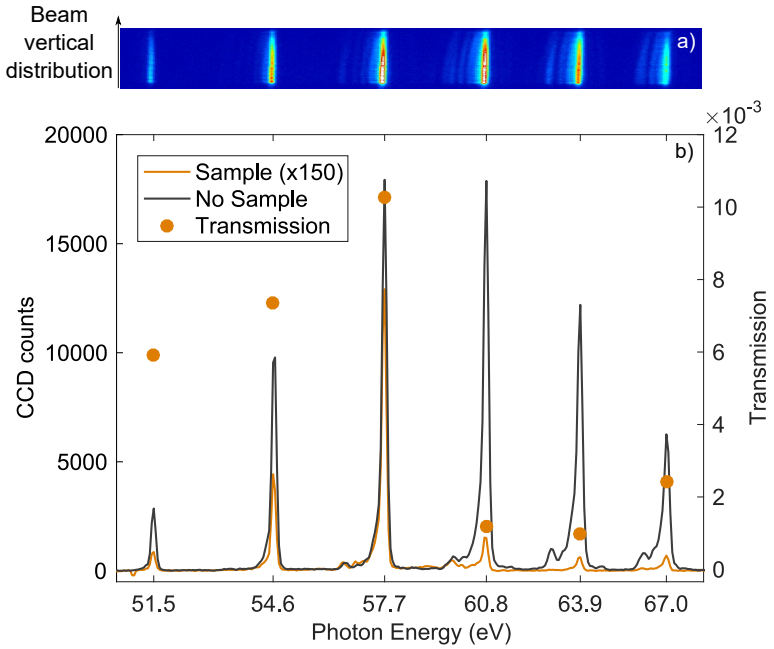

FIGURE 3.6: **Transmission of the CoDy sample.** (a) Harmonics spectrum: vertical distribution of the beam as function of the photon energy (30s acquisition time). (b) Energy projection of the harmonics spectra showing the intensity of each harmonic for two configurations, with and without the sample in the harmonics path (30s and 2s acquisition time, respectively).

around the $M_{2,3}$ absorption edge of cobalt is calculated. As expected, there is a strong absorption of the signal around this edge. The transmission decays from 10×10^{-3} at 57.7 eV to 1.5×10^{-3} at 60.8 eV. The signal losses on the sample added to the losses in the harmonics path (optics - 0.7, filters - 0.25, and polarizer - 10^{-4}) constitute an important loss factor of 10^{-8}. Therefore, the low number of available photons to detect the Faraday effect makes this experience a great challenge.

3.2.5.2 Measurement of the Faraday effect through the harmonics footprint

As referred in the previous subsection, in the first configuration measurement, the effect was observed through the footprint of the harmonics. A spectral information is then necessary to understand which harmonics contribute for the effect. The spectral measurements show the generated harmonics without (figure 3.7 a)) and with (figure 3.7 b)) the CoDy sample on the harmonics path. Figure 3.7 c) represents the energy projection of these two harmonics spectra showing the intensity of each harmonic. Without the sample in the path, 13 harmonics are identified, from $\sim$ 25 to 62 eV. This spectrum

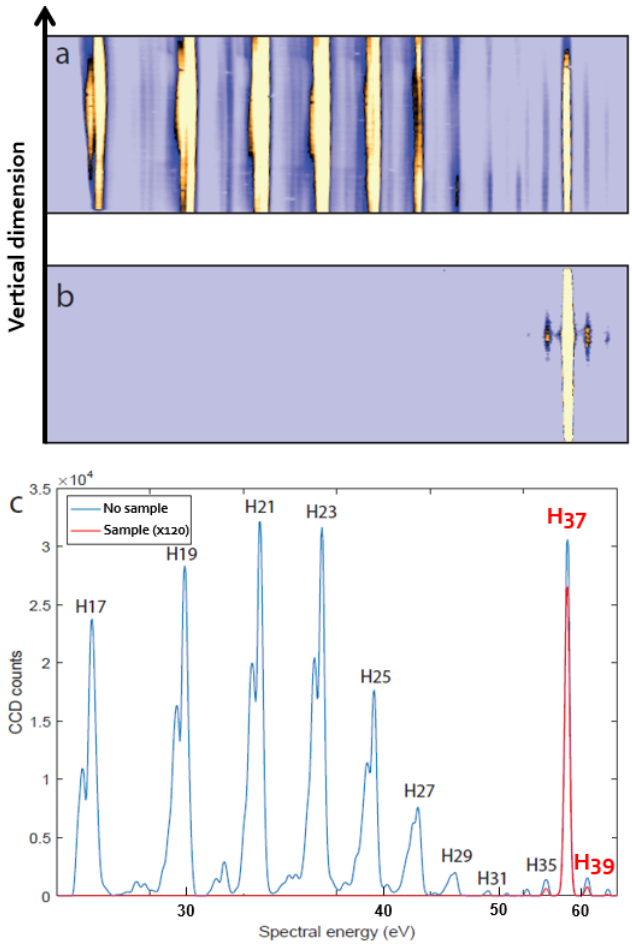

FIGURE 3.7: **Harmonics spectra in the harmonics footprint configuration.** Harmonics spectrum: vertical distribution of the beam as function of the photon energy without (a) and with (b) the sample in the harmonics path (1s and 30s acquisition time). (c) Energy projection of the harmonics spectra showing the intensity of each harmonic for two configurations, with and without the sample in the harmonics path (30s and 2s acquisition time, respectively).

shows a double peak for each harmonic, which is a frequent observation in the harmonics spectra, probably corresponding to spectral interferences. When the sample is in the harmonics path, essentially one energy is selected close to 60 eV, corresponding to a transmission of 10^{-3}. One can confirm the efficiency of the multilayer selecting the energy range that corresponds to the cobalt $M_{2,3}$ edge with rather good transmission.

The results describing the Faraday effect are presented in figure 3.8 for a CoDy sample. The first image (figure 3.8 a) corresponds to the direct profile of the harmonics in the CCD camera, without the sample in the harmonics path. The round shape is due to the Al filter. Figure 3.8 b) corresponds to the HHG signal with the sample in the path. Since the signal is rather weak after the sample, a binning was applied to obtain the

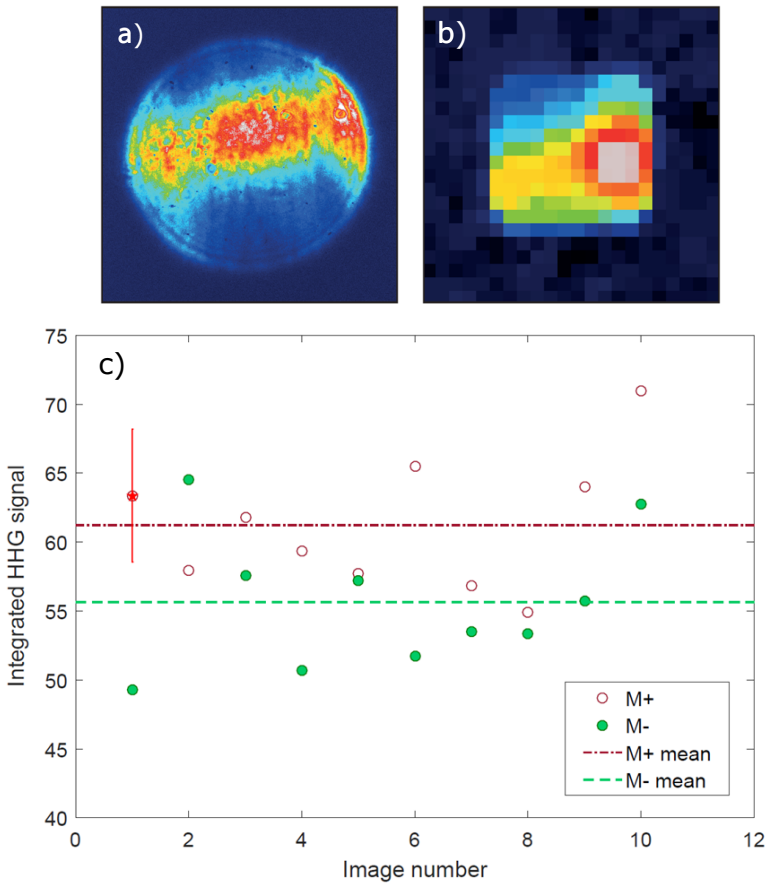

FIGURE 3.8: **Faraday effect measurement from the harmonics footprint.** a) HHG spatial distribution (1s acquisition time). b) HHG spatial distribution with the sample in the harmonics path (30s acquisition time). c) Integrated HHG signal for consecutive alternated magnetic field directions.

image. The measurement in figure 3.8 c) corresponds then to the integrated HHG signal with the sample in the path for consecutive alternated magnetic field directions. In general, the signal increases when the magnetization is in the $\vec{M}^+$ direction (red circles). The signal difference between the two magnetization directions ($\vec{M}^-$ and $\vec{M}^+$) is only 10 %, which corresponds to the detectable Faraday effect. These first results prove the possibility of measuring the resonant magneto-optical Faraday effect with linearly polarized harmonics. To obtain further information about a greater number of harmonics contributing to the effect, a spectral measurement is preferable. This leads to the second configuration of the setup whose experimental results are presented below.

3.2.5.3 Measurement of the Faraday effect through the harmonics spectra

The second setup configuration for the measurement of the static Faraday effect uses then the harmonics spectra, whose principle of the measurement corresponds to the

one described in subsection 3.2.2. The experiment was performed using two different cobalt-based samples. First, I present the results for the same CoDy sample used in the harmonics footprint setup configuration, and then the results for the Co/Pt multilayer.

3.2.5.3.1 CoDy alloy

Figure 3.9 a) shows the projection of the energy of the harmonics spectra for the two opposite magnetization directions ($\vec{M}^-$ in blue and $\vec{M}^+$ in red), where eight harmonics are identified. The curves correspond to an average of the harmonics spectra recorded for each magnetization direction. The polarizing gold coated mirror reflects a large

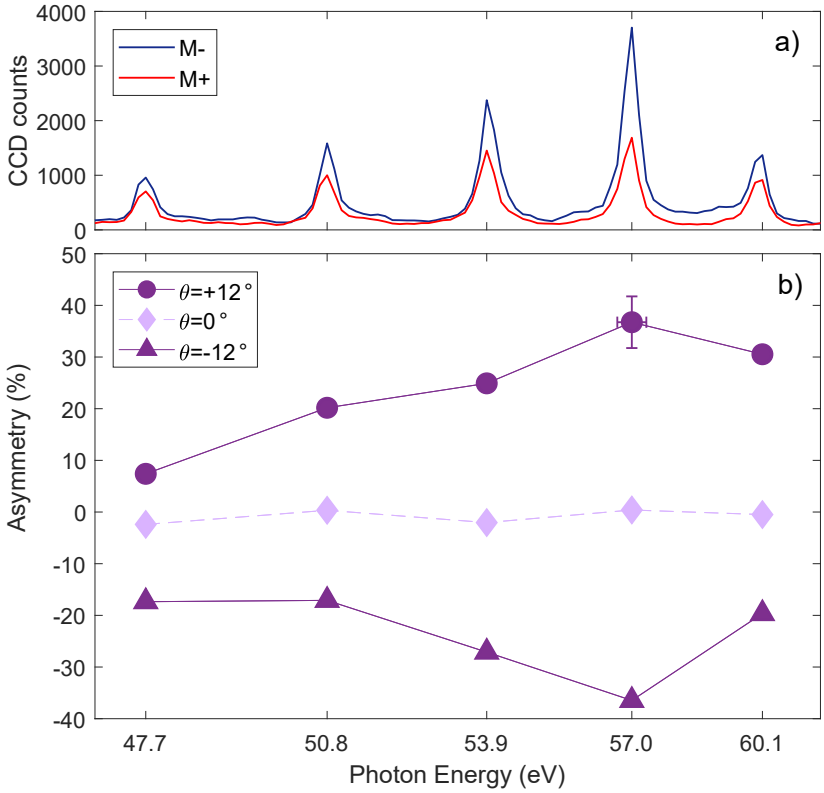

FIGURE 3.9: **Static Faraday effect of CoDy sample as a function of photon energy.** (a) Average of the energy projection of the recorded harmonics spectra (30s acquisition time) showing the intensity of each harmonic for two opposite directions of the sample's magnetization ($\vec{M}^-$ in blue and $\vec{M}^+$ in red lines). (b) Asymmetry of the Faraday effect measured for three different polarization axis angles of the incident light (θ, $-\theta$ and 0) for CoDy (see equation 3.13).

range of harmonics around the energy of the cobalt M-edge, giving origin to this spectra pattern. We observe a different response in the signal intensity of the harmonics for the two magnetization directions. A considerable decrease of the harmonics signal is observed from the $\vec{M}^-$ to the $\vec{M}^+$ directions, describing the decrease of the *s*-component

transmission of the harmonics (vertical projection of the ellipse illustrated in figure 3.2). It is clear in several harmonics and it is more remarkable in the ones whose energies are between 54 and 60 eV. This behavior is characteristic of the Faraday effect close to resonance in the EUV range. The two contributions, the difference in phase and the difference in absorption of the two circularly polarized light components traversing the sample ($\Delta\delta$ and $\Delta\beta$ from equation 1.1, respectively) are notable on a large energy range. These observations are supported by Valencia's results [20], represented in figure 3.10. Analyzing the figure, one can infer that the effect at 60 eV, for example, is dominated by $\Delta\beta$, while the main contribution at 57 eV is $\Delta\delta$. On other energies (54 eV, for example) the effect is the result of both factors.

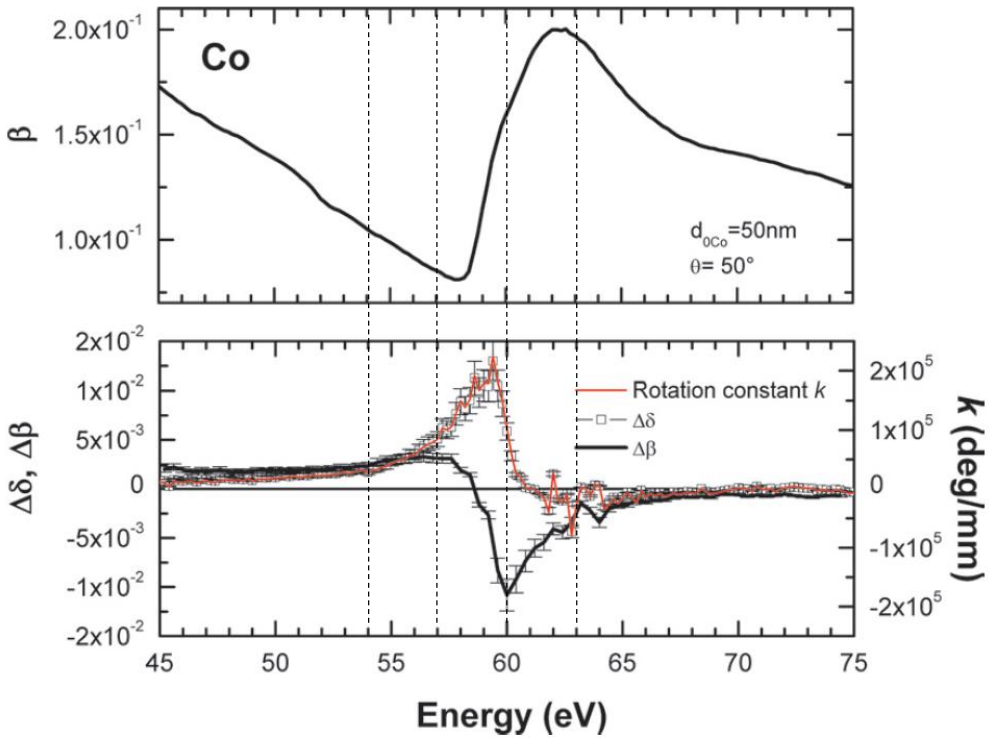

FIGURE 3.10: **Absorption and MO constants of Co as function of photon energy at the Co 3p edges (from [20]).** The figure on the top shows the measured absorption constant β. On the bottom, the spectra of the MO constants $\Delta\delta$, $\Delta\beta$ and Faraday rotation constant k are shown.

To quantify the static Faraday effect in each harmonic, the asymmetry between the two signals ($\vec{M}^-$ and $\vec{M}^+$) is calculated from figure 3.9 a), according to equation 3.13. Figure 3.9 b) shows the respective result for the 3 positions of the half wave-plate, corresponding to 3 polarization axis angles of the incident light (θ, $-\theta$ and 0). When setting the incident polarization parallel to the analyzer plane ($\theta = 0°$, as represented in figure 3.2 a) the projections have the same amplitude, giving $A \approx 0$, as expected.

When turning the incident polarization axis such that the *s*-projection in one of the two magnetization directions is minimal ($\theta = \pm 12°$, as represented in figure 3.2 b) and c) corresponding to the red and blue ellipse, respectively), A is maximum and opposite for symmetric θ. Close to the Co M-edge, for which the analyzer angle has been optimized, A reaches almost 40% for the two symmetric polarization axis angles, showing its theoretical symmetry property. This fully demonstrates our ability to measure the Faraday effect. The obtained asymmetry is much higher than the achieved results in XMCD techniques. For example, Willems *et al.* [3] observed $A \approx 6$ % at the Co edge at 60.8 eV. Moreover, the effect covers a large range of photon energies due to the two contributions for the effect, the difference in absorption ($\Delta\beta$) and the difference in phase ($\Delta\delta$), which is a big plus for ultrafast time resolved experiments.

3.2.5.3.2 Co/Pt multilayer

The experiment was then accomplished with a Co/Pt multilayer, where the cobalt thickness is only 12 nm contrasting with 42 nm in the CoDy alloy. We intend to prove here the high sensitivity of our technique regarding the limited thickness of the cobalt. To overcome the small thickness of cobalt we have used a multilayer as a polarizer, whose R_s/R_p is higher than the Au polarizer, optimized close to 60 eV. The static results

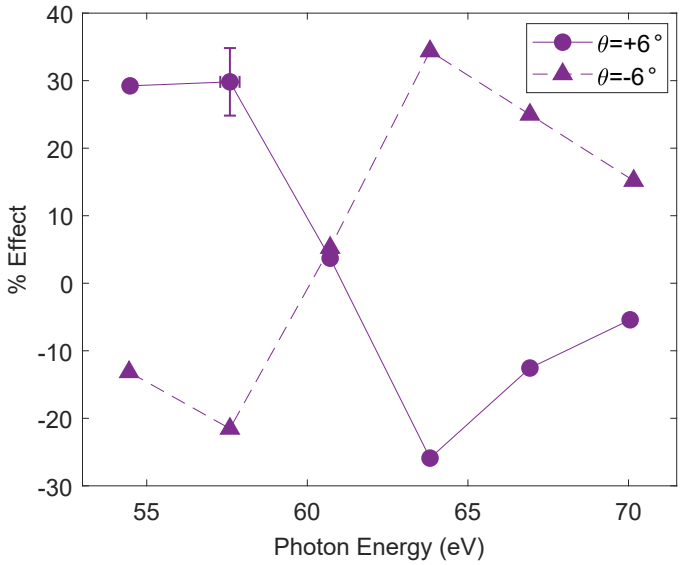

FIGURE 3.11: **Static Faraday effect of Co/Pt multilayer as a function of photon energy.** Asymmetry of the Faraday effect measured for symmetric positions of the half wave-plate for the [Co(0.6 nm)/Pt(0.8 nm)]x20 multilayer (see equation 3.13).

of the Faraday effect for the Co/Pt multilayer is represented in figure 3.11 for symmetric polarization axis of the incident light ($\theta = \pm 6°$). Before and after the cobalt M-edge around 60 eV the effect is opposite, reaching 30 % of asymmetry close to 58 eV and 35 % close to 64 eV, while it is roughly zero around 60 eV. Carefully analyzing Valencia's results represented in figure 3.10, we may consider that an inversion of the effect after 60 eV is possible. Indeed, recent unpublished results from another group clearly show this inversion.

Chirp influence

The HHG signal can be improved by adjusting the source parameters such as the laser chirp. Occasionally, this change gives origin to some extra peaks in the harmonics spectrum for each energy, as we can see in figure 3.12 a). These peaks are probably due to spectral interferences. Indeed it is very interesting since it gives an extra spectral

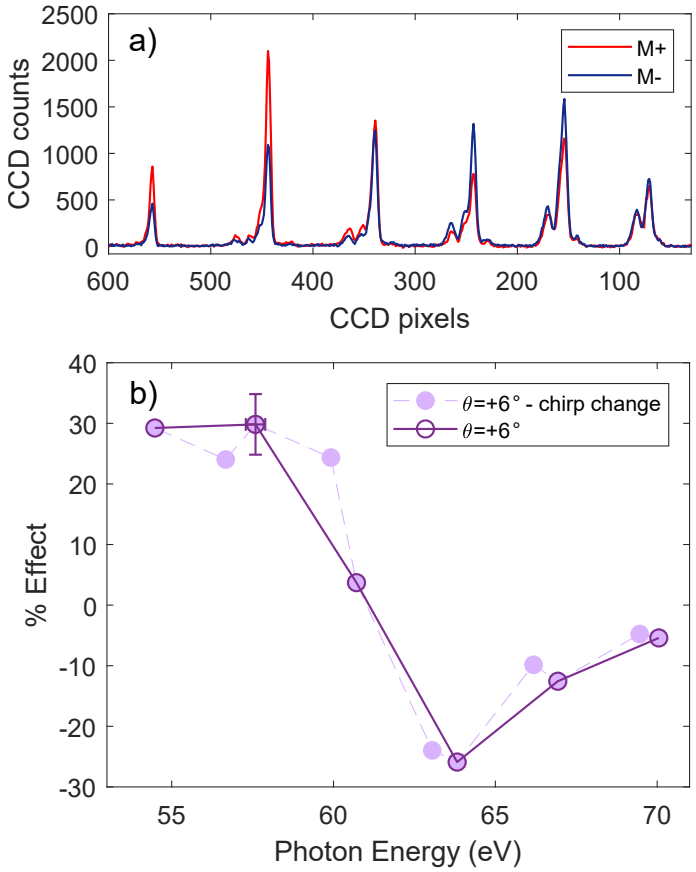

FIGURE 3.12: **Static Faraday effect of Co/Pt multilayer as a function of photon energy.** a) Harmonics spectra for two magnetization directions with the chirp change (30s acquisition time). b) Asymmetry of the Faraday effect measured for symmetric positions of the half wave-plate for [Co(0.6 nm)/Pt(0.8 nm)]x20 multilayer with the chirp results.

information for each harmonic in a single measurement. Figure 3.12 b) shows exactly this. It corresponds to the static Faraday effect measurement of the Co/Pt multilayer presented in figure 3.11 but with the additional spectral information obtained from the slight change of the chirp. In fact, for $\theta = +6^{\circ}$ the inversion of the magnetic asymmetry at 60 eV is more abrupt than the one predicted without taking into account the chirp measurements (light violet curve).

3.3 Ultrafast demagnetization of coupled CoDy and Co/Pt multilayer

3.3.1 Pump-probe setup

Our developed HHG setup revealed strong magnetic asymmetries up to 40 % in the measurement of the static Faraday effect in CoDy and Co/Pt materials. We then exploit these results to study pump-probe induced dynamics, expecting a high degree of the samples' demagnetization. If one had a fast detector, one would be able to follow this dynamics in real time. However, there is no device with such capacity. The pump-probe technique is used to detect this fast time evolution phenomena on the femtosecond time scale. First, a short pump pulse creates an excitation on the sample. Then, a time delayed second pulse resolves the evolution of the excitation created in the sample. This is repeated for several time delays in order to characterize the temporal evolution of the phenomenon of interest. Pump and probe pulses must be shorter than the time scale of the magnetization time evolution, in specific shorter than hundreds of femtoseconds. The time resolution of the laser used in the experiment is about 30 fs and, the high order harmonics are often generated with pulse durations shorter than that of the driving laser, about 5 fs, defining an excellent time resolution for this pump-probe experiment.

Our experimental setup is schematically represented in figure 3.13. Both pump and probe pulses are created by the same laser pulse making the source inherently jitter free. Since the convolution of both pulses duration (IR and HHG) is given by $\sqrt{(30)^2 + (5)^2}$, one can follow the magnetization dynamics of the magnetic materials with a time resolution of about 30 fs.

The HHG branch (probe) was already described in the previous section for the static Faraday effect measurement. Through a 90-10% beam splitter, a small fraction of the

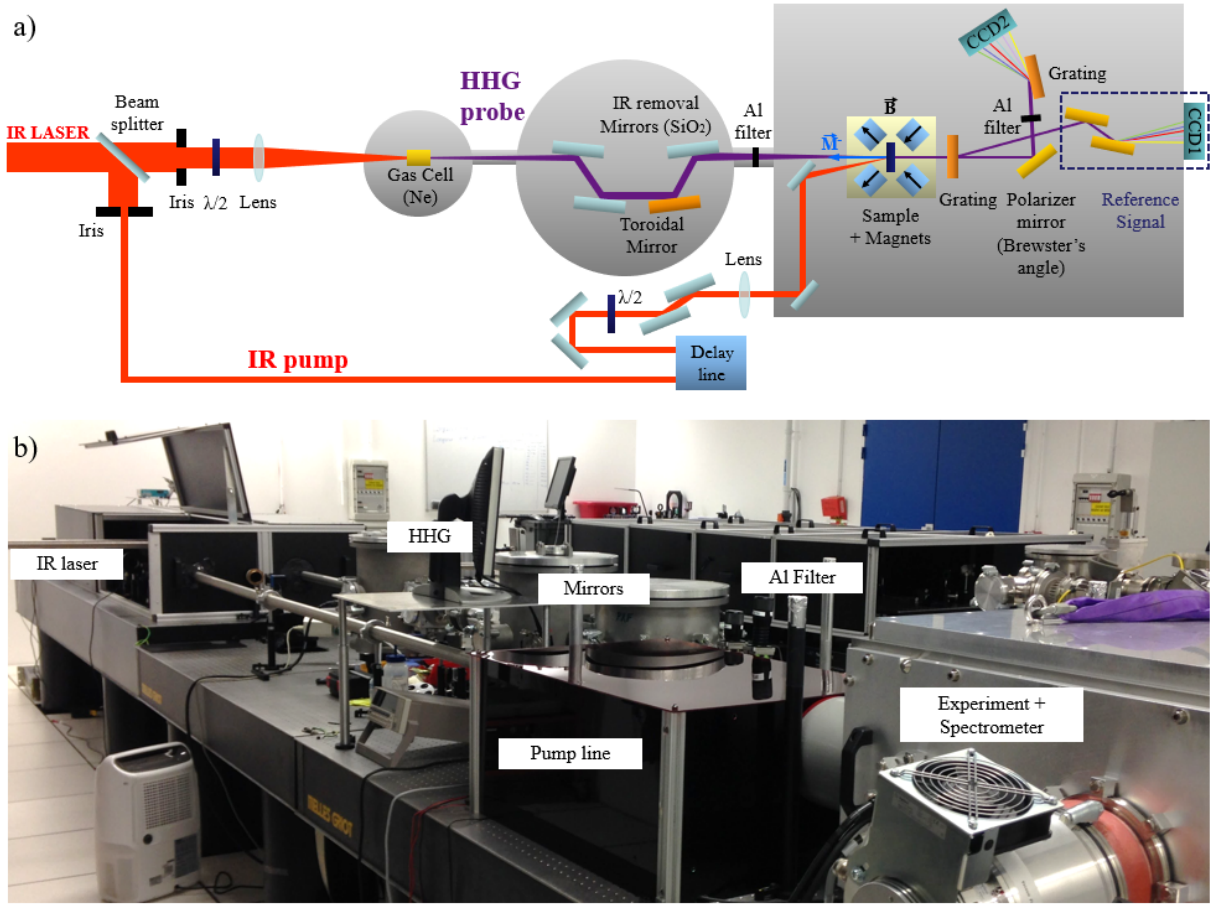

FIGURE 3.13: **Experimental pump-probe setup.** a) Schematic diagram and b) photo of the setup in the *Salle Corail* at *LOA*. The magnetic sample is pumped by an IR laser pulse and probed by a delayed X-ray pulse (linearly polarized harmonics, generated by the same laser in a gas cell filled with neon). Both, pump and probe, are focused at the same point on the sample in order to measure its ultrafast magnetic dynamics through the Faraday effect. A reference signal is simultaneously recorded in another CCD camera using the first order transmission of the signal passing through the grating placed just after the sample.

infrared laser beam driving the HHG process is used as a pump to initiate the demagnetization dynamics. The delay line with a step size of 6 fs allows to acquire information for different time delays. A half-wave plate combined with two SiO_2 mirrors, controls the fluence of the pump beam (from 3 to $\sim$ 5 μJ) and the lens focus the beam to excite the sample. The size of the focal spot (less than 200 μm in diameter) ensures an uniform illumination across one membrane. The other mirrors are used to re-position the beam in the correct axis. In addition, an aluminum filter is used after the polarizer to prevent the IR light of the pump from reaching to the CCD.

3.3.2 Time-resolved results

Time-resolved studies based on the Faraday effect were accomplished for two types of cobalt based samples, alloys and multilayers, with different thicknesses of cobalt.

3.3.2.1 Reference harmonic signal

First time-resolved measurements showed high noise level, which significantly lowers the quality of the acquired data. Due to the difficulty in analyzing this type of data, a reference harmonic signal was implemented in the pump-probe experimental setup. It corresponds to the harmonic signal variation over time, which is simultaneously recorded with the main harmonic signal reflected by the polarizer, using a second CCD camera (the one from the harmonics footprint measurement) allowing the normalization of the main signal. This reference signal is not sensitive to the Faraday effect since it does not pass through the polarizer. In a first moment, a grating was placed before the sample, at the beginning of the application chamber, in order to record the harmonics first order and use it for the normalization of the signal passing through the sample. However, the results were not satisfactory since the harmonics passing through the sample present additional oscillations, which cannot be corrected by the reference signal recorded before the sample. The focal spot size of the HHG beam is bigger than the sample (membrane of 0.05 mm^2) and the possible changes in the signal due to laser pointing oscillations are not included in the reference signal recorded before the sample.

The final configuration used to record the reference signal is represented in figure 3.13 a). The grating was placed immediately after the sample. The harmonics first order (reference signal) is recorded in the CCD1 camera at the end of the vacuum chamber while the harmonics zero order (main signal) continues the usual path until the CCD2 camera. With this configuration, a better spectral resolution of the harmonics was also accomplished, since the reference signal is imaged from a very small membrane. Figure 3.14 shows the reference signal, the main signal and the resulting normalization. The reference signal, acquired in CCD1 for each time delay, was carefully treated by taking the average intensity of individual harmonics subtracted to the background of the same image. The same procedure was done for the main signal, acquired in the CCD2. The normalization results from the division of main and reference signals. We can observe

that the reference signal significantly improves the data quality but it is still sensitive to the polarization variation of the IR laser. A simply way to overcome this limitation is to introduce an IR polarizer in the reference beam path. However, technically, it is difficult to install and the intensity of the beam would be significantly affected.

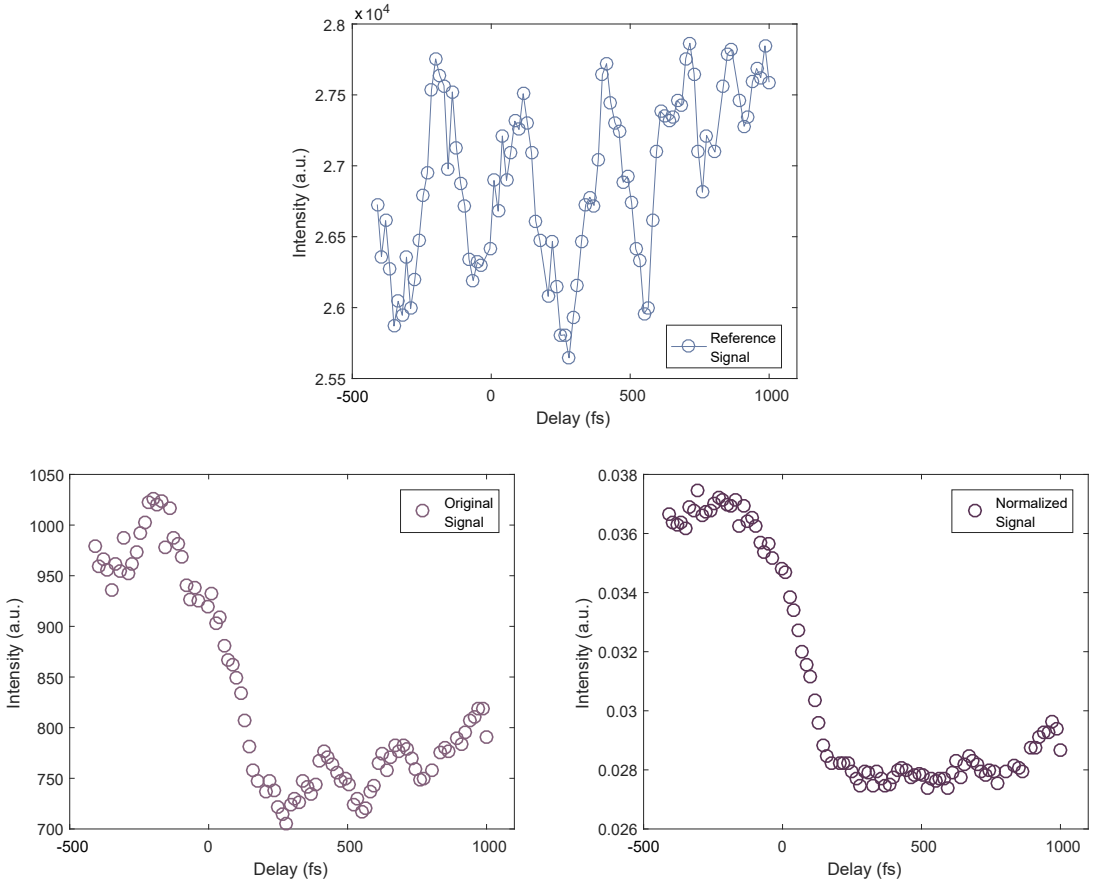

FIGURE 3.14: **Signal intensity as a function of time delay for the Co/Pt multilayer.** Signal intensity as a function of time delay in the [Co(1.5 nm)/Pt(1.2 nm)]x5 multilayer for a) the reference signal, b) the main signal, and c) the original signal normalized by the reference signal.

3.3.2.2 CoDy alloy

The IR pump successfully initiates the demagnetization dynamics and the HHG probes the CoDy alloy at different time delays. Figure 3.15 shows the corresponding signal intensity as a function of time delay. We show here the signal obtained for the 39^{th} harmonic at 57 eV close to the cobalt M-edge. The measured intensity signal is related to the magnetization but not proportional to it. As shown in subsection 3.2.1, for the signal intensity to be directly proportional to the magnetization, we have to consider the difference of the signal intensity for the two opposite magnetization directions. However, for this sample, it was not possible to do the measurement for both

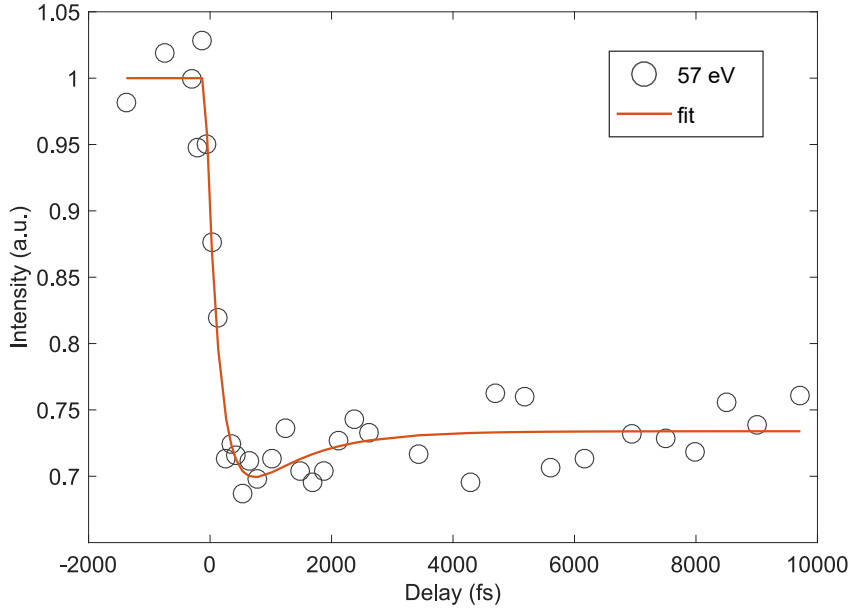

FIGURE 3.15: **Signal intensity as a function of time delay for the CoDy sample.** Demagnetization curve obtained from a 50 nm CoDy sample for a pump fluence of 15 mJ cm^{-2} for a long delay scan at 57 eV. Each point of the curve substitutes the average of 3 neighboring points. The orange solid lines represent the best fits obtained.

magnetization directions due to lack of beamtime. Yet, the acquired data gives a fairly close approximation of the sample's magnetization behavior. The orange solid line represents the best fit calculated by a double exponential expression based on a semi-empirical model [148]. One observe in figure 3.15 that after excitation of the sample, the signal intensity rapidly decreases staying flat up to 10 ps. The displayed slow magnetization recovering time has already been observed in our group for alloys with rare earths, such as CoTb, but not published yet.

As already mentioned, one of the great advantages of the HHG source is the possibility of looking at different energies at the same time, meaning we can observe simultaneously the ultrafast dynamics of our sample at different energies around the edge. In figure 3.16 the curves corresponding to energies from 54 eV to 60 eV are represented for a short time delay. At 54 and 57 eV we can identify a similar behavior of the intensity curves. From the fit we obtain a characterization time of the intensity decrease of about 200 fs. At 57 eV, the signal intensity starts to decrease before the excitation of the sample (0 fs). The average of the data points and shot to shot variations may explain these unexpected and unexplained results. Contrasting with these trends, 60 eV presents a clearly different behavior, clearly visible after 400 fs. Considering that

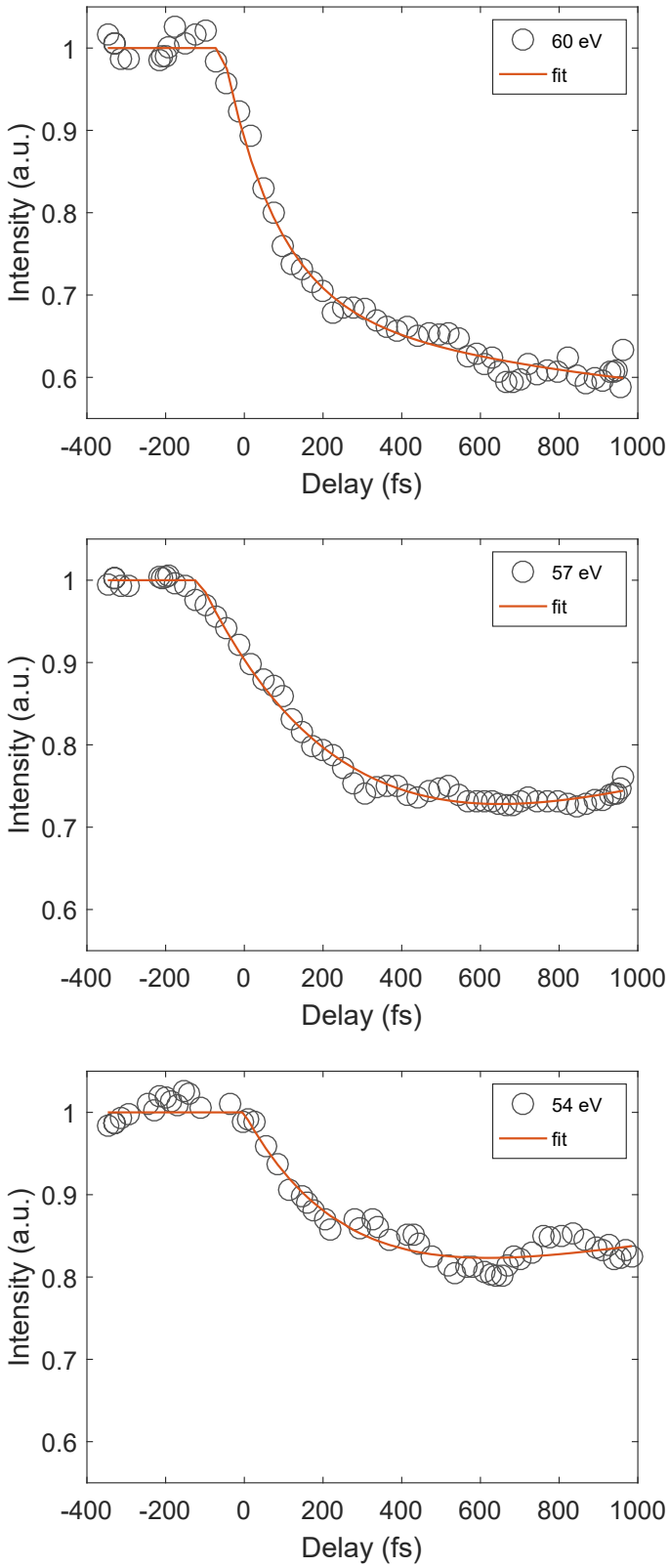

FIGURE 3.16: **Signal intensity as a function of time delay for the CoDy sample at different energies.** In the three curves, each point corresponds to a moving average of 8 neighboring elements.

the Faraday effect mainly results from the absorption of the transmitted light at 60 eV, which is related to the ellipticity, as measured by Valencia *et al.* (figure 3.10), one can thus associate this disparity in the results to the ellipticity contribution. The effect at 54 and 57 eV results, therefore, mainly from the dephasing which results in the Faraday rotation. One can then consider the possibility whether a different behavior in each energy may depend on the dominance of the rotation or the ellipticity. Further investigations may be carried out in order to answer this question, especially time-resolved measurements for opposite magnetization directions of the sample. These first results prove the capability of our method to successfully follow the magnetization dynamics of a ferromagnetic sample, simultaneously probing different energies around the sample's edge. Now the interest relies in the demonstration of the magnetization dynamics in samples with thinner magnetic layers.

3.3.2.3 Co/Pt multilayer

The investigation of the limit of the sample's thickness in our setup is a great challenge. The Co/Pt multilayer that corresponds to the results presented below, contains even less quantity of cobalt than the one used in the static experiment, only 7.5 nm, and 6 nm of platinum. To counter balance the decreased signal amplitude, due to lower thickness of the sample, a multilayer mirror was used as a polarizer optimized around the cobalt M-edge with higher ratio between the *s* and *p* reflectivities and higher reflectivity of the *s*-component. The time-resolved results for the Co/Pt multilayer are represented in figure 3.17, for three different energies close to the Co M-edge. Concerning the 57 and 63 eV curves, the signal evolves oppositely for the two magnetization directions of the sample ($\vec{M}^+$ in red and $\vec{M}^-$ in blue). On the other hand, at 60 eV, the signal exhibits the same behavior for the two opposite magnetization directions. While the same direction of the two curves at 60 eV suggests the Faraday effect measurement mainly due to the ellipticity contribution, the opposite direction of the two curves at 57 and 63 eV indicates an effect dominated by the rotation contribution, as schematically represented in figure 3.17 for each energy. The initial small difference between the $\vec{M}^-$ and $\vec{M}^+$ curves at 60 eV indicates a small rotation contribution for the effect, which can be neglected to simplify the analysis. The same occurs at 57 and 63 eV where a small ellipticity contribution for the effect is neglected for further analysis.

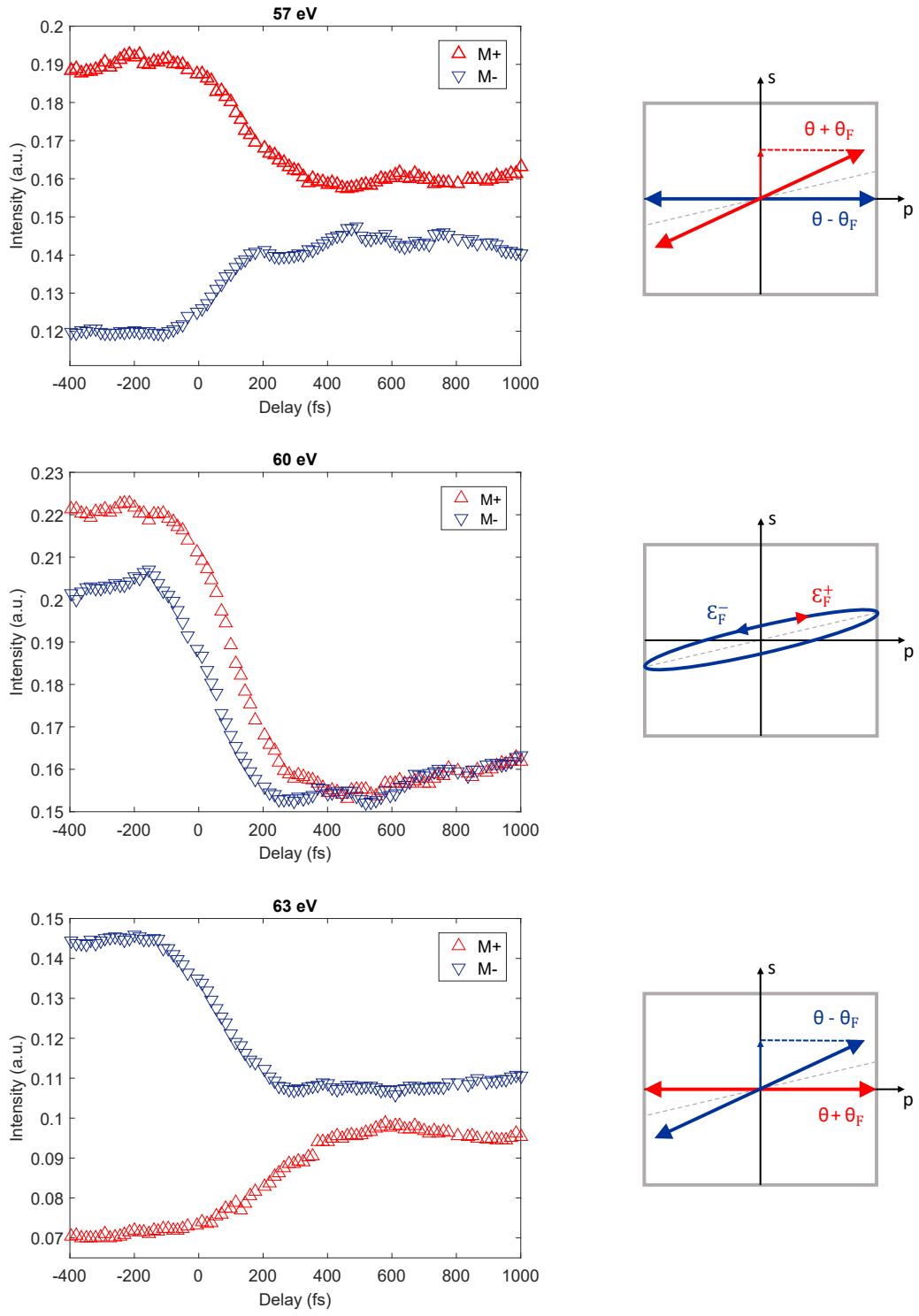

FIGURE 3.17: **Signal intensity as a function of time delay for three different energies in the Co/Pt multilayer.** For each energy, the Faraday effect was measured in the [Co(1.5 nm)/Pt(1.2 nm)]x5 multilayer for two opposite magnetization directions ($\vec{M}^+$ in red and $\vec{M}^-$ in blue). In all the curves, each point corresponds to a moving average of 15 neighboring elements. The Faraday rotation angles θ_F are only representative (in reality, θ_F is much smaller). While at 57 and 63 eV the signal vary oppositely for the two magnetization directions, at 60 eV they have the same behavior.

Due to the characteristic polychromaticity of our source, one is then able to retrieve information about both the ellipticity and the rotation in one single measurement in a large energy range, which are directly related with the magnetization. To have more detailed information about the demagnetization dynamics of the sample one should for example subtract the signal intensity curves corresponding to $\vec{M}^-$ and $\vec{M}^+$ on figure 3.17, as explained in subsection 3.2.1. This is valid for energies where the rotation contribution is the mainly responsible for the effect (57 and 63 eV) and the measurement is directly proportional to the magnetization (equation 3.10). Figure 3.18 shows the magnetization as a function of time delay, derived from the subtraction of the non average

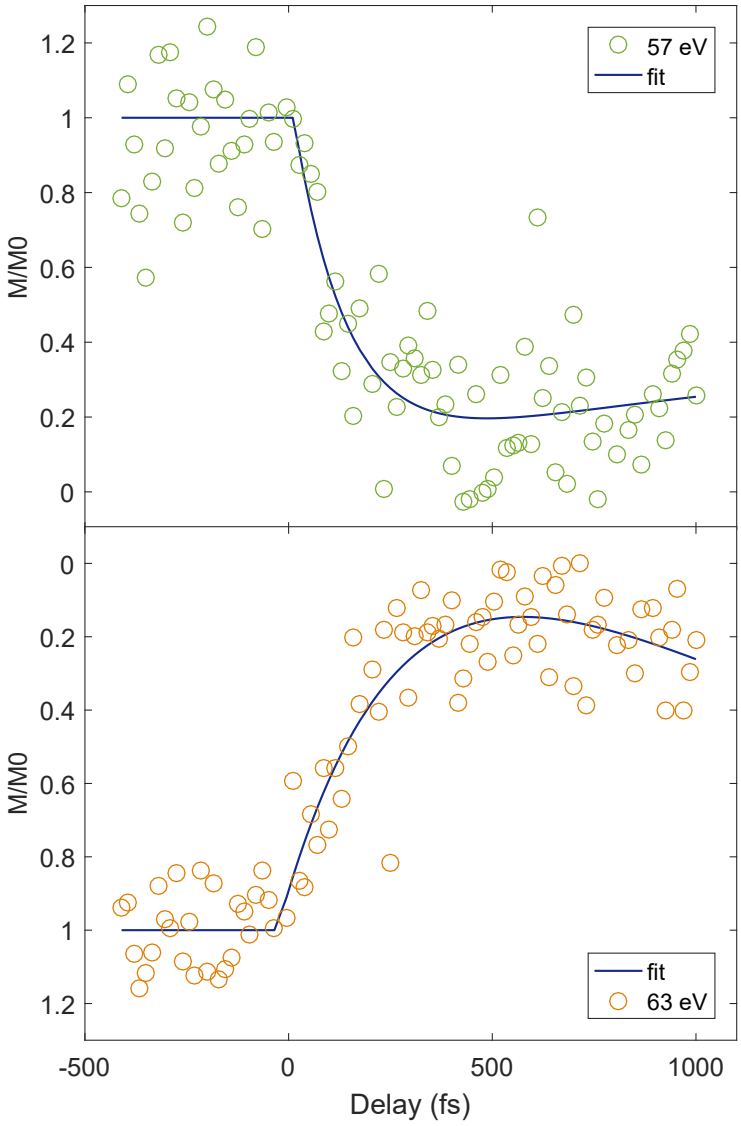

FIGURE 3.18: **Magnetization as a function of time delay for the Co/Pt multilayer.** Demagnetization curve obtained from the [Co(1.5 nm)/Pt(1.2 nm)]x5 multilayer for a pump fluence of 15 mJ cm^{-2}. For both curves no average of the data points was done. The solid lines represent the best fit.

signal intensity curves for $\vec{M}^-$ and $\vec{M}^+$ at 57 and 63 eV. The results show a successfully symmetric demagnetization of approximately 80 % for both energies around the cobalt M-edge. The effects between 57 and 63 eV in the Co/Pt multilayer are opposite, as foreseen in the measurement of A (figure 3.11) in the static results of the Co/Pt multilayer. The thermalization time (τ_M), characterized by the delay time at which the drop in magnetization reaches 63% of its maximum, is obtained from the fit, which gives $\tau_M \approx 150$ fs for both energies 57 and 63 eV. At 60 eV, since the main contribution for the Faraday effect is the ellipticity an extra measurement would have to be made (as explained in subsection 3.2.1, equation 3.12), corresponding to the null magnetization of the sample. By substituting the signal of $\vec{M}^+$ or $\vec{M}^-$ by $\vec{M}(0)$ one retrieve direct information about the demagnetization evolution at this energy, but quadratically proportional to it.

Once again, thanks to the harmonic polychromaticity, one can study the magnetization at different energies. In particular, the intensity and magnetization curves of the harmonics at 57 eV and 54 eV are compared on figure 3.19 a) and b), which correspond to the Faraday rotation before 60 eV at the Co M-edge. With the same purpose, figure 3.19 c) and d) compare the intensity and magnetization curves after 60 eV (63 eV and 66 eV). Analyzing the intensity curves in figure 3.19 a) and c), we observe an opposite variation of the signals for the two magnetization directions, characteristic of the rotation. Then, figure 3.19 b) and d) show that 54/57 eV and 63/66 eV have a common trend. Furthermore, a similar percentage of demagnetization ($\sim$ 80%) within a similar τ_M is observed, which seems to indicate that the effect is independent on the energy. These results demonstrate the big potential of our technique for the measurement of demagnetization dynamics of small sample's thicknesses.

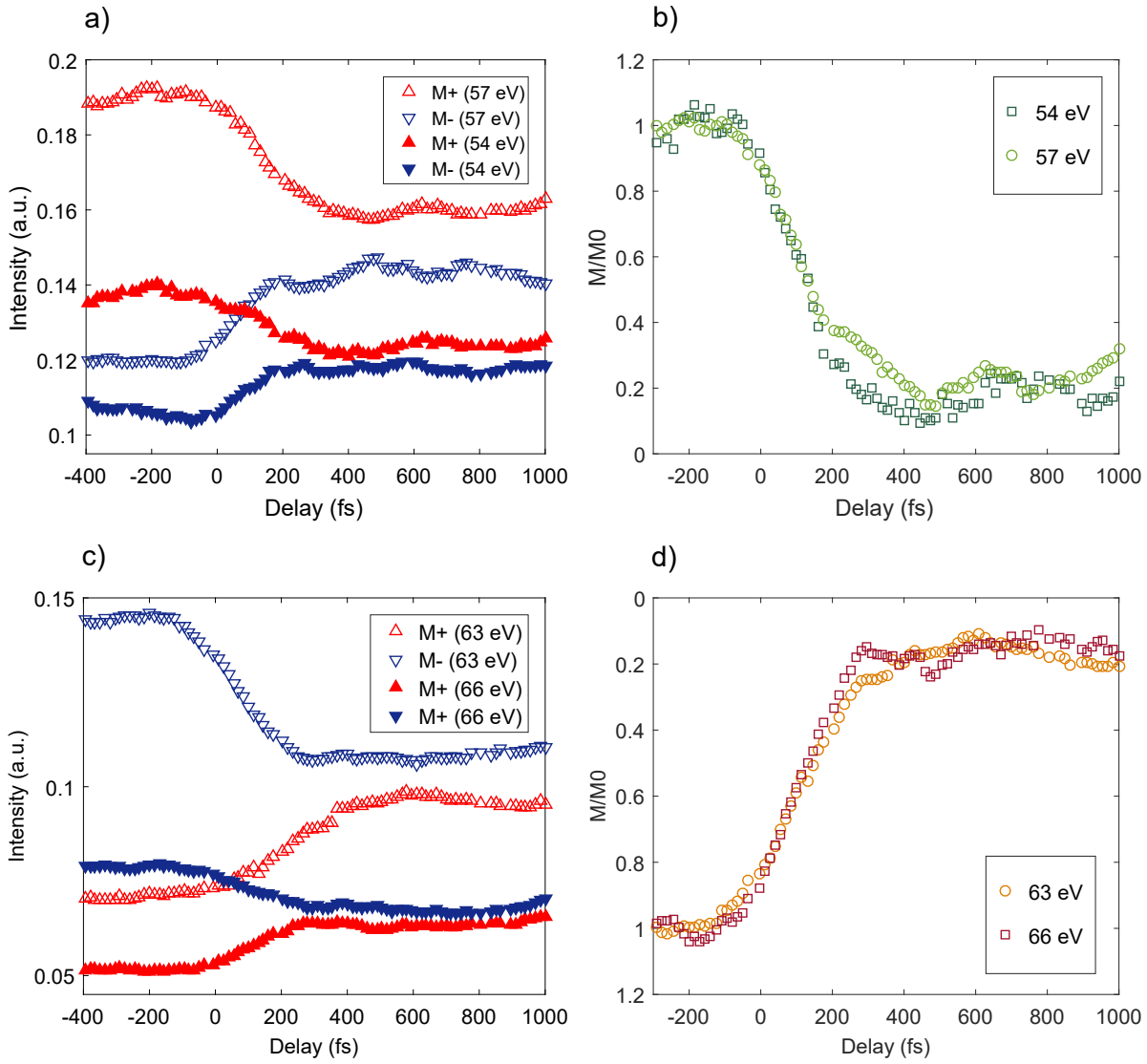

FIGURE 3.19: **Signal intensity and magnetization as a function of time delay for other energies of the Co/Pt multilayer.** The curves compare the signal intensity a) and the magnetization b) at 54 and 57 eV, and the signal intensity c) and the magnetization d) at 63 and 66 eV of the [Co(1.5 nm)/Pt(1.2 nm)]x5 multilayer. In all the curves each data point corresponds to a moving average of 15 neighboring elements.

Conclusions and Outlook

In this thesis, investigations of ultrafast magnetization dynamics in cobalt based materials were experimentally carried out. Among all the known magneto-optical effects used to characterize and probe the magnetization, the Faraday effect fits perfectly our experimental demands. For the first time, using simply generated linearly polarized harmonics, static and time-resolved experiments were realized through the magneto-optical Faraday effect. The pump-probe technique was used to obtain the dynamic response of the magnetic samples upon laser excitation. First, a strong laser pulse (pump) creates a perturbation in the sample, which results in a reduction of the macroscopic magnetization. Then, a time delayed weaker pulse (probe) resolves the evolution of the magnetization as function of time. The changes in the magnetization of the sample are associated to the changes in the polarization of the probe beam, i.e. the rotation and ellipticity induced by the magneto-optical Faraday effect. Thus, the measurements related with these two quantities, describe the magnetization, providing information about its dynamics. The materials under investigation are ferromagnetic samples, whose spins are aligned along a preferential axis, leading to a macroscopic magnetization. Cobalt based samples with different thicknesses, CoDy alloys and Co/Pt multilayers, establishing perpendicular magnetic anisotropy, were studied in the near EUV range around the cobalt M-edge at 60 eV.

The experimental work was accomplished using a femtosecond laser, which allows high temporal and spatial resolution, following the demand for faster and smaller storage technology of nowadays. Besides the interest of the industry in the investigation of laser-induced ultrafast demagnetization, the scientific community intends to solve the controversies in the proposed microscopic models describing the process of ultrafast demagnetization. In this regard, my thesis brings out a new approach to describe magnetization by means of the magneto-optical Faraday effect, using simply generated

linearly polarized high-order harmonics, which can clearly contribute to the advancement of these investigations. The highlight of our method lies on the versatility of the setup for any type of ferromagnetic material, magnetized out-of-plane, with no requirement for elliptical polarized light sources or samples with magnetic domains.

For both type of samples, CoDy and Co/Pt, our results indicated that the observed signal is, as we expected, significantly stronger than the XMCD signal one can obtain at these photon energies, which is the reference absorption experiment realized in a transmission geometry. These studies revealed similar dynamic behaviors for the two samples, in particular, the demagnetization time of cobalt, with 200 fs for CoDy and 150 fs for Co/Pt. Comparing the results for both type of samples, we observe an inversion of the magnetization response in the Co/Pt multilayers around the M-edge of cobalt between 57 eV and 63 eV. In addition, the results suggest that the main contribution of the Faraday effect at 57 and 63 eV is the rotation of the polarization, while at 60 eV it is dominated by the ellipticity. In one single measurement, this technique allows to retrieve information about both the ellipticity and the rotation in a quite large energy range, which are proportional to the magnetization. This is a great advantage compared to XMCD, where the detected effect is, in general, small and restricted to one single harmonic. Observing the magnetization dynamics simultaneously in a wide energy range, gives a completely different outlook of the demagnetization process. Being the first group to perform this experiment, one cannot predict the extra information associated to each energy around the material's edge.

The main results of my thesis demonstrate that measuring the Faraday rotation offers a sensitive way to characterize a thin film's magnetization via magnetically dichroic absorption spectroscopy. Indeed, with such temporal and spatial resolution, our method may enable the measurement of very small effects, unnoticed until then. Likewise, a small thickness of the sample is no longer a limitation since we demonstrated the investigation of very thin materials, such that we intend to exploit it to materials with a single layer of atoms. The polarizer, which is a key element in our setup, is the only limitation of this method. In the EUV range, our results prove that the effects are rather relevant to efficiently explore the magnetization dynamics of ferromagnetic materials. To observe the effect at higher photon energies, where the effects at the materials edges are stronger, especially in the hard x-ray range, no polarizer in reflection configuration exists so far. Yet, the concept of our method is suitable for FEL sources, which has

already been carried out by our team [149]. In conclusion, the capability of our newly technique to follow magnetization dynamics, simplifies the realization of time-resolved experiments, providing simultaneously information of the dynamics in a large energy range.

APPENDIX A

Polarimetry of a low and even-order harmonic: 4ω

Using the cross-polarized two-color ($\omega + 2\omega$) laser field technique developed in our group, highly coherent odd and even order harmonics, up to 70 eV and with high ellipticity, were generated [2]. This result sets up a great outlook for various applications based on dichroism effects, particularly for magnetism studies (XMCD). Yet, questions remained on the possibility that the radiation was not fully polarized. In addition, extended results to low order harmonics were previously studied [150], but in this study, no complete analysis of the harmonics polarization was performed. As a consequence, a full polarimetry analysis of a low-order harmonic is presented below, the 4^{th} harmonic.

Experimental setup

The experiment was conducted at LOA, in salle Corail, using the laser system described in subsection 2.3.1. More specifically, we investigated the degree and type of polarization of low order harmonics, in particular 4ω. This harmonic was spectrally isolated easily, using interferential filters, and then, its signal was directly measured on a photodiode.

For a complete polarimetry analysis of the radiation, a polarizer and an analyzer are required. The polarizer selects a specific polarization axis of the light for which the analyzer evaluates its rotation by doing a complete scan around the beam propagation axis. The polarized component is converted into light intensity, giving origin to a series

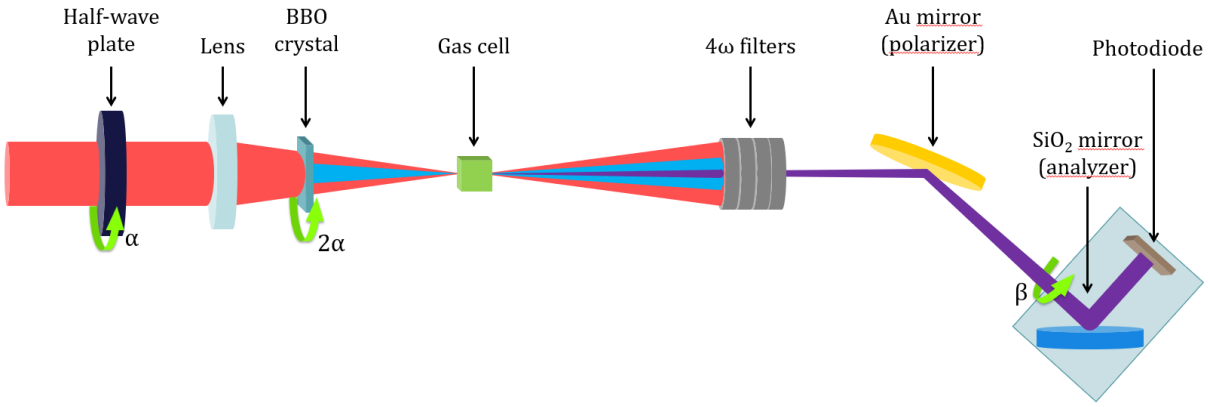

FIGURE A.1: **Layout of the first tentative experiment to perform the complete polarimetry of 4ω.** Cross-polarized two-color laser field configuration. The polarizer is a gold mirror (Brewster's angle at 67.5° of incidence), and the analyzer composed by a fused silica mirror at 45°. The harmonic is spectrally isolated using interferential filters, and then, its signal is measured on a photodiode. α and β corresponds to the angles that should be turned to perform the complete polarimetry. For each α, a complete scan of β is done.

of sinusoidals that have all to be fitted to get exactly the Stokes' parameters. The Stokes' parameters S_1 and S_2 give information on the linear polarization and S_3 on the degree of elliptical polarization. Throughout this experimental work, two different experimental apparatus were used to perform a complete polarimetry analysis of 4ω.

The first experimental apparatus is schematically represented in figure A.1. To characterize the polarization properties of the 4^{th} harmonic, the Stokes' parameters described in 2.2.3.2.2, were evaluated through an entirely optical technique, for which a half-wave plate, a fixed polarizing mirror and an analyzer are employed. This simple approach requires the rotation of the source polarization axis for a fixed position of the polarizer. For different rotation angle positions of the half-wave plate (α), the analyzer rotates around the harmonic beam propagation axis (β), acquiring the harmonic signal on the photodiode. In order to maintain the cross-polarized laser field between ω and 2ω, the 0.2 mm thick BBO crystal should rotate along with the half-wave plate by 2α. However, this experimental configuration showed an issue while rotating the half-wave plate and the BBO. Depending on α, the intensity of 2ω was not perfectly constant, introducing a difficulty in the data analysis and an important uncertainty.

An alternative and more classical experimental apparatus was then assembled, which is represented in figure A.2. Before the interferential filters, the configuration is the same as in the previous configuration but the half-wave plate and the BBO crystal are

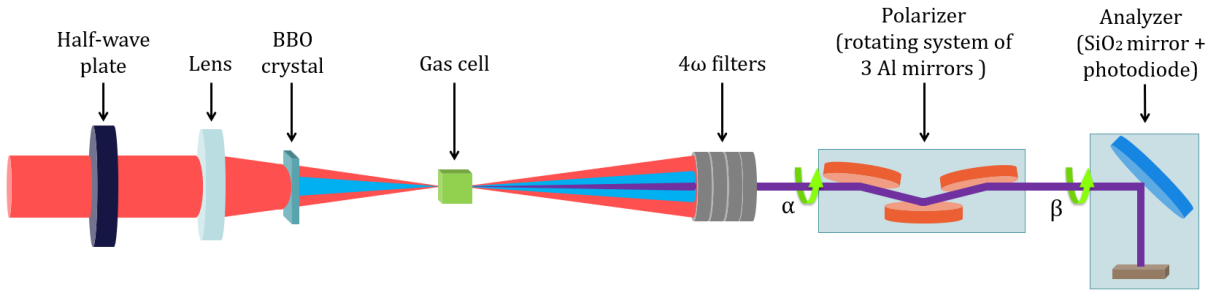

FIGURE A.2: **Layout of the final configuration to perform the complete polarimetry of 4ω.** The half-wave plate and BBO crystal are fixed and a rotating system with three Al mirrors at grazing incidence was used as a polarizer. The analyzer is similar to the previous experimental configuration.

in a fixed position, establishing a cross-polarized two-color laser field configuration. After the interferential filters, which selects the harmonics of interest (4ω), a rotating polarizer system composed of three Al mirrors at grazing incidence substitutes the previous fixed polarizer composed of a Au mirror. This new rotating polarizer system is quite difficult to introduce in the setup since it should be simultaneously robust and stable. Here, for different rotation angle positions of the polarizer (α), the analyzer rotates around the harmonic beam propagation axis (β), acquiring the harmonic signal on the photodiode.

Results and Discussion

Resulting from the first experimental configuration, the graphs from figure A.3 show the experimental data for 8 consecutive rotation angle positions of the half-wave plate for the 4^{th} harmonic. In order to obtain the Stokes' parameters, which allow to calculate the polarization and ellipticity degrees of 4ω, the experimental data must be fitted. The Stokes' parameters are obtained from a recursive program by introducing initial random variables and then substituting the initial guess by the values obtained from the program. This process is repeated until a good agreement between the fit and the experimental data is obtained. P and ε are calculated from the obtained Stokes' parameters according to equations 2.22 and 2.24, respectively. The fit equation corresponds the transmitted Stokes vector using Mueller matrices representing each optical element, in particular the polarizer and the analyzer (see 2.2.3.2.2).

As said before, an unexpected change of the 2ω intensity is observed while rotating

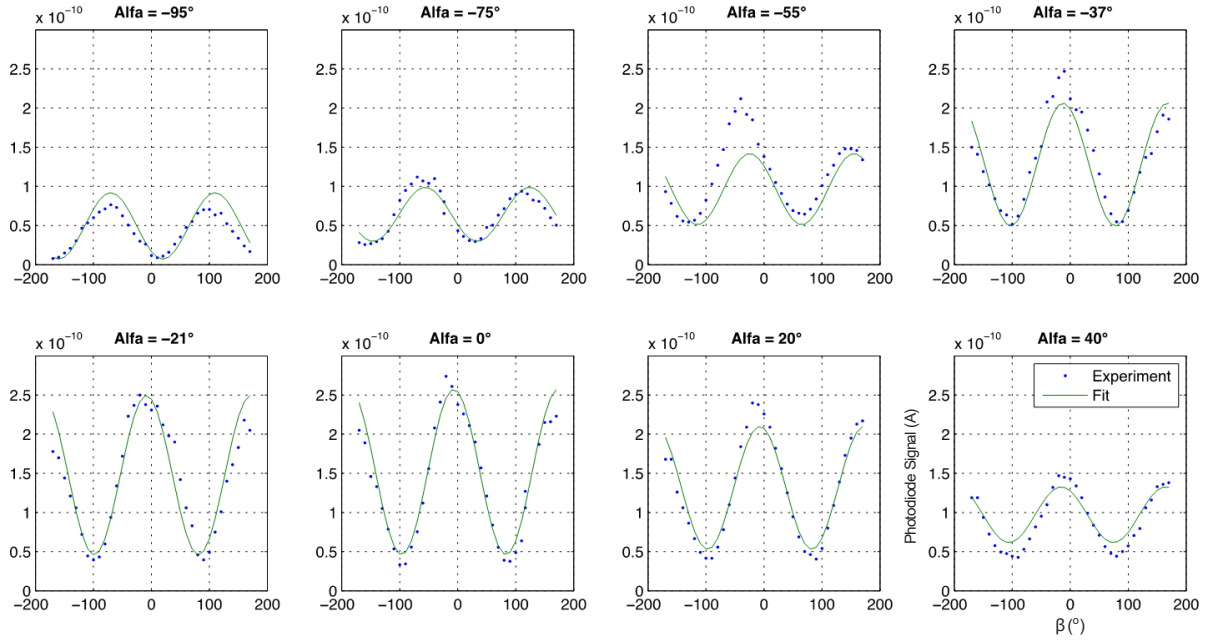

FIGURE A.3: **Variation of the harmonic signal for the 4^{th} harmonic as function of the β angle.** The experimental data is presented in blue and the respective fits in green for eight different positions of the half-wave plate. For each rotation angle position of the half-wave plate (α), the analyzer rotates around the harmonic beam propagation axis (β), acquiring the harmonic signal on the photodiode.

the half-wave plate and the BBO crystal. Due to this behavior, it becomes difficult to correctly fit all the curves at the same time, resulting in a bad fit for some α angles, for example -55°, -37° and 20° in figure A.3. In reality, we did the measurement for 14 rotation angle positions of the half-wave plate, however the fit with all the graphs introduces a phase shift problem in addition to the intensity change. This behavior is probably a consequence of non constant intensity of 2ω with α, which we cannot explain. The respective Stokes' parameters extracted from these graphs are summarized in table A.1, which shows a fully polarized light (P=1) with 20% of ellipticity (ε). However, one should notice that these results have an important error bar due to the half-wave plate/BBO issues explained above.

S_1	S_2	S_2	P	ε
-0.9	-0.2	0.4	1.0	0.2

TABLE A.1: **Experimentally obtained Stokes' parameters for the first experimental configuration.** S_1 and S_2 give information on the linear polarization and S_3 on the degree of elliptical polarization. P gives the degree of polarization (1 corresponds to fully polarized beam).

Figure A.4 shows the graphs for the second experimental apparatus for 16 positions

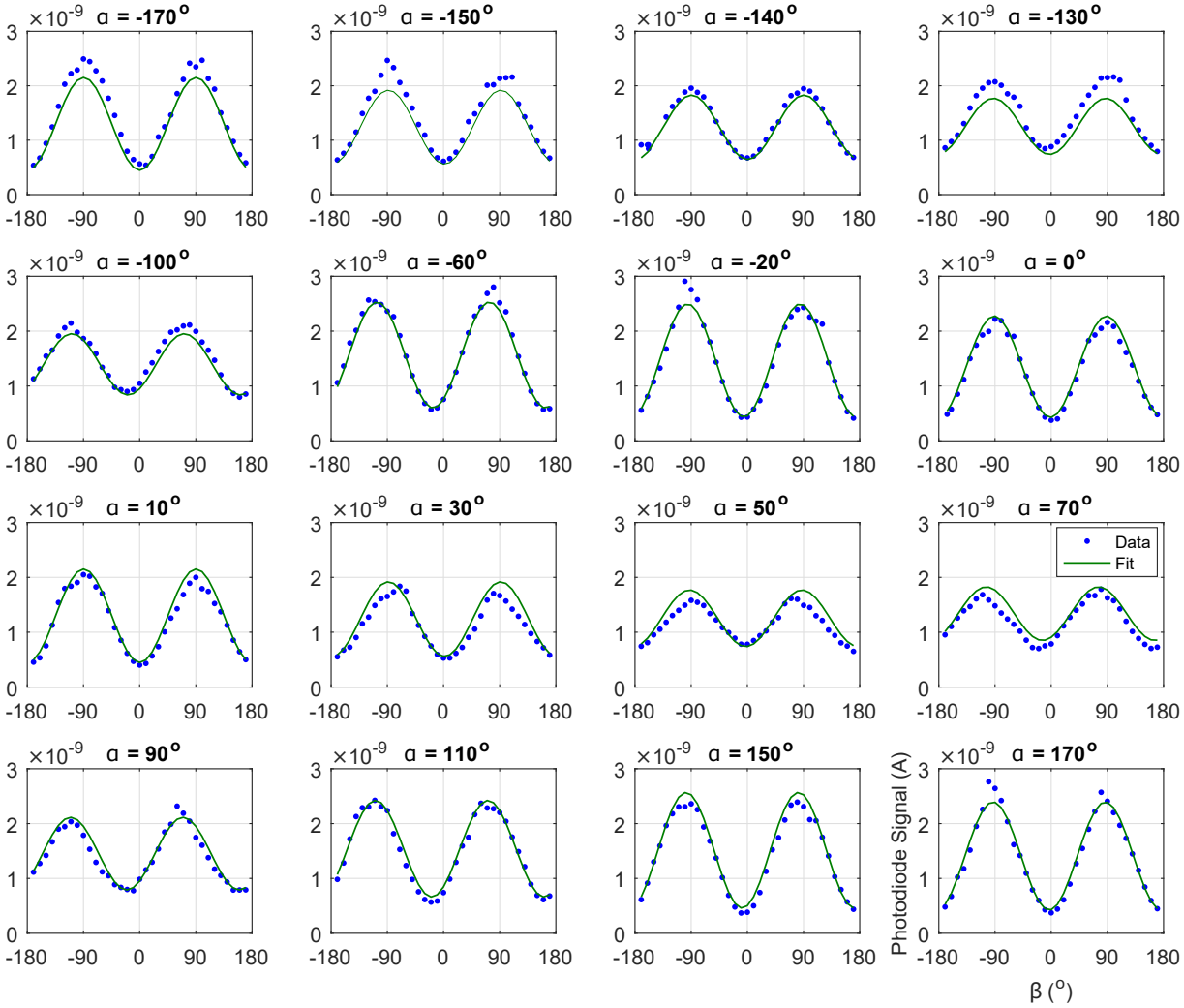

FIGURE A.4: **Variation of the harmonic signal for the 4^{th} harmonic as function of the β angle.** The experimental data is presented in blue and the respective fits in green for sixteen different positions of the analyzer. For each rotation angle position of the analyzer (α), the polarizer rotates around the harmonic beam propagation axis (β), acquiring the harmonic signal on the photodiode.

of the rotating polarizer system ($-170° \leq \alpha \leq 170°$). Contrary to the results obtained with the first experimental configuration, the intensity of the signal is independent of α, meaning the intensity of 2ω is constant throughout the experiment. Consequently, one obtain a good agreement between the experimental data and the respective fit for every α. The respective extracted parameters are summarized in table A.2. The radiation is fully polarized with an ellipticity degree of 43%. Considering other sets of

S_1	S_2	S_2	P	ε
0.65	-0.21	0.73	1.00	0.43

TABLE A.2: **Experimentally obtained Stokes' parameters for the second experimental configuration.**

data with near laser properties, an average of the 4ω polarization degree was obtained, P=0.97$\pm$0.05, meaning that the radiation is always fully polarized. In contrast, the ellipticity drastically varies from a full measurement to another, from almost nearly 0 to 0.5. Such variations are not understood bu it could come from the slight variation of the intensity ratio between ω and 2ω.

Conclusion

This work presents a first full characterization of the polarization state of a low and even-order harmonic in a cross-polarized two-color laser field configuration. The analysis of the polarization of 4ω showed that the harmonics are fully polarized with a significant degree of ellipticity. From these results, one can extend the investigations to higher order harmonics.

Bibliography

[1] E. Beaurepaire, J.-C. Merle, A. Daunois, *et al.*, "Ultrafast spin dynamics in ferromagnetic nickel", *Phys. Rev. Lett.*, vol. 76, pp. 4250–4253, 22 1996. DOI: 10.1103/PhysRevLett.76.4250 (Cited on pages 1, 7, 16–19).

[2] G. Lambert, B. Vodungbo, J. Gautier, *et al.*, "Towards enabling femtosecond helicity-dependent spectroscopy with high-harmonic sources.", *Nature Communications*, vol. 6, p. 6167, 2015. DOI: 10.1038/ncomms7167 (Cited on pages 2, 46, 47, 58, 91).

[3] F. Willems, C. T. Smeenk, N. Zhavoronkov, *et al.*, "Probing ultrafast spin dynamics with high-harmonic magnetic circular dichroism spectroscopy", *Physical Review B - Condensed Matter and Materials Physics*, vol. 92, no. 22, pp. 1–5, 2015. DOI: 10.1103/PhysRevB.92.220405 (Cited on pages 2, 46, 58, 74).

[4] H.-C. Mertins, S. Valencia, D. Abramsohn, *et al.*, "X-ray Kerr rotation and ellipticity spectra at the 2 p edges of Fe, Co, and Ni", *Physical Review B*, vol. 69, no. 6, p. 064 407, 2004. DOI: 10.1103/PhysRevB.69.064407 (Cited on pages 2, 58).

[5] C. La-O-Vorakiat, M. Siemens, M. M. Murnane, *et al.*, "Ultrafast demagnetization dynamics at the M edges of magnetic elements observed using a tabletop high-harmonic soft X-ray source", *Physical Review Letters*, vol. 103, no. 25, pp. 1–4, 2009. DOI: 10.1103/PhysRevLett.103.257402 (Cited on pages 2, 58).

[6] C. La-O-Vorakiat, E. Turgut, C. A. Teale, *et al.*, "Ultrafast demagnetization measurements using extreme ultraviolet light: Comparison of electronic and magnetic contributions", *Physical Review X*, vol. 2, no. 1, pp. 1–7, 2012. DOI: 10.1103/PhysRevX.2.011005 (Cited on pages 2, 58).

[7] B. Vodungbo, J. Gautier, G. Lambert, *et al.*, "Laser-induced ultrafast demagnetization in the presence of a nanoscale magnetic domain network", *Nature Communications*, vol. 3, p. 999, 2012. DOI: 10.1038/ncomms2007 (Cited on pages 2, 13, 14, 29, 58).

[8] R. Elliott, "The story of magnetism", *Physica A: Statistical Mechanics and its Applications*, vol. 384, no. 1, pp. 44 –52, 2007, STATPHYS - KOLKATA VI. DOI: https://doi.org/10.1016/j.physa.2007.04.068 (Cited on page 6).

[9] J. Bass and W. P. P. Jr, "Spin-diffusion lengths in metals and alloys, and spin-flipping at metal/metal interfaces: An experimentalist's critical review", *Journal of Physics: Condensed Matter*, vol. 19, no. 18, p. 183 201, 2007 (Cited on page 6).

[10] F. Batallan, I. Rosenman, and C. B. Sommers, "Band structure and fermi surface of hcp ferromagnetic cobalt", *Phys. Rev. B*, vol. 11, pp. 545–557, 1 1975. DOI: 10.1103/PhysRevB.11.545 (Cited on page 6).

[11] M. Battiato, G. Barbalinardo, K. Carva, *et al.*, "Beyond linear response theory for intensive light-matter interactions: Order formalism and ultrafast transient dynamics", *Phys. Rev. B*, vol. 85, p. 045 117, 4 2012. DOI: 10.1103/PhysRevB.85.045117 (Cited on page 6).

[12] C Brombacher, M Grobis, J Lee, *et al.*, "L1 0 feptcu bit patterned media", *Nanotechnology*, vol. 23, no. 2, p. 025 301, 2012 (Cited on page 6).

[13] M. H. Kryder, E. C. Gage, T. W. McDaniel, *et al.*, "Heat assisted magnetic recording", *Proceedings of the IEEE*, vol. 96, no. 11, pp. 1810–1835, 2008. DOI: 10.1109/JPROC.2008.2004315 (Cited on page 6).

[14] B. Dieny, M. Chshiev, B. Charles, *et al.*, "Impact of intergrain spin transfer torques due to huge thermal gradients on the performance of heat assisted magnetic recording", *arXiv preprint arXiv:1712.03302*, 2017 (Cited on page 7).

[15] H. G. S. Technologies", *Patterned magnetic media*. eprint: https://www.hgst.com/ (Cited on page 7).

[16] L. Pan and D. B. Bogy, "Data storage: Heat-assisted magnetic recording", *Nature Photonics*, vol. 3, no. 4, p. 189, 2009 (Cited on page 7).

[17] M. Faraday, "On the magnetization of light and the illumination of magnetic lines of force", *Philosophical Transactions of the Royal Society of London*, vol. 136, pp. 1–20, 1846 (Cited on page 8).

[18] J. K. LL.D., "Xliii. on rotation of the plane of polarization by reflection from the pole of a magnet", *The London, Edinburgh, and Dublin Philosophical Magazine and Journal of Science*, vol. 3, no. 19, pp. 321–343, 1877. DOI: 10.1080/14786447708639245 (Cited on pages 8, 12).

[19] I. Crassee, J. Levallois, A. L. Walter, *et al.*, "Giant faraday rotation in single-and multilayer graphene", *Nature Physics*, vol. 7, no. 1, p. 48, 2011 (Cited on page 9).

[20] S. Valencia, A. Gaupp, W. Gudat, *et al.*, "Faraday rotation spectra at shallow core levels: 3p edges of Fe, Co, and Ni", *New Journal of Physics*, vol. 8, pp. 1–11, 2006. DOI: 10.1088/1367-2630/8/10/254 (Cited on pages 10, 11, 57, 61, 62, 73).

[21] P. Oppeneer, "Handbook of magnetic materials", *Vol. 13Elsevier, Amsterdam*, 2001 (Cited on page 10).

[22] J. Kunes, P. M. Oppeneer, H.-C. Mertins, *et al.*, "X-ray faraday effect at the l2,3 edges of fe, co, and ni: Theory and experiment", *Phys. Rev. B*, vol. 64, p. 174 417, 17 2001. DOI: 10.1103/PhysRevB.64.174417 (Cited on page 11).

[23] S. Yamamoto and I. Matsuda, "Measurement of the resonant magneto-optical kerr effect using a free electron laser", *Applied Sciences*, vol. 7, no. 7, 2017. DOI: 10.3390/app7070662 (Cited on page 11).

[24] "SPring-8". eprint: http://www.spring8.or.jp/wkg/BL39XU/solution/lang-en/SOL-0000001032?set_language=en&cl=en (Cited on page 12).

[25] "SLAC". eprint: https://www-ssrl.slac.stanford.edu/stohr/xmcd.htm (Cited on page 12).

[26] B. Vodungbo, A. Barszczak Sardinha, J. Gautier, *et al.*, "Table-top resonant magnetic scattering with extreme ultraviolet light from high-order harmonic generation", *EPL (Europhysics Letters)*, vol. 94, no. 5, p. 54 003, 2011. DOI: 10.1209/0295-5075/94/54003 (Cited on page 14).

[27] B Pfau, S Schaffert, L Müller, *et al.*, "Ultrafast optical demagnetization manipulates nanoscale spin structure in domain walls", *Nature communications*, vol. 3, p. 1100, 2012 (Cited on pages 14, 25).

[28] A. Merhe, "Ultrafast modification of the magnetic anisotropy in a cotb alloy", PhD thesis, 2018 (Cited on page 14).

[29] L. Landau and E. Lifshitz, "On the theory of the dispersion of magnetic permeability in ferromagnetic bodies", *Phys. Z. Sowjetunion*, vol. 8, no. 153, pp. 101–114, 1935 (Cited on pages 15, 17).

[30] T. L. Gilbert, "A phenomenological theory of damping in ferromagnetic materials", *IEEE Transactions on Magnetics*, vol. 40, no. 6, pp. 3443–3449, 2004. DOI: 10.1109/TMAG.2004.836740 (Cited on page 15).

[31] A. Vaterlaus, T. Beutler, and F. Meier, "Spin-lattice relaxation time of ferromagnetic gadolinium determined with time-resolved spin-polarized photoemission", *Phys. Rev. Lett.*, vol. 67, pp. 3314–3317, 23 1991. DOI: 10.1103/PhysRevLett.67.3314 (Cited on page 16).

[32] A. Vaterlaus, T. Beutler, D. Guarisco, *et al.*, "Spin-lattice relaxation in ferromagnets studied by time-resolved spin-polarized photoemission", *Phys. Rev. B*, vol. 46, pp. 5280–5286, 9 1992. DOI: 10.1103/PhysRevB.46.5280 (Cited on page 16).

[33] J. Hohlfeld, E. Matthias, R. Knorren, *et al.*, "Nonequilibrium magnetization dynamics of nickel", *Phys. Rev. Lett.*, vol. 78, pp. 4861–4864, 25 1997. DOI: 10.1103/PhysRevLett.78.4861 (Cited on page 16).

[34] A. Scholl, L. Baumgarten, R. Jacquemin, *et al.*, "Ultrafast spin dynamics of ferromagnetic thin films observed by fs spin-resolved two-photon photoemission", *Phys. Rev. Lett.*, vol. 79, pp. 5146–5149, 25 1997. DOI: 10.1103/PhysRevLett.79.5146 (Cited on page 16).

[35] M. van Kampen, C. Jozsa, J. T. Kohlhepp, *et al.*, "All-optical probe of coherent spin waves", *Phys. Rev. Lett.*, vol. 88, p. 227 201, 22 2002. DOI: 10.1103/PhysRevLett.88.227201 (Cited on page 16).

[36] E Beaurepaire, G. Turner, S. Harrel, *et al.*, "Coherent terahertz emission from ferromagnetic films excited by femtosecond laser pulses", *Applied Physics Letters*, vol. 84, no. 18, pp. 3465–3467, 2004 (Cited on page 16).

[37] G. Ju, A. V. Nurmikko, R. F. C. Farrow, *et al.*, "Ultrafast optical modulation of an exchange biased ferromagnetic/antiferromagnetic bilayer", *Phys. Rev. B*, vol. 58, R11857–R11860, 18 1998. DOI: 10.1103/PhysRevB.58.R11857 (Cited on page 16).

[38] G. Ju, A. V. Nurmikko, R. F. C. Farrow, *et al.*, "Ultrafast time resolved photoinduced magnetization rotation in a ferromagnetic/ antiferromagnetic exchange coupled system", *Phys. Rev. Lett.*, vol. 82, pp. 3705–3708, 18 1999. DOI: 10.1103/PhysRevLett.82.3705 (Cited on page 16).

[39] G. Ju, L. Chen, A. V. Nurmikko, *et al.*, "Coherent magnetization rotation induced by optical modulation in ferromagnetic/ antiferromagnetic exchange-coupled bilayers", *Phys. Rev. B*, vol. 62, pp. 1171–1177, 2 2000. DOI: 10.1103/PhysRevB.62.1171 (Cited on page 16).

[40] A. Kirilyuk, A. V. Kimel, and T. Rasing, "Ultrafast optical manipulation of magnetic order", *Rev. Mod. Phys.*, vol. 82, pp. 2731–2784, 3 2010. DOI: 10.1103/RevModPhys.82.2731 (Cited on page 16).

[41] M. Cinchetti, M. Sánchez Albaneda, D. Hoffmann, *et al.*, "Spin-flip processes and ultrafast magnetization dynamics in co: Unifying the microscopic and macroscopic view of femtosecond magnetism", *Phys. Rev. Lett.*, vol. 97, p. 177 201, 17 2006. DOI: 10.1103/PhysRevLett.97.177201 (Cited on page 16).

[42] B Koopmans, G Malinowski, F Dalla Longa, *et al.*, "Explaining the paradoxical diversity of ultrafast laser-induced demagnetization", *Nature materials*, vol. 9, no. 3, p. 259, 2010 (Cited on pages 16, 18, 21).

[43] M. Krauß, T. Roth, S. Alebrand, *et al.*, "Ultrafast demagnetization of ferromagnetic transition metals: The role of the coulomb interaction", *Phys. Rev. B*, vol. 80, p. 180 407, 18 2009. DOI: 10.1103/PhysRevB.80.180407 (Cited on page 16).

[44] J.-Y. Bigot, M. Vomir, and E. Beaurepaire, "Coherent ultrafast magnetism induced by femtosecond laser pulses", *Nature Physics*, vol. 5, no. 7, p. 515, 2009 (Cited on page 16).

[45] M. Battiato, K. Carva, and P. M. Oppeneer, "Superdiffusive spin transport as a mechanism of ultrafast demagnetization", *Phys. Rev. Lett.*, vol. 105, p. 027 203, 2 2010. DOI: 10.1103/PhysRevLett.105.027203 (Cited on pages 16, 22).

[46] U. Atxitia, O. Chubykalo-Fesenko, J. Walowski, *et al.*, "Evidence for thermal mechanisms in laser-induced femtosecond spin dynamics", *Phys. Rev. B*, vol. 81, p. 174 401, 17 2010. DOI: 10.1103/PhysRevB.81.174401 (Cited on page 16).

[47] A. B. Schmidt, M. Pickel, M. Donath, *et al.*, "Ultrafast magnon generation in an fe film on cu(100)", *Phys. Rev. Lett.*, vol. 105, p. 197 401, 19 2010. DOI: 10.1103/PhysRevLett.105.197401 (Cited on page 16).

[48] M. Sultan, A. Melnikov, and U. Bovensiepen, "Ultrafast magnetization dynamics of gd(0001): Bulk versus surface", *physica status solidi (b)*, vol. 248, no. 10, pp. 2323–2329, DOI: 10.1002/pssb.201147105 (Cited on page 16).

[49] T. Gilbert, "A lagrangian formulation of the gyromagnetic equation of the magnetization field", *Phys. Rev.*, vol. 100, p. 1243, 1955 (Cited on page 17).

[50] F. Bloch, "Nuclear induction", *Phys. Rev.*, vol. 70, pp. 460–474, 7-8 1946. DOI: 10.1103/PhysRev.70.460 (Cited on page 18).

[51] U. Atxitia, O. Chubykalo-Fesenko, N. Kazantseva, *et al.*, "Micromagnetic modeling of laser-induced magnetization dynamics using the landau-lifshitz-bloch equation", *Applied Physics Letters*, vol. 91, no. 23, p. 232 507, 2007 (Cited on page 18).

[52] A. Kirilyuk, A. V. Kimel, and T. Rasing, "Ultrafast optical manipulation of magnetic order", *Reviews of Modern Physics*, vol. 82, no. 3, p. 2731, 2010 (Cited on page 18).

[53] E. Turgut, "Studying laser-induced spin currents using ultrafast extreme ultraviolet light", 2014 (Cited on page 18).

[54] B. Koopmans, J. J. M. Ruigrok, F. D. Longa, *et al.*, "Unifying ultrafast magnetization dynamics", *Phys. Rev. Lett.*, vol. 95, p. 267 207, 26 2005. DOI: 10.1103/PhysRevLett.95.267207 (Cited on pages 18, 21).

[55] C. La-O-Vorakiat, "Element-selective ultrafast magnetization dynamics with a tabletop light source", PhD thesis, 2011 (Cited on page 19).

[56] G. P. Zhang and T. F. George, "Total angular momentum conservation in laser-induced femtosecond magnetism", *Phys. Rev. B*, vol. 78, p. 052 407, 5 2008. DOI: 10.1103/PhysRevB.78.052407 (Cited on page 20).

[57] S. Mathias, C. La-O-Vorakiat, P. Grychtol, *et al.*, "Probing the timescale of the exchange interaction in a ferromagnetic alloy", *Proceedings of the National Academy of Sciences*, 2012. DOI: 10.1073/pnas.1201371109 (Cited on page 20).

[58] R. J. Elliott, "Theory of the effect of spin-orbit coupling on magnetic resonance in some semiconductors", *Phys. Rev.*, vol. 96, pp. 266–279, 2 1954. DOI: 10.1103/PhysRev.96.266 (Cited on page 21).

[59] S. Essert and H. C. Schneider, "Electron-phonon scattering dynamics in ferromagnetic metals and their influence on ultrafast demagnetization processes", *Phys. Rev. B*, vol. 84, p. 224 405, 22 2011. DOI: 10.1103/PhysRevB.84.224405 (Cited on page 21).

[60] D. Rudolf, L.-O. Chan, M. Battiato, *et al.*, "Ultrafast magnetization enhancement in metallic multilayers driven by superdiffusive spin current", *Nature communications*, vol. 3, p. 1037, 2012 (Cited on pages 22, 23, 25).

[61] A. Schellekens, W Verhoeven, T. Vader, *et al.*, "Investigating the contribution of superdiffusive transport to ultrafast demagnetization of ferromagnetic thin films", *Applied Physics Letters*, vol. 102, no. 25, p. 252 408, 2013. DOI: 10.1063/1.4812658 (Cited on page 22).

[62] A. Sakdinawat and D. Attwood, "Nanoscale x-ray imaging", *Nature photonics*, vol. 4, no. 12, p. 840, 2010 (Cited on page 24).

[63] G. Tallents, E. Wagenaars, and G. Pert, "Optical lithography: Lithography at euv wavelengths", *Nature Photonics*, vol. 4, no. 12, p. 809, 2010 (Cited on page 24).

[64] I Radu, K Vahaplar, C Stamm, *et al.*, "Transient ferromagnetic-like state mediating ultrafast reversal of antiferromagnetically coupled spins", *Nature*, vol. 472, no. 7342, p. 205, 2011 (Cited on page 25).

[65] C Stamm, T Kachel, N Pontius, *et al.*, "Femtosecond modification of electron localization and transfer of angular momentum in nickel", *Nature materials*, vol. 6, no. 10, p. 740, 2007 (Cited on page 25).

[66] T. Wang, D. Zhu, B. Wu, *et al.*, "Femtosecond single-shot imaging of nanoscale ferromagnetic order in co/pd multilayers using resonant x-ray holography", *Phys. Rev. Lett.*, vol. 108, p. 267 403, 26 2012. DOI: 10.1103/PhysRevLett.108.267403 (Cited on page 25).

[67] C. La-O-Vorakiat, M. Siemens, M. M. Murnane, *et al.*, "Ultrafast demagnetization dynamics at the *m* edges of magnetic elements observed using a tabletop high-harmonic soft x-ray source", *Phys. Rev. Lett.*, vol. 103, p. 257 402, 25 2009. DOI: 10.1103/PhysRevLett.103.257402 (Cited on page 25).

[68] C. La-O-Vorakiat, E. Turgut, C. A. Teale, *et al.*, "Ultrafast demagnetization measurements using extreme ultraviolet light: Comparison of electronic and magnetic contributions", *Phys. Rev. X*, vol. 2, p. 011 005, 1 2012. DOI: 10.1103/PhysRevX.2.011005 (Cited on page 25).

[69] E. Turgut, C. La-o vorakiat, J. M. Shaw, *et al.*, "Controlling the competition between optically induced ultrafast spin-flip scattering and spin transport in magnetic multilayers", *Phys. Rev. Lett.*, vol. 110, p. 197 201, 19 2013. DOI: 10.1103/PhysRevLett.110.197201 (Cited on page 25).

[70] S. Khan, K. Holldack, T. Kachel, *et al.*, "Femtosecond undulator radiation from sliced electron bunches", *Phys. Rev. Lett.*, vol. 97, p. 074 801, 7 2006. DOI: 10.1103/PhysRevLett.97.074801 (Cited on page 26).

[71] C. Pellegrini and J. Stöhr, "X-ray free-electron lasers—principles, properties and applications", *Nuclear Instruments and Methods in Physics Research Section A: Accelerators, Spectrometers, Detectors and Associated Equipment*, vol. 500, no. 1, pp. 33 –40, 2003, NIMA Vol 500. DOI: https://doi.org/10.1016/S0168-9002(03)00739-3 (Cited on page 26).

[72] "EuropeanXFEL". eprint: https://www.xfel.eu/ (Cited on page 27).

[73] "LEAPS", *European facilities*. eprint: https://www.leaps-initiative.eu/synchrotrons/european_facilities/ (Cited on page 27).

[74] T. Ditmire, E. T. Gumbrell, R. A. Smith, *et al.*, "Spatial coherence measurement of soft x-ray radiation produced by high order harmonic generation", *Phys. Rev. Lett.*, vol. 77, pp. 4756–4759, 23 1996. DOI: 10.1103/PhysRevLett.77.4756 (Cited on page 29).

[75] R. A. Bartels, A. Paul, H. Green, *et al.*, "Generation of spatially coherent light at extreme ultraviolet wavelengths", *Science*, vol. 297, no. 5580, pp. 376–378, 2002. DOI: 10.1126/science.1071718 (Cited on page 29).

[76] C. Lyngå, M. B. Gaarde, C. Delfin, *et al.*, "Temporal coherence of high-order harmonics", *Phys. Rev. A*, vol. 60, pp. 4823–4830, 6 1999. DOI: 10.1103/PhysRevA.60.4823 (Cited on page 29).

[77] Z. Chang, A. Rundquist, H. Wang, *et al.*, "Generation of coherent soft x rays at 2.7 nm using high harmonics", *Phys. Rev. Lett.*, vol. 79, pp. 2967–2970, 16 1997. DOI: 10.1103/PhysRevLett.79.2967 (Cited on pages 29, 56).

[78] M. Schnürer, C. Spielmann, P. Wobrauschek, *et al.*, "Coherent 0.5-kev x-ray emission from helium driven by a sub-10-fs laser", *Phys. Rev. Lett.*, vol. 80, pp. 3236–3239, 15 1998. DOI: 10.1103/PhysRevLett.80.3236 (Cited on page 29).

[79] D. Descamps, L. Roos, C. Delfin, *et al.*, "Two- and three-photon ionization of rare gases using femtosecond harmonic pulses generated in a gas medium", *Phys. Rev. A*, vol. 64, p. 031 404, 3 2001. DOI: 10.1103/PhysRevA.64.031404 (Cited on page 29).

[80] N. A. Papadogiannis, B. Witzel, C. Kalpouzos, *et al.*, "Observation of attosecond light localization in higher order harmonic generation", *Phys. Rev. Lett.*, vol. 83, pp. 4289–4292, 21 1999. DOI: 10.1103/PhysRevLett.83.4289 (Cited on page 29).

[81] Y. Mairesse, A. de Bohan, L. J. Frasinski, *et al.*, "Attosecond synchronization of high-harmonic soft x-rays", *Science*, vol. 302, no. 5650, pp. 1540–1543, 2003. DOI: 10.1126/science.1090277 (Cited on page 29).

[82] E. Goulielmakis, M. Schultze, M. Hofstetter, *et al.*, "Single-cycle nonlinear optics", *Science*, vol. 320, no. 5883, pp. 1614–1617, 2008. DOI: 10.1126/science.1157846 (Cited on page 29).

[83] S. L. Sorensen, O. Björneholm, I. Hjelte, *et al.*, "Femtosecond pump–probe photoelectron spectroscopy of predissociative rydberg states in acetylene", *The Journal of Chemical Physics*, vol. 112, no. 18, pp. 8038–8042, 2000. DOI: 10.1063/1.481402 (Cited on page 29).

[84] P. A. Franken, A. E. Hill, C. W. Peters, *et al.*, "Generation of optical harmonics", *Phys. Rev. Lett.*, vol. 7, pp. 118–119, 4 1961. DOI: 10.1103/PhysRevLett.7.118 (Cited on page 29).

[85] G. H. C. New and J. F. Ward, "Optical third-harmonic generation in gases", *Phys. Rev. Lett.*, vol. 19, pp. 556–559, 10 1967. DOI: 10.1103/PhysRevLett.19.556 (Cited on page 29).

[86] A. McPherson, G. Gibson, H. Jara, *et al.*, "Studies of multiphoton production of vacuum-ultraviolet radiation in the rare gases", *Journal of the Optical Society of America B*, vol. 4, no. 4, p. 595, 1987. DOI: 10.1364/JOSAB.4.000595 (Cited on page 30).

[87] P. B. Corkum, "Plasma perspective on strong field multiphoton ionization", *Physical Review Letters*, vol. 71, no. 13, pp. 1994–1997, 1993. DOI: 10.1103/PhysRevLett.71.1994. eprint: 1011.1669 (Cited on pages 30, 31, 38).

[88] J. L. Krause, K. J. Schafer, and K. C. Kulander, "High-order harmonic generation from atoms and ions in the high intensity regime", *Phys. Rev. Lett.*, vol. 68, pp. 3535–3538, 24 1992. DOI: 10.1103/PhysRevLett.68.3535 (Cited on page 30).

[89] M. Lewenstein, P. Balcou, M. Y. Ivanov, *et al.*, "Theory of high-harmonic generation by low-frequency laser fields", *Physical Review A*, vol. 49, no. 3, pp. 2117–2132, 1994. DOI: 10.1103/PhysRevA.49.2117. arXiv: 1106.1603 (Cited on pages 30, 33, 38).

[90] J. J. Macklin, J. D. Kmetec, and C. L. Gordon, "High-order harmonic generation using intense femtosecond pulses", *Phys. Rev. Lett.*, vol. 70, pp. 766–769, 6 1993. DOI: 10.1103/PhysRevLett.70.766 (Cited on page 30).

[91] C. Spielmann, N. H. Burnett, S. Sartania, *et al.*, "Generation of coherent x-rays in the water window using 5-femtosecond laser pulses", *Science*, vol. 278, no. 5338, pp. 661–664, 1997. DOI: 10.1126/science.278.5338.661 (Cited on page 30).

[92] Y. Tamaki, Y. Nagata, M. Obara, *et al.*, "Phase-matched high-order-harmonic generation in a gas-filled hollow fiber", *Phys. Rev. A*, vol. 59, pp. 4041–4044, 5 1999. DOI: 10.1103/PhysRevA.59.4041 (Cited on page 30).

[93] P. M. Paul, E. S. Toma, P. Breger, *et al.*, "Observation of a train of attosecond pulses from high harmonic generation", *Science*, vol. 292, no. 5522, pp. 1689–1692, 2001. DOI: 10.1126/science.1059413. eprint: http://science.sciencemag.org/content/292/5522/1689.full.pdf (Cited on page 30).

[94] R. Kienberger, E. Goulielmakis, M. Uiberacker, *et al.*, "Atomic transient recorder", *Nature*, vol. 427, no. 6977, p. 817, 2004 (Cited on page 30).

[95] P. á. Corkum and F. Krausz, "Attosecond science", *Nature physics*, vol. 3, no. 6, p. 381, 2007 (Cited on page 30).

[96] E. J. Takahashi, Y. Nabekawa, and K. Midorikawa, "Low-divergence coherent soft x-ray source at 13 nm by high-order harmonics", *Applied Physics Letters*, vol. 84, no. 1, pp. 4–6, 2004. DOI: 10.1063/1.1637949 (Cited on page 30).

[97] E. Takahashi, Y. Nabekawa, T. Otsuka, *et al.*, "Generation of highly coherent submicrojoule soft x rays by high-order harmonics", *Phys. Rev. A*, vol. 66, p. 021 802, 2 2002. DOI: 10.1103/PhysRevA.66.021802 (Cited on page 30).

[98] T. Remetter, P. Johnsson, J Mauritsson, *et al.*, "Attosecond electron wave packet interferometry", English, *Nature Physics*, vol. 2, no. 5, pp. 323–326, 2006. DOI: 10.1038/nphys290 (Cited on page 30).

[99] T. Okino, K. Yamanouchi, T. Shimizu, *et al.*, "Attosecond nonlinear fourier transformation spectroscopy of co2 in extreme ultraviolet wavelength region", *The Journal of Chemical Physics*, vol. 129, no. 16, p. 161 103, 2008. DOI: 10.1063/1.3006026 (Cited on page 30).

[100] C. Winterfeldt, C. Spielmann, and G. Gerber, "Colloquium: Optimal control of high-harmonic generation", *Rev. Mod. Phys.*, vol. 80, pp. 117–140, 1 2008. DOI: 10.1103/RevModPhys.80.117 (Cited on page 32).

[101] D. Bauer and P. Mulser, "Exact field ionization rates in the barrier-suppression regime from numerical time-dependent schrödinger-equation calculations", *Phys. Rev. A*, vol. 59, pp. 569–577, 1 1999. DOI: 10.1103/PhysRevA.59.569 (Cited on page 32).

[102] S. Augst, D. Strickland, D. D. Meyerhofer, *et al.*, "Tunneling ionization of noble gases in a high-intensity laser field", *Phys. Rev. Lett.*, vol. 63, pp. 2212–2215, 20 1989. DOI: 10.1103/PhysRevLett.63.2212 (Cited on page 32).

[103] P. Rudawski, "Second-generation high-order harmonic sources—from cpa to opcpa", PhD thesis, 2014 (Cited on pages 35, 39).

[104] P Salieres, T Ditmire, K. Budil, *et al.*, "Spatial profiles of high-order harmonics generated by a femtosecond cr: Lisaf laser", *Journal of Physics B: Atomic, Molecular and Optical Physics*, vol. 27, no. 9, p. L217, 1994 (Cited on page 35).

[105] P. Salières, A. L'Huillier, and M. Lewenstein, "Coherence control of high-order harmonics", *Phys. Rev. Lett.*, vol. 74, pp. 3776–3779, 19 1995. DOI: 10.1103/PhysRevLett.74.3776 (Cited on pages 35, 36).

[106] A. L'Huillier, X. F. Li, and L. A. Lompré, "Propagation effects in high-order harmonic generation in rare gases", *Journal of the Optical Society of America B*, vol. 7, no. 4, p. 527, 1990. DOI: 10.1364/JOSAB.7.000527 (Cited on page 35).

[107] P. Balcou, P. Sali'eres, A. L'Huillier, *et al.*, "Generalized phase-matching conditions for high harmonics: The role of field-gradient forces", *Phys. Rev. A*, vol. 55, pp. 3204–3210, 4 1997. DOI: 10.1103/PhysRevA.55.3204 (Cited on page 36).

[108] P. Balcou and A. L'Huillier, "Phase-matching effects in strong-field harmonic generation", *Phys. Rev. A*, vol. 47, pp. 1447–1459, 2 1993. DOI: 10.1103/PhysRevA.47.1447 (Cited on page 36).

[109] K. J. Schafer and K. C. Kulander, "High harmonic generation from ultrafast pump lasers", *Phys. Rev. Lett.*, vol. 78, pp. 638–641, 4 1997. DOI: 10.1103/PhysRevLett.78.638 (Cited on page 36).

[110] S. Kazamias, D. Douillet, F. Weihe, *et al.*, "Global optimization of high harmonic generation", *Phys. Rev. Lett.*, vol. 90, p. 193 901, 19 2003. DOI: 10.1103/PhysRevLett.90.193901 (Cited on page 36).

[111] E. Constant, D. Garzella, P. Breger, *et al.*, "Optimizing high harmonic generation in absorbing gases: Model and experiment", *Phys. Rev. Lett.*, vol. 82, pp. 1668–1671, 8 1999. DOI: 10.1103/PhysRevLett.82.1668 (Cited on pages 36, 37, 55).

[112] V. Gruson, "Polarimétrie harmonique et spectroscopie de photoionisation attoseconde", PhD thesis, Paris Saclay, 2015 (Cited on pages 38, 45).

[113] J. Mauritsson, P. Johnsson, E. Gustafsson, *et al.*, "Attosecond pulse trains generated using two color laser fields", *Phys. Rev. Lett.*, vol. 97, p. 013 001, 1 2006. DOI: 10.1103/PhysRevLett.97.013001 (Cited on pages 39, 40).

[114] J. Mauritsson, P. Johnsson, E Gustafsson, *et al.*, "Attosecond pulse trains generated using two color laser fields", *Physical review letters*, vol. 97, no. 1, p. 013 001, 2006 (Cited on page 39).

[115] "EdmundOptics", *Introduction to polarization*, 2018. eprint: https://www.edmundoptics.eu/resources/application-notes/optics/introduction-to-polarization/ (Cited on page 42).

[116] G. G. Stokes, "On the composition and resolution of streams of polarized light from different sources", *Transactions of the Cambridge Philosophical Society*, vol. 9, p. 399, 1851 (Cited on page 43).

[117] E. Collett, *Field guide to polarization*. SPIE press Bellingham, 2005, vol. 15 (Cited on page 43).

[118] H Müeller, "The foundations of optics", *J. Opt. Soc. Am*, vol. 38, p. 661, 1948 (Cited on page 44).

[119] K. S. Budil, P. Salières, A. L'Huillier, *et al.*, "Influence of ellipticity on harmonic generation", *Phys. Rev. A*, vol. 48, R3437–R3440, 5 1993. DOI: 10.1103/PhysRevA.48.R3437 (Cited on page 45).

[120] P. Antoine, B. Carré, A. L'Huillier, *et al.*, "Polarization of high-order harmonics", *Phys. Rev. A*, vol. 55, pp. 1314–1324, 2 1997. DOI: 10.1103/PhysRevA.55.1314 (Cited on page 45).

[121] V. V. Strelkov, "Theory of high-order harmonic generation and attosecond pulse emission by a low-frequency elliptically polarized laser field", *Phys. Rev. A*, vol. 74, p. 013 405, 1 2006. DOI: 10.1103/PhysRevA.74.013405 (Cited on page 46).

[122] J Stöhr, "Exploring the microscopic origin of magnetic anisotropies with x-ray magnetic circular dichroism (xmcd) spectroscopy", *Journal of Magnetism and Magnetic Materials*, vol. 200, no. 1-3, pp. 470–497, 1999 (Cited on page 46).

[123] Y. Mairesse, J. Higuet, N. Dudovich, *et al.*, "High harmonic spectroscopy of multichannel dynamics in strong-field ionization", *Phys. Rev. Lett.*, vol. 104, p. 213 601, 21 2010. DOI: 10.1103/PhysRevLett.104.213601 (Cited on page 46).

[124] X. Zhou, R. Lock, N. Wagner, *et al.*, "Elliptically polarized high-order harmonic emission from molecules in linearly polarized laser fields", *Phys. Rev. Lett.*, vol. 102, p. 073 902, 7 2009. DOI: 10.1103/PhysRevLett.102.073902 (Cited on page 46).

[125] B. Vodungbo, A. Barszczak Sardinha, J. Gautier, *et al.*, "Polarization control of high order harmonics in the EUV photon energy range.", *Opt. Express*, vol. 19, no. 5, pp. 4346–4356, 2011. DOI: 10.1364/OE.19.004346 (Cited on page 46).

[126] O. Kfir, P. Grychtol, E. Turgut, *et al.*, "Generation of bright phase-matched circularly-polarized extreme ultraviolet high harmonics", *Nature Photonics*, vol. 9, no. 2, p. 99, 2015. DOI: 10.1038/NPHOTON.2014.293 (Cited on pages 46–48).

[127] T André, I. Andriyash, A Loulergue, *et al.*, "Control of laser plasma accelerated electrons for light sources", *Nature communications*, vol. 9, no. 1, p. 1334, 2018. DOI: 10.1038/s41467-018-03776-x (Cited on page 47).

[128] D. Strickland and G. Mourou, "Compression of amplified chirped optical pulses", *Optics communications*, vol. 55, no. 6, pp. 447–449, 1985 (Cited on page 48).

[129] S. Backus, C. G. Durfee III, M. M. Murnane, *et al.*, "High power ultrafast lasers", *Review of scientific instruments*, vol. 69, no. 3, pp. 1207–1223, 1998 (Cited on page 48).

[130] S. Kazamias-Moucan, "Optimisation d'une source d'harmoniques d'ordres élevés pour l'optique non-linéaire dans l'extrême uv", PhD thesis, Ecole Polytechnique X, 2003 (Cited on page 51).

[131] S. Kazamias, F. Weihe, D. Douillet, *et al.*, "High order harmonic generation optimization with an apertured laser beam", *The European Physical Journal D - Atomic, Molecular, Optical and Plasma Physics*, vol. 21, no. 3, pp. 353–359, 2002. DOI: 10.1140/epjd/e2002-00193-0 (Cited on page 51).

[132] T. Brabec and F. Krausz, "Intense few-cycle laser fields: Frontiers of nonlinear optics", *Rev. Mod. Phys.*, vol. 72, pp. 545–591, 2 2000. DOI: 10.1103/RevModPhys.72.545 (Cited on page 51).

[133] E. J. Takahashi, Y. Nabekawa, and K. Midorikawa, "Low-divergence coherent soft x-ray source at 13 nm by high-order harmonics", *Applied physics letters*, vol. 84, no. 1, pp. 4–6, 2004. DOI: 10.1063/1.1637949 (Cited on page 51).

[134] D. M. Gaudiosi, B. Reagan, T. Popmintchev, *et al.*, "High-order harmonic generation from ions in a capillary discharge", *Phys. Rev. Lett.*, vol. 96, p. 203 001, 20 2006. DOI: 10.1103/PhysRevLett.96.203001 (Cited on page 51).

[135] S. Kazamias, S. Daboussi, O. Guilbaud, *et al.*, "Pressure-induced phase matching in high-order harmonic generation", *Phys. Rev. A*, vol. 83, p. 063 405, 6 2011. DOI: 10.1103/PhysRevA.83.063405 (Cited on page 52).

[136] X. He, M. Miranda, J. Schwenke, *et al.*, "Spatial and spectral properties of the high-order harmonic emission in argon for seeding applications", *Phys. Rev. A*, vol. 79, p. 063 829, 6 2009. DOI: 10.1103/PhysRevA.79.063829 (Cited on page 54).

[137] Y. Tamaki, J. Itatani, M. Obara, *et al.*, "Optimization of conversion efficiency and spatial quality of high-order harmonic generation", *Phys. Rev. A*, vol. 62, p. 063 802, 6 2000. DOI: 10.1103/PhysRevA.62.063802 (Cited on page 55).

[138] M Ferray, A L'Huillier, X. F. Li, *et al.*, "Multiple-harmonic conversion of 1064 nm radiation in rare gases", *Journal of Physics B: Atomic, Molecular and Optical Physics*, vol. 21, no. 3, p. L31, 1988 (Cited on page 55).

[139] J. Rothhardt, M. Krebs, S. Hädrich, *et al.*, "Absorption-limited and phase-matched high harmonic generation in the tight focusing regime", *New Journal of Physics*, vol. 16, no. 3, p. 033 022, 2014 (Cited on page 55).

[140] E. Takahashi, Y. Nabekawa, M. Nurhuda, *et al.*, "Generation of high-energy high-order harmonics by use of a long interaction medium", *J. Opt. Soc. Am. B*, vol. 20, no. 1, pp. 158–165, 2003. DOI: 10.1364/JOSAB.20.000158 (Cited on page 55).

[141] A. Averchi, D. Faccio, R. Berlasso, *et al.*, "Phase matching with pulsed bessel beams for high-order harmonic generation", *Phys. Rev. A*, vol. 77, p. 021 802, 2 2008. DOI: 10.1103/PhysRevA.77.021802 (Cited on page 55).

[142] C. F. R. Caron and R. M. Potvliege, "Optimum conical angle of a bessel–gauss beam for low-order harmonic generation in gases", *J. Opt. Soc. Am. B*, vol. 16, no. 9, pp. 1377–1384, 1999. DOI: 10.1364/JOSAB.16.001377 (Cited on page 55).

[143] T. Auguste, O. Gobert, and B. Carré, "Numerical study on high-order harmonic generation by a bessel-gauss laser beam", *Phys. Rev. A*, vol. 78, p. 033 411, 3 2008. DOI: 10.1103/PhysRevA.78.033411 (Cited on page 55).

[144] M. Nisoli, E. Priori, G. Sansone, *et al.*, "High-brightness high-order harmonic generation by truncated bessel beams in the sub-10-fs regime", *Phys. Rev. Lett.*, vol. 88, p. 033 902, 3 2002. DOI: 10.1103/PhysRevLett.88.033902 (Cited on page 55).

[145] C. Altucci, R. Bruzzese, D. D'Antuoni, *et al.*, "Harmonic generation in gases by use of bessel–gauss laser beams", *J. Opt. Soc. Am. B*, vol. 17, no. 1, pp. 34–42, 2000. DOI: 10.1364/JOSAB.17.000034 (Cited on page 55).

[146] E. A. Gibson, A. Paul, N. Wagner, *et al.*, "High-order harmonic generation up to 250 ev from highly ionized argon", *Phys. Rev. Lett.*, vol. 92, p. 033 001, 3 2004. DOI: 10.1103/PhysRevLett.92.033001 (Cited on page 56).

[147] P. Antoine, A. L'Huillier, M. Lewenstein, *et al.*, "Theory of high-order harmonic generation by an elliptically polarized laser field", *Phys. Rev. A*, vol. 53, pp. 1725–1745, 3 1996. DOI: 10.1103/PhysRevA.53.1725 (Cited on page 56).

[148] B. Vodungbo, B. Tudu, J. Perron, *et al.*, "Indirect excitation of ultrafast demagnetization", *Scientific Reports*, vol. 6, pp. 1–9, 2016. DOI: 10.1038/srep18970 (Cited on page 80).

[149] X. Liu, "Investigation of the early time period of ultrafast magnetization dynamics", PhD thesis, 2018 (Cited on page 89).

[150] G. Lambert, A. Andreev, J. Gautier, *et al.*, "Spatial properties of odd and even low order harmonics generated in gas", *Scientific Reports*, vol. 5, pp. 1–10, 2015. DOI: 10.1038/srep07786 (Cited on page 91).

List of Figures

Étude de la dynamique d'aimantation ultra-rapide par l'effet Faraday en utilisant des harmoniques d'ordres élevés polarisées linéairement

Résumé :
Dans cette thèse, nous démontrons qu'un rayonnement harmonique XUV polarisé linéairement peut être utilisé en spectroscopie d'absorption pour accéder à l'état de magnétisation de tout type d'échantillon, contrairement à toutes les techniques développées jusque-là. En effet, pour la première fois, des expériences résolues en temps ont été réalisées par l'effet Faraday magnéto-optique, que nous exploitons autour du seuil d'absorption magnétiquement dichroïque $M_{2,3}$ du Cobalt à 60 eV. La technique pompe-sonde a été utilisée pour obtenir la réponse dynamique des échantillons magnétiques lors de l'excitation laser. Les changements dans l'aimantation de l'échantillon sont associés aux changements dans la polarisation du faisceau harmonique de sonde, i.e. à la fois à la rotation de l'axe de polarisation et à la variation de l'ellipticité. Les principaux résultats de cette thèse démontrent que la mesure de l'effet Faraday offre un moyen ultrasensible de caractériser l'aimantation de films très minces (seulement quelques nm de matériaux magnétique). De plus, l'effet Faraday ayant lieu sur une large plage spectrale il est possible de suivre la dynamique simultanée de différents matériaux et donc d'étudier des matériaux très complexes.

Mots clés : Désaimantation ultra-rapide, Effet Faraday, Rotation de Faraday, Ellipticité, Cobalt, Harmoniques d'ordres élevés, Polarisation linéaire, Laser femtoseconde

Studying ultrafast magnetization dynamics through Faraday effect and using linearly polarized high order harmonics

Abstract:
In this thesis, we demonstrate that a linearly polarized XUV harmonic radiation can be employed in absorption spectroscopy to access the magnetization state of any type of sample, unlike all the techniques developed so far. Indeed, for the first time, time-resolved experiments were realized through the magneto-optical Faraday effect, which we exploit around the magnetically dichroic Co $M_{2,3}$ absorption edge at 60 eV. The pump-probe technique was used to obtain the dynamic response of the magnetic samples upon laser excitation. The changes in the magnetization of the sample are associated to the changes in the polarization of the probe harmonic beam, i.e. the rotation of the polarization axis and the variation of the ellipticity. The main results of this thesis demonstrate that the measurement of the Faraday effect offers an ultra-sensitive way to characterize the magnetization of very thin films (only a few nm of magnetic materials). Moreover, since the Faraday effect takes place over a wide spectral range, it is possible to follow the simultaneous dynamics of different materials and thus to study very complex materials.

Keywords: Ultrafast magnetization, Faraday effect, Faraday rotation, Ellipticity, Cobalt, High order harmonics, Linear polarization, Femtosecond laser